The Pennsylvania State University
The Graduate School

THE ROBUSTNESS OF BINARY BLACK HOLE MERGERS AND WAVEFORMS

A Dissertation in
Physics
by
Tanja Bode

Submitted in Partial Fulfillment
of the Requirements
for the Degree of

Doctor of Philosophy

August 2009

The dissertation of Tanja Bode was reviewed and approved* by the following:

Lee Sam Finn
Professor of Physics
Chair of Committee

Deirdre Shoemaker
Assistant Professor of Physics (Adjunct)
Dissertation Advisor

Martin Bojowald
Assistant Professor of Physics

Michael Eracleous
Associate Professor of Astronomy & Astrophysics

Jayanth R. Banavar
Professor of Physics
Head of the Department of Physics

*Signatures are on file in the Graduate School.

Abstract

In the past five years, the field of numerical relativity has changed dramatically. With many groups now able to simulate merging black holes and more breakthroughs coming almost monthly, there is much competition to pick off as many astrophysically relevant situations as possible. It is sensible, though, to step back from this competition and to look on the new techniques and results with more skeptical eyes than before.

In this dissertation we look at two aspects of initial data from new perspectives and find the waveforms generated from merging binary black hole (BBH) systems to be robust to significant errors in the initial data. In the first study we find that, by adding tuneable auxiliary gravitational waves into a BBH spacetime, up to 1% extra Arnowitt-Deser-Misner (ADM) energy can be added to a standard BBH system before the waveforms are significantly altered. While this study is based on observations of spurious radiation found in all standard initial data sets to date, the second study takes a more general approach. With an eye towards setting up more complex black hole (BH) systems, we find that evolutions of skeleton approximate initial data based on solutions to the ADM Hamiltonian with point sources also yield robust gravitational waveforms that are accurate enough for use in matched template searches for gravitational wave signals in the Laser Interferometer Gravitational-wave Observatory (LIGO) band. We also consider the interpretation of a possible class of constraint violations as an unphysical negative energy field that is absorbed by the BHs. Both of these studies show that the change in apparent horizon (AH) masses during the evolution is a good way to gauge the robustness of the extracted waveforms.

At the end of this dissertation we discuss ongoing work on evolving BBH mergers embedded in gaseous clouds. This is the first study with the new matter code `Scotch` which couples a hydrodynamic matter field to the fully-nonlinear spacetime evolution code. Evolving a wet BBH system will gauge how robust gravitational wave templates are given that true astrophysical sources are not in vacuum. This is a first step at considering the larger question of whether the presence of gas can overcome the "last parsec" problem, hastening the mergers and thereby increasing the expected merger rates.

Table of Contents

List of Figures

List of Tables

List of Symbols

For a discussion of the conventions used in this work, see Sec. 1.4 at the end of the introduction.

Σ_τ	Cauchy hypersurface parametrized by τ, p. 8
n^α	Unit normal vector to a hypersurface unless otherwise noted, p. 8
$\perp_{ab}$	Spatial projection operator, p. 9
$g_{\mu\nu}$	Full 4-dimensional metric, p. 7
$T_{\mu\nu}$	Stress-energy-momentum tensor, p.7
$R_{\alpha\beta\gamma\delta}$	Full 4-dimensional Riemann tensor, p. 29
γ_{ij}	Spatial 3-metric, p. 8
K_{ij}	Extrinsic curvature, p. 9
α	Lapse function, p. 8
β^i	Shift vector, p. 8
$\breve{\nabla}_i$	Covariant derivative with respect to γ_{ij}, p. 10
$\mathcal{R}_{ijkl}$	Spatial Riemann tensor, p. 29
$\mathcal{R}_{ij}$	Spatial Ricci tensor, p. 10
$\mathcal{R}$	Spatial scalar curvature, p. 10
$\mathbb{C}_H$	Scalar (Hamiltonian) constraint, p. 9
$\mathbb{M}_i$	Vector (Momentum) constraint, p. 10
ρ	Total energy density as seen by an observer n^α, p.10
S^i	Total energy current as seen by an observer n^α, p.10
S_{ij}	Energy-matter Structure tensor as seen by an observer n^α, p.10

S	Trace of the structure tensor S_{ij}, p.10
ψ	Generic conformal factor, p. 11
ϕ	BSSN conformal factor, p. 11
χ	Moving Puncture conformal factor, p. 11
K	Trace of the extrinsic curvature, p. 11
A_{ij}	Traceless extrinsic curvature, p. 11
$\tilde{\gamma}_{ij}$	Conformal spatial 3-metric, p. 11
$\tilde{A}_{ij}$	Traceless conformal extrinsic curvature, p. 11
$\tilde{\nabla}_i$	Covariant derivative with respect to $\tilde{\gamma}_{ij}$, p. 12
$\tilde{\Gamma}^i$	Conformal connection functions, p. 12
$\tilde{\mathcal{R}}_{ij}$	Conformal spatial Ricci tensor, p. 12
$\tilde{\mathcal{R}}$	Conformal spatial scalar curvature, p. 20
${}_nY^{lm}$	Spin-weighted spherical harmonics, p. 95
$d\Omega$	Standard solid angle element, p. 32
Ψ_{0-4}	The five Weyl scalars, p. 29
$\mathcal{P}^i$	Linear momentum vector, p. 21
$\mathcal{S}^i$	Spin vector, p. 21
$\mathcal{M}_{AH}$	Apparent Horizon (AH) mass, p. 26
$\mathcal{M}_{\rm ADM}$	ADM mass (or equivalently $\mathcal{E}_{\rm ADM}$), p. 25
$\mathcal{P}^i_{\rm ADM}$	ADM linear momentum, p. 25
$\mathcal{J}^i_{\rm ADM}$	ADM angular momentum, p. 25
ρ_o	Rest mass density, p.78
v^i	Comoving velocity, p.78
ϵ	Internal energy, p.78
h	Specific enthalpy, p.78
P	Pressure, p.78

W Lorentz factor, p.80

D Conserved mass-energy density, p.79

τ Conserved mass-energy, p.79

S_i Conserved comoving momentum, p.79

Acknowledgments

"It is a miracle that curiosity survives a formal education." – *Albert Einstein*

Nobody works in true isolation though I might at times wish for and even attempt it. This work would of course not have been possible without the support I received from friends, family, and colleagues who have not let me give up.

First I must thank Deirdre Shoemaker, my advisor, whose kind words and open door made working with her a great pleasure.

I must also thank Pablo Laguna, my collaborator and co-advisor, for enlightening me in the dark ways of academic work in certain fields. I thank him for the many animated discussions and an unforgettable monologue over a glass of marsala in a Sicilian monastery.

I very much appreciated the invaluable help, insightful discussions, and enjoyable work environment provided by my colleagues Roland Haas, Ian Hinder, Frank Herrmann, Eloisa Bentivegna, Shaun Wood, James Healy, and Nico Yunes. When the bugs seemed to be winning, their camaraderie made coming into the office much less painful. I would also like to thank Erik Schnetter, Frank Löffler, and Richard O'Shaughnessy for their discussions.

Of course I could not have done this without my good friends: BJ Cooley, Adrienne Criss, Dan Costantino, Shaun Wood, Dave Sloan, Ajaychander Chandrashekar, Tim Russin, Mitchell Schuster, and Victor Taveras. They tolerated me when I was intolerable. They were there when I needed to smile with words of encouragement, points of advice good and bad, and yes, the occasional much-needed hug.

I am also very much indebted to Mother Nature. Her beauty and the peace, found not only on the wooded ridges and by the hidden streams of Pennsylvanian forests but also in the wondrous high peaks of the Colorado Rocky Mountains or simultaneously wild and tame Austrian Alps during my summer breaks, brought me clarity and calm when I needed it most.

Last but certainly *not* least, I am indebted to my parents Ute and Udo Bode, who never held me back even when they thought I was reaching too far. I especially need to thank my sister, Sonja, who has inspired me to shoot for the stars and taught me that no place on Earth is truly out of my reach. Of course my family across the ocean also supported me well. My grandmother, my many aunts, and especially Ulla Bode who never doubted I could.

The work in Chapter 4 was done in collaboration with D. Shoemaker, I. Hinder, and F. Herrmann. It was supported in part by National Science Foundation (NSF) grants PHY-0653443, PHY-0555436 and PHY-0114375 (CGWP). The work in Chapter 5 was done in collaboration with P. Laguna, D. Shoemaker,

I. Hinder, F. Herrmann, and B. Vaishnav. It was supported by the same NSF grants as the previous chapter and, in addition, by NSF grants PHY-0354821, PHY-0244788, and PHY-0801213. Computations were performed at NCSA and TACC under allocation TG-PHY060013N, and at the Information Technology Services at Penn State. I also received the Duncan Fellowship which helped support my endeavors during my research.

Dedication

I dedicate this work to the Gods of Snow and Mountains. May they be so generous as to heap many feet upon my head during the remainder of my life and let me see more of the subsequent snow-covered world from mountain summits in the years to come.

> "The scientist does not study nature because it is useful; he studies it because he delights in it, and he delights in it because it is beautiful. If nature were not beautiful, it would not be worth knowing, and if nature were not worth knowing, life would not be worth living."
>
> – *Jules Henri Poincaré*

Chapter 1

Introduction

"The realities of nature surpass our most ambitious dreams." – *Rodin (1837-1868)*

The goals of Numerical Relativity are two-fold: (1) to simulate gravitational waves as aids in the eventual detection of real gravitational waves and (2) to expand our understanding of general relativity, extensions thereof, and alternative theories in the most non-linear regime where analytical solutions cannot reach and approximations are no longer valid. Numerical studies of binary black hole (BBH) systems using fully non-linear codes are crucial to both these endeavors as they delve deeper into the non-linear regime than analytical techniques have thus far been able to achieve, simultaneously opening up new regimes of gravity and testing the limits of applicability for each analytical technique. The extreme masses of black holes (BHs) in such a highly dynamic setting are simultaneously the strongest anticipated source of gravitational waves and a perfect testbed for exploring gravity's strong regime. In this chapter we will discuss the astrophysical motivation behind studying BBH evolutions in Sec. 1.1 and progress in the area thus far in Sec. 1.2. A road map for this dissertation is laid out in Sec. 1.3 followed by a note on the conventions in Sec. 1.4.

1.1 Astrophysical Motivations for Numerical Binary Black Hole Studies

Astronomical evidence for the existence of BHs, although indirect, has been found in abundance. Black holes are roughly divided into three mass categories: stellar, intermediate, and supermassive. Stellar mass BHs, with masses of order ten times that of the sun, are the corpses of supermassive stars. Intermediate BHs, measuring hundreds to thousands of solar masses, have possibly been observed for the first time quite recently [144] in the center of globular clusters where the density of stellar material may have allowed stellar mass BHs to merge and grow significantly. Finally, supermassive BHs, measuring over 10^6 solar masses, have been shown to exist at the center of many spiral galaxies in the form of Active Galactic Nuclei (AGN). In our own Milky Way Galaxy, observers have tracked the motion of stars in the immediate vicinity of the galactic center and shown that there must exist a very massive, very compact object there [88, 90]. Even

in a playground as vast as the universe, there is always a possibility two BHs will become gravitationally entwined and dance until they merge.

1.1.1 Gravitational Wave Sources

The first strong "laboratory" test for the existence of gravitational waves was the binary neutron system, containing the pulsar PSR 1913+16, discovered by Hulse and Taylor in 1974 [107]. By 1982, enough observations of this system had been made to find that the orbital decay of the binary was consistent with Einstein's general relativity and inconsistent with alternative theories of gravity [172]. This discovery strengthened the search for gravitational waves already in progress through Weber bars [185], limited in their range, and the first early interferometric gravitational wave detector by Levine and Stebbins [122] which put an upper limit on gravitational waves emitted by the Crab pulsar. The case for gravitational waves made by the system with PSR 1913+16 paved the way for the first generation of large-scale interferometric gravitational wave detectors. At this point in history, the currently operational interferometry-based gravitational wave detectors – LIGO, Virgo, GEO600, and TAMA – have run their first few science runs. LIGO is now undergoing improvements to Enhanced LIGO and then Advanced LIGO which, with its order of magnitude increase in sensitivity, is expected to hear the first gravitational wave signal when online. There is a possibility, though, that the first gravitational waves are not detected by interferometers with man-made light sources, but by pulsars in pulsar timing array (PTA)s [83] where timing residuals observed similarly illuminate the gravitational waves passing between Earth and the pulsars. These strides in gravitational wave detection makes it likely that the first gravitational wave signals will be detected in the next five to ten years.

The list of possible sources for gravitational waves being studied is quite lengthy [162, 49]. There are the inspiral emissions of binary systems, whether the participants are white dwarfs, neutron stars, or black holes. There are many types of transient signals: close encounters in highly eccentric binaries, mergers of compact binary systems, the ringdown of a merged binary as it settles down to a stationary BH, the gravitational collapse of a massive stellar core during a supernova, perturbations on rapidly rotating neutron stars, etc. The list goes on, but these are the strongest sources anticipated. There will likely be sources that we are *not* anticipating, possibly generated by physics we do not understood yet. All these sources are expected to lie on top of a stochastic background of gravitational waves generated by the Big Bang, carrying information of processes from energies we have not been able to observe before.

Unfortunately, the weak interactions of gravitational waves with matter means they are quite difficult to detect. It is for this reason that so many resources have been dedicated to understanding and predicting the gravitational wave signals of the strongest and most likely signal to be detected above noise of Earthly origin. If the ground-based interferometers, with their bandwidth at relatively high frequencies ($\sim 10 - 10^3$ Hz for Advanced LIGO), do not detect gravitational waves, there are plans for the first space-based detector, the Laser Interferometer Space Antenna (LISA). Source studies are already keeping an eye on the LISA's much lower frequency bandwidth ($\sim 5\times10^{-5} - 10^{-1}$ Hz) and realizing signals are much more likely to be in

abundance in that band. Even without LISA, the PTAs such as Parkes radio telescope [129] can also reach a completely different frequency range, currently ($\sim 10^{-9} - 10^{-6}$ Hz) [165] which complements both LIGO and LISA in its frequency range and may even beat LIGO to the first direct detection of gravitational waves.

1.1.2 Population Studies of Compact Binaries

Population studies feed both into and from gravitational wave detection. They predict how often signals from specific sources might be seen given our current understanding of cosmological evolutions and astronomical observations. Population syntheses such as those by Belczynski *et al.* [33, 34] use numerical methods to evolve a population of stars to simulate the formation of compact objects and subsequent compact binaries, yielding estimates of galactic merger rates. The conclusions based on current models are that, of the compact binaries, binary neutron star systems are most common with predicted detection rates of $\sim 20\text{yr}^{-1}$ for Advanced LIGO. Our BBH systems are expected to be far less common with detection rates of $\sim 2\text{yr}^{-1}$ [34]. On the other hand, BBH signals are much stronger than binary neutron star systems and, given numerical relativity's (NR's) ability to simulate gravitational waveforms in vacuum spacetimes, are much better understood and thus more easily detected. The models used to derive these numbers, though, could well be wrong. How often we *do* detect compact binary signals, whether it is more or less frequent than predicted, will feed back into population studies to yield a better understanding of the evolution of the universe.

Beyond numbers are the characteristics expected of binary compact objects in the real Universe. In 1964, Peters [148] showed the emission of gravitational radiation tended to circularize binary systems. The speedy circularization was simulated recently by Hinder *et al.* [106] for BBH systems. Despite this, the many-body interactions found inside globular clusters could keep perturbing intermediate mass BBH systems into eccentric orbits [10, 117]. Finally, there are also the effects of matter on binary compact object evolutions. In so-called "wet" mergers where participating compact objects have accretion disks, the gas in the system is thought to align the spins [39] and possibly hasten a merger [15]. Though this decreases the possible observed parameter space, there are other mechanisms by which BHs with interesting spin orientations may merge. Until we observe many of these systems by their gravitational wave emissions, it is important that the NR community explore fully the parameter space of binary compact objects, and specifically BBH systems. With a basic understanding of non-linear general relativistic mergers, the astrophysical community has a better chance to understand the signals we detect, and the signals we do *not* detect, expanding our understanding of the universe at large.

1.2 Binary Black Hole Simulations: A Brief History

Starting from a field where simulations were highly idealized and the holy grail was a BBH which could be simulated with controllable errors through merger and indefinitely beyond, to a time when all the major

astrophysically relevant vacuum systems have been at least briefly studied, the field has come a long way in the past few years - relatively fast-paced development in an area of research almost half a century old [156].

Attempts have been made to solve the Einstein equations for BBH systems since Hahn and Lindquist's 1964 study [98] of two "worm holes" in a time-symmetric, axisymmetric system. The techniques and computational resources of the day allowed limited degrees of freedom and a very short evolution. Hahn's study was at the leading edge of an intensive era of BH studies[137], but numerical studies of BBH systems took a back burner to understanding the fundamental properties of BHs. It was 10 years into this period that Smarr [168] and then Eppley [73] extracted the first rough gravitational waves out of a BBH system, the head-on collision. Still, another 15 years passed before numerical studies took hold as a separate field, propelled by the prospects of gravitational wave detection since LIGO was finally seen as a concrete possibility. These prospects of detecting gravitational waves spurred the community to turn back to numerical studies in order to predict the signals that could be detected and to provide waveform templates for matched filtering, desired for finding signals buried in noise.

Many developments in both computational power, theoretical understanding, and formulations since this revival have contributed to our current ability to evolve BBH systems through merger. Chief among these were the advent of large-scale multi-processor computing, mesh refinement [163, 2], the *Moving Puncture Technique* (MPT) [27, 55], and the Baumgarte-Shapiro-Shibata-Nakamura (BSSN) formalism [166, 30]. The latter two are not to be viewed as requirements for successful BBH evolutions in general, but merely the set of formalisms and methods which allowed the first breakthrough evolutions [155, 26, 56] of inspiralling BBHs through merger.

The first successful BBH mergers that allowed commonly used approaches sparked a mass migration of numerical codes to the techniques that proved successful. Equal-mass, non-spinning, quasi-circular BBHs begun at various separations [26, 56] were just the beginning. Herrmann *et al.* [103] studied the coalescence of unequal-mass BBHs, followed by similar studies by Baker *et al.* [23] and Gonzalez *et al.* [92]. Soon studies were done that added eccentricity [170, 106]. Spins were added, which expanded the parameter space further and proved quite interesting. It was found that asymmetries in either mass or spin configurations resulted in final BHs with unexpectedly large linear momentum, popularly dubbed a kick [92, 104, 105, 131]. This spurred vigorous conversations concerning the evolution of large-scale structure in the universe and population estimates of BHs.

The initial race to cover final BH kicks and other parameter space has started to ebb as the merger waveforms were found to be not as obviously interesting as was hoped, being replaced with a new collaborative atmosphere. The Samurai project [101] brings numerical groups together to compare the consistency of waveforms between different groups and convey the comparison in a way that is relevant to gravitational wave observations. Other collaborative efforts are underway such as NINJA [21] that tie into the data analysis efforts to test the sensitivity of the data analysis techniques used for the first generation of interferometry-based gravitational wave observatories.

In the past few years the field of Numerical Relativity has overflowed with new results. It is within this timeframe that the studies in this dissertation took place.

1.3 Robustness of Simulation Results

The studies presented in this dissertation explore three ways in which the robustness of numerical BBH evolutions, in the face of both numerically and astrophysically motivated perturbations, are considered. These studies shed some light for the Numerical Relativity community on the degree of non-linearity hidden in results from BBH mergers. Aspects such as the orbital dynamics, properties of the final BH, and the generated waveforms are compared across these perturbations. The robustness of the final BH's properties and the generated waveform are of interest to the NR community in evaluation of current evolution techniques as well as the data analysis community in their search for gravitational waves.

We begin with a discussion of the relevant theoretical background in Chapter 2 wherein we discuss the formulation and gauges used in the vacuum portion of this work. We also briefly summarize the `MayaKranc` code with its capabilities and shortcomings. Chapter 3 continues the discussion of background theory to initial data generation methods, discussing again the approximations, assumptions and shortfalls thereof. In addition, we examine the methods of analyzing the resulting four-dimensional spacetime including gravitational waveform extraction and measurements of mass and momentum.

Chapter 4 presents the first study wherein we use model gravitational waves "added" to a standard BBH system to simulate additional spurious radiation in the intiial data. In this way, we consider how robust BBH evolutions are to spurious gravitational waves, especially with respect to the numerical errors in the initial data which manifest themselves as spurious gravitational radiation.

The second study, presented in Chapter 5, considers errors in the initial data from a more relevant source. Given that constructing completely accurate initial data is computationally intensive and the construction of physically accurate initial data for reasonably close BBH systems is still a topic of study, we consider a skeleton approximate initial data which models the BHs as point masses. Evolving this, we discuss the behavior of the constraint violations and its effects on the resulting merger dynamics and waveforms.

Beginning in Chapter 6 we shift towards spacetimes where a matter field is coupled to the spacetime evolution. This requires a discussion on matter field formulations and coupling its evolutions to spacetime evolutions of `MayaKranc` in Chapter 6. In Chapter 7 we present preliminary results of how robust a BBH system is when embedded in a gaseous cloud. Finally, we summarize the results of all studies and reflect on remaining open questions in Chapter 8.

1.4 Conventions

In this dissertation we follow the conventions of Wald [184] and Misner *et al.* [137] where the metric has the signature -,+,+,+. Unless otherwise noted, we use geometrized units: $G = c = 1$. All simulations are done such that the results are scalable by the total irreducible mass of the system, i.e. $M_{\rm irr} = 1$.

The indices of tensor quantities are chosen to be either Greek or Latin. Greek indices span four dimensions, $\mu \in 0, 1, 2, 3$, while Latin indices are reserved for the spatial dimensions, $i \in 1, 2, 3$. Unless otherwise notified, the order of the spatial coordinates will be (x, y, z) in Cartesian coordinates and (r, θ, ϕ) in spherical polar coordinates. Symmetrization is designated by $A_{(ab)} \coloneqq \frac{1}{2}(A_{ab} + A_{ba})$ while anti-symmetrization is designated by $A_{[ab]} \coloneqq \frac{1}{2}(A_{ab} - A_{ba})$.

We choose to define our Riemann and Ricci tensors to follow the signs of Misner et. al [137]

$$R^{\alpha}_{\beta,\gamma,\delta} = \partial_{\gamma}\Gamma^{\alpha}_{\beta\delta} - \partial_{\delta}\Gamma^{\alpha}_{\beta\alpha} + 2\Gamma^{\alpha}_{\sigma[\gamma}\Gamma^{\sigma}_{\delta]\beta} \tag{1.1a}$$

$$R_{\alpha\beta} = R^{\sigma}_{\alpha\sigma\beta} \tag{1.1b}$$

and we choose to follow York's [192] sign convention in defining the extrinsic curvature,

$$K_{\alpha\beta} = -\frac{1}{2}\pounds_{\boldsymbol{n}}\gamma_{\alpha\beta}. \tag{1.2}$$

This is consistent with Misner *et al.*. [137] but not with Wald [184]. In separating the 4-dimensional from the spatial Riemann tensor, we denote all spatial Riemann tensor quantities using $\mathcal{R}$.

The BSSN formulation and the standard initial data require a conformal decomposition of the metric and related quantities. Conformal quantities are designated by a tilde over the physical quantity: $\tilde{A}$. Likewise complex conjugates are designated by a bar over the variable, $\overline{m}$. Tetrads are designated in bold type, $\boldsymbol{z}$, in Sec. 3.4. In other sections, the $i^{\rm th}$ vector of an array of vectors is designated by, for instance, $\boldsymbol{\xi}_i$.

Chapter 2

Spacetime Formulations and `MayaKranc`

> "You have to learn the rules of the game, and then you have to play better than anyone else." – *Albert Einstein*

At the base of all general relativity lies one set of equations, the Einstein equations. It can be written to look deceptively simple in geometrized units written as

$$G_{\alpha\beta} = 8\pi T_{\alpha\beta}. \tag{2.1}$$

The Einstein tensor, $G_{\alpha\beta} \coloneqq R_{\alpha\beta} - \frac{1}{2} g_{\alpha\beta} R$, is constructed from the metric and its derivatives. On the other side, the stress-energy-momentum tensor, $T_{\alpha\beta}$, contains information about matter in the spacetime. Numerical Relativity endeavors to solve these equations in their full non-linearity in regions of extreme gravity. Over the past 50 years that numerical relativity has been developing, there have been many approaches to solving these equations. In this chapter we discuss the basic theoretical framework of modern numerical relativity to the extent necessary for understanding the context for and methods of the studies presented in Ch. 4 and Ch. 5.

2.1 Decomposing the Einstein Equations: '3+1' Decomposition

At the very heart of modern numerical relativity is the decomposition of the very thing Einstein united in his theory of general relativity: spacetime. In the generic theory, we describe spacetime by a set $(\mathcal{M}, g_{ab})$ where g_{ab} is the four-dimensional metric defined everywhere on a manifold $\mathcal{M}$. Given no other framework, we find ourselves with 10 tightly coupled, second-order partial differential equations (PDEs) to be solved everywhere on the manifold $\mathcal{M}$ at once. The various decompositions treat one of the dimensions differently from the remaining three. We can then rewrite the Einstein equations as an initial value problem.

The decomposition of spacetime is best expressed as a *foliation* of the manifold $\mathcal{M}$ as we are not bound

to choose our decomposition in any particular way. The standard approach is to foliate the spacetime into a set of hypersurfaces, Σ_τ, parametrized by some time-like parameter, τ. What properties these hypersurfaces have depends on the formalism chosen. Some studies have chosen the hypersurfaces to lie along null cones emanating from a central world tube, dubbed "characteristic" formalisms [187]. Others have chosen hyperbolic hypersurfaces such that the outer boundaries lie at future null infinity, dubbed "conformal" formalisms [85, 84]. For the purposes of this dissertation we will concentrate our discussion on the third formalism, most often used in contemporary studies formalism, dubbed '3+1' or "Cauchy" decomposition.

In the '3+1' decomposition, we foliate spacetime by Cauchy hypersurfaces. These Cauchy hypersurfaces are fully spacelike surfaces so any timelike world line would intercept each surface at most *once*. We also require these foliations and the four-dimensional metric on these foliations to be smooth. In this way we conserve causality between our hypersurfaces even though our spacetime might evolve more slowly in one area of spacetime than in another.

2.1.1 ADM Formalism

Applying the above foliation of spacetime to the Einstein equations, we can restate them as a set of 4 constraint equations and 10 evolution equations for the full metric's 10 independent components. These equations, presented by Arnowitt, Deser, and Misner in 1962 [16] and popularized in form by York [192] in 1979, make up the ADM formalism. Their intuitive derivation represent the canonical '3+1' formulation where we foliate the four-dimensional spacetime into Cauchy hypersurfaces Σ_t parametrized by t, our chosen time coordinate.

With this foliation we can decompose $g_{\mu\nu}$ at any point in terms of the three-dimensional "spatial" metric $\gamma_{\mu\nu}$ intrinsic to Σ_t and a four-vector n^μ normalized to -1 and oriented normal to Σ_t:

$$g_{\mu\nu} = \gamma_{\mu\nu} - n_\mu n_\nu. \tag{2.2}$$

The actual time direction is related to the hypersurface normal n^μ by

$$t^\mu = \alpha n^\mu + \beta^\mu \tag{2.3}$$

where we have introduced the *lapse function* α and the *shift vector* β^μ. Together the lapse and shift encode the gauge, or coordinate freedom, of general relativity. The lapse is a measure of how t changes between hypersurfaces while a non-zero shift allows for a shifting in spatial coordinates between hypersurfaces. Given a choice in lapse and shift together with a spatial metric, we can reconstruct the four-metric line element as

$$ds^2 = -\alpha^2 dt^2 + \gamma_{ij}(dx^i + \beta^i dt)(dx^j + \beta^j dt). \tag{2.4}$$

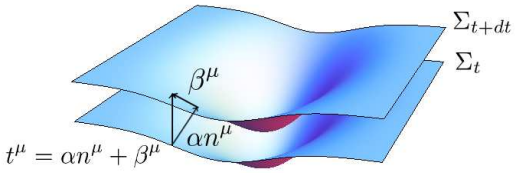

Figure 2.1. Schematic of the ADM foliation with the break up of the metric into spatial and temporal variables.

In matrix form the metric and its dual are

$$g_{\mu\nu} = \begin{pmatrix} -\alpha^2 + \beta_k\beta^k & \beta_i \\ \beta_j & \gamma_{ij} \end{pmatrix}, \; g^{\mu\nu} = \frac{1}{\alpha^2}\begin{pmatrix} -1 & \beta^i \\ \beta^j & \alpha^2\gamma^{ij} - \beta^i\beta^j \end{pmatrix}. \tag{2.5}$$

A schematic of the ADM formalism is shown in Fig. 2.1.

Being spatial, quantities intrinsic to Σ_t have a reduced number of degrees of freedom. We note that any spatial vector A^μ can be uniquely denoted by its spatial components, A^i. The spatial index can be lowered using the spatial metric and the zeroth vector component is derived from the spatial components by lowering the indices with the full metric: $A^\mu = (0, A^i)$, $A_\mu = (-\beta_i A^i, A_i)$. It is still advantageous to define a spatial projection operator:

$$\perp^\mu_\nu := \gamma^\mu_\nu = g^\mu_\nu + n^\mu n_\nu. \tag{2.6}$$

.

The spatial metric γ_{ij} is our primary variable to be evolved in the initial value problem. However, knowing the spatial metric on the hypersurface, the lapse function, and the shift vector is not enough. We also need the *extrinsic curvature*, $K_{\mu\nu}$, which is the embedding of the particular hypersurface in the general spacetime. The extrinsic curvature is defined through a Lie derivative along the vector perpendicular to Σ_t.

$$K_{\mu\nu} := -\frac{1}{2}\pounds_{\boldsymbol{n}}\gamma_{\mu\nu} \tag{2.7}$$

where $\pounds_{\boldsymbol{n}}$ is the Lie derivative along the vector n^μ.

To complete this formalism, Einstein's equations must also be separated into spatial and temporal components. We proceed by projecting the equations spatially and temporally. This gives us four equations that relate only quantities intrinsic to one hypersurface and must vanish at all points for the hypersurface to satisfy the Einstein equations. Therefore these are constraint equations for the hypersurfaces. By projecting both indices onto n^a, the Einstein equations yield the scalar (or Hamiltonian) constraint $\mathbb{C}_H$

$$\mathbb{C}_H := n^\mu n^\nu (G_{\mu\nu} - 8\pi T_{\mu\nu}) = \mathcal{R} + K^2 - K^{ij}K_{ij} - 16\pi\rho. \tag{2.8}$$

where $\mathcal{R}$ is the *spatial* scalar curvature and ρ is the projection of the stress-energy-momentum tensor in the same manner: $\rho \coloneqq n^\mu n^\nu T_{\mu\nu}$. The vector (or Momentum) constraint $\mathbb{M}_i$ is derived by projecting one index of the Einstein equations onto the hypersurface and the other onto the normal n^μ:

$$\mathbb{M}_i \coloneqq n^\mu \perp_i^\nu (G_{\mu\nu} - 8\pi T_{\mu\nu}) = \breve{\nabla}_j K_i^j - \breve{\nabla}_i K + 8\pi S_i. \tag{2.9}$$

Here we denote $\breve{\nabla}_i$ as the spatial covariant derivative connected with the spatial metric and the quantity S_i is similarly derived from the stress-energy-momentum tensor: $S_i \coloneqq -n^\mu \perp_i^\nu T_{\mu\nu}$. We will look at these constraint equations in more detail in Ch. 5.

The quantity ρ can be interpreted as the total energy density in the local matter fields of the spacetime as seen by an observer n^a. Similarly the quantity S^i can be interpreted as the total energy current of the spacetime as seen by the same observer. In this vein we can decompose the stress-energy-momentum tensor into spatial and temporal components as

$$T^{\mu\nu} = \rho n^\mu n^\nu + 2S^{(\mu} n^{\nu)} + S^{\mu\nu} \tag{2.10}$$

where we have introduced the spatial structural tensor S_{ij}.

To find the evolution equation for the spatial metric, we need to compute the Lie derivative of γ_{ij} along t^μ.

$$\pounds_{\boldsymbol{t}} \gamma_{ij} = \pounds_{\alpha \boldsymbol{n} + \beta} \gamma_{ij} = \alpha \pounds_{\boldsymbol{n}} \gamma_{ij} + \pounds_{\beta} \gamma_{ij} = -2\alpha K_{ij} + \pounds_{\beta} \gamma_{ij} \tag{2.11}$$

The extrinsic curvature's evolution equation can be derived from the Einstein equations and the Ricci relation as

$$\begin{aligned} \partial_t K_{ij} \quad = \quad & -\breve{\nabla}_i \breve{\nabla}_j \alpha + \alpha(\mathcal{R}_{ij} - 2K_{ik}K_j^k + KK_{ij}) - 8\pi\alpha(S_{ij} - \frac{1}{2}\gamma_{ij}(S - \rho)) \\ & + \beta^k \breve{\nabla}_k K_{ij} + K_{ik}\breve{\nabla}_j \beta^k + K_{kj}\breve{\nabla}_i \beta^k \end{aligned} \tag{2.12}$$

where $\mathcal{R}_{ij}$ is the *spatial* Ricci tensor and S is the trace of the structural tensor S_{ij}.

In summary, the ADM formalism decomposes the full spacetime into a spatial metric γ_{ij} with 6 independent components, an extrinsic curvature K_{ij} also with 6 independent components, a lapse function α, and a spatial shift vector β^i. It gives us 16 independent, quasi-linear first-order PDEs and 4 constraint equations. This is an improvement from the 10 highly-coupled, quasi-linear, second-order PDEs for the 10 independent components if you naïvely expand the Einstein equations into metric components and coordinates. This is, however, not sufficient to solve the full four-dimensional spacetime. While the canonical ADM formalism is intuitive and has proved to *lead* to successful formulations, it itself is not well-posed as an initial value problem [156]. In the face of numerical error during a simulation, it has been shown that the formulation is generally unstable and diverges from the constraint-satisfying hypersurfaces.

2.1.2 Baumgarte-Shapiro-Shibata-Nakamura (BSSN) Formulation

Although the ADM formalism is intuitive, it is not the formulation that has proved successful in numerical codes for merging BBHs. The formulation utilized in this work is the BSSN formulation [166, 30] (a good review is found in [31]). This is derived from the ADM formalism by a conformal decomposition of the spatial metric, a traceless (and generally transverse) and conformal decomposition of the extrinsic curvature, an additional variable with related constraint equation, and the addition of factors of the constraints to the evolution equations for the purpose of avoiding terms that misbehave.

A York-Lichnerowicz conformal transformation [123, 190] maps one metric onto that of another metric by the relation, $g_{\alpha\beta} = \Omega^2 \tilde{g}_{\alpha\beta}$ where Ω can be any smooth function (see Wald [184] Appendix D for a general discussion of conformal transformations). In the BSSN formulation, we simplify equations involving the spatial metric by performing a conformal decomposition

$$\tilde{\gamma}_{ij} \coloneqq \psi^{-4} \gamma_{ij} \tag{2.13}$$

and using a simpler spatial metric as our conformal metric $\tilde{\gamma}_{ij}$, thus hiding a lot of the complexity within the single degree of freedom found in the conformal factor, ψ. The power of 4 is chosen for convenience.

We similarly decompose the extrinsic curvature. Before we do so, though, we separate out the trace K

$$K_{ij} = A_{ij} + \frac{1}{3} \gamma_{ij} K. \tag{2.14}$$

leaving the traceless extrinsic curvature A_{ij}. It is this *traceless* extrinsic curvature which we conformally decompose with the same conformal factor as the spatial metric:

$$\tilde{A}_{ij} \coloneqq \psi^{-4} A_{ij}. \tag{2.15}$$

In the BSSN formulation, we take into account that the conformal factor ψ must be positive, introducing the BSSN conformal factor ϕ such that $\psi = e^{\phi}$. For simplicity we choose $\phi = (\ln \gamma)/12$ such that the determinant of the conformal metric is unity. However, when representing BHs in our spacetimes using the puncture method (see Sec. 3.1.3), the divergences of ψ and ϕ at the punctures lend to numerical problems in the evolution. In order to regularize the conformal factor, we introduce another conformal factor χ which we evolve instead of ϕ. In some parts of the evolution equations, as you will see, we still use ϕ. The three conformal factors are then related such that

$$\chi = \psi^{-4} = e^{-4\phi} \tag{2.16}$$

and the two conformal decompositions are

$$\gamma_{ij} = \chi^{-1}\tilde{\gamma}_{ij}, \tag{2.17a}$$
$$A_{ij} = \chi^{-1}\tilde{A}_{ij}. \tag{2.17b}$$

We also introduce the conformal connection functions $\tilde{\Gamma}^i$ defined as

$$\tilde{\Gamma}^i := \tilde{\gamma}^{jk}\tilde{\Gamma}^i_{jk} \tag{2.18}$$

where $\tilde{\Gamma}^i_{jk}$ are the connections of the conformal metric. If the determinant of the conformal metric were unity at all times as it analytically should be, $\tilde{\Gamma}^i = -\partial_j\tilde{\gamma}^{ij}$. However, due to numerical error this is not necessarily the case. We evolve $\tilde{\Gamma}^i$ as a separate variable and replace the derivatives of the metric found in its own evolution equation by itself, which lets us avoid taking derivatives of the metric and results in better convergence. This requires us to add a new constraint equation, derived from the definition of $\tilde{\Gamma}^i$, which must be monitored during the evolution

$$\mathbb{C}_{\tilde{\Gamma}} := \tilde{\Gamma}^i - \tilde{\gamma}^{jk}\tilde{\Gamma}^i_{jk}\,. \tag{2.19}$$

With the conformal decompositions of the spatial metric and extrinsic curvature, the extraction of the extrinsic curvature's trace, and the introduction of the conformal connection functions $\tilde{\Gamma}^i$, the BSSN variables for evolution are ϕ, $\tilde{\gamma}_{ij}$, K, $\tilde{A}_{ij}$, and $\tilde{\Gamma}^i$. Due to the divergences in ϕ for our puncture treatment of BHs, though, we take as our evolution variables the set χ, $\tilde{\gamma}_{ij}$, K, $\tilde{A}_{ij}$, and $\tilde{\Gamma}^i$.

Given the BSSN variables and our change in conformal factor, our evolution equations can be derived from the ADM evolution equations as [7]

$$\partial_t\chi = -\frac{2}{3}\chi(\alpha K + \partial_j\beta^j) + \beta^i\partial_i\chi \tag{2.20a}$$
$$\partial_t\tilde{\gamma}_{ij} = -2\alpha\tilde{A}_{ij} + \beta^k\partial_k\tilde{\gamma}_{ij} + 2\tilde{\gamma}_{k(i}\partial_{j)}\beta^k - \frac{2}{3}\tilde{\gamma}_{ij}\partial_k\beta^k \tag{2.20b}$$
$$\partial_t K = -\chi(\tilde{\nabla}^j\tilde{\nabla}_j\alpha + 2\tilde{\gamma}^{ij}\partial_i\phi\cdot\tilde{\nabla}_j\alpha) + \alpha(\tilde{A}^{ij}\tilde{A}_{ij} + \frac{1}{3}K^2 + 4\pi(\rho + S)) + \beta^j\partial_j K \tag{2.20c}$$
$$\begin{aligned}\partial_t\tilde{A}_{ij} = {} & \chi(\alpha\tilde{\mathcal{R}}_{ij} + \alpha\tilde{\mathcal{R}}^{\phi}_{ij} - \tilde{\nabla}_i\tilde{\nabla}_j\alpha + 4\partial_{(i}\phi\cdot\tilde{\nabla}_{j)}\alpha - 8\pi\alpha S_{ij})^{\mathrm{TF}} + \alpha K\tilde{A}_{ij} - 2\alpha\tilde{A}_{ik}\tilde{A}^k_j \\ & + \beta^k\partial_k\tilde{A}_{ij} + 2\tilde{A}_{k(i}\partial_{j)}\beta^k - \frac{2}{3}\tilde{A}_{ij}\partial_k\beta^k\end{aligned} \tag{2.20d}$$
$$\begin{aligned}\partial_t\tilde{\Gamma}^i = {} & \beta^j\partial_j\tilde{\Gamma}^i + h^{kl}\partial_l\partial_k\beta^i + \frac{1}{3}\tilde{\gamma}^{ij}\partial_j\partial_k\beta^k - \tilde{\Gamma}^j\partial_j\beta^i + \frac{2}{3}\tilde{\Gamma}^i\partial_j\beta^j - \frac{4}{3}(\tilde{\Gamma}^i - \tilde{\gamma}^{lm}\tilde{\Gamma}^i_{lm})\partial_j\beta^j \\ & -2\tilde{A}^{ij}\partial_j\alpha + 2\alpha(\tilde{\Gamma}^i_{kl}\tilde{A}^{kl} + 6\tilde{A}^{ij}\partial_j\phi - \frac{2}{3}\tilde{\nabla}^i K - 8\pi\tilde{\gamma}^{ij}S_j)\end{aligned} \tag{2.20e}$$

where $\tilde{\nabla}_i$ and $\tilde{\mathcal{R}}_{ij}$ are the covariant derivative and Ricci tensor, respectively, with respect to $\tilde{\gamma}_{ij}$. Additionally

we define the quantity

$$\tilde{\mathcal{R}}^{\phi}_{ij} = -2\tilde{\nabla}_i\tilde{\nabla}_j\phi - 2\tilde{\gamma}_{ij}\tilde{\nabla}^k\tilde{\nabla}_k\phi + 4\tilde{\nabla}_i\phi\cdot\tilde{\nabla}_j\phi - 4\tilde{\gamma}_{ij}\tilde{\nabla}^k\phi\cdot\tilde{\nabla}_k\phi \tag{2.21}$$

which relates the spatial Ricci tensor to the conformal Ricci tensor by $\mathcal{R}_{ij} = \tilde{\mathcal{R}}_{ij} + \tilde{\mathcal{R}}^{\phi}$. In the derivation of these evolution equations, we have made modifications from the ADM formalism by adding appropriate factors of the constraints to two evolution equations:

$$\partial_t K \rightarrow \partial_t K + \alpha\mathbb{C}_H, \tag{2.22a}$$

$$\partial_t\tilde{\Gamma}^i \rightarrow \partial_t\tilde{\Gamma}^i - 2\alpha\mathbb{M}^i \tag{2.22b}$$

For a more in-depth discussion of the derivation of these equations, see [7].

The scalar and vector constraint equations (Eq. 2.8 and 2.9) can similarly be rewritten in terms of our BSSN variables so the set of monitored constraints are, in addition to Eq. 2.19,

$$\mathbb{C}_H = \chi\tilde{\gamma}^{ij}(\tilde{\mathcal{R}}_{ij} + \tilde{\mathcal{R}}^{\phi}_{ij}) - \tilde{A}_{ij}\tilde{A}^{ij} + \frac{2}{3}K^2 - 16\pi\rho, \tag{2.23a}$$

$$\mathbb{M}_i = 6\tilde{A}^j_i\partial_j\phi + \tilde{\gamma}^{mk}(\partial_k\tilde{A}^{mi} - \tilde{\Gamma}^d_{mk}\tilde{A}_{di} - \tilde{\Gamma}^d_{ik}\tilde{A}_{md}) - \frac{2}{3}\partial_i K - 8\pi S_i. \tag{2.23b}$$

Precisely why this formulation has been so successful is still a topic of study. Separating out the trace of the extrinsic curvature K is useful for choosing and applying a slicing condition as, like the lapse, it is a scalar measure of how quickly the spacetime is changing. Gentle [87] suggests adding constraints to the evolution equations of K and $\tilde{\Gamma}^i$ result in a partially constrained evolution system. That is, the presence of the additional constraint equation terms keeps the system from diverging. The well-posedness and conditions for hyperbolicity of the BSSN formulation in various gauges has been a popular topic of study [159, 161, 38, 96, 97]. These studies have found that the BSSN formulation is hyperbolic in some gauges, lending credibility to their usefulness from a mathematical standpoint.

At the beginning of the simulation we observe a gauge wave (unphysical wave in the gauges) carrying constraint violations propagate outwards from the area of greatest constraint violation (around the BHs) and the remaining constraint violations eventually damping down further outside the BHs. This is unlike the the ADM formalism where the constraint violations and initial gauge waves are stationary [6]. Observations such as this have lead to studies of constraint propagation systems [189, 167]. Regardless of the theoretical reasons, the BSSN formulation has proved most successful in solving the Einstein equations.

2.1.3 Slicing Conditions

As discussed for both the ADM and BSSN formulations, we are free to choose our gauge conditions, or *slicing conditions*. These conditions express how coordinates on one hypersurface relate to those on a

neighboring hypersurface. In terms of the ADM and BSSN formulations, this is the evolution of the lapse α and the shift β^i. From our discussion of the BSSN formulation in Sec. 2.1.2, our formulation says nothing about the lapse or shift evolution. The "trick" to a stable evolution is a good choice of gauge and the trick to a successful gauge depends, largely, upon how the physical singularities (i.e. the BHs) are handled.

An intuitive choice in gauge, called *maximal* slicing, avoids the infall of coordinate stationary observers (and thus gridpoints) to areas of strong gravity like BHs by imposing that proper time move more slowly in such regions and that the shift continually counteract the infall of gridpoints into this slowly evolving region. This leads first to the lapse condition. In maximal slicing, we want K to vanish and so choose it to do so initially, but we also want it to vanish on future time-slices. This is problematic as the condition for $\partial_t K = 0$ at all times is a computationally expensive elliptic equation to find the lapse. Instead, we implement a form of the *K-driver* condition [7, 40]

$$\partial_t \alpha = -\alpha^2 f(\alpha)(K - K_0) \tag{2.24}$$

where $f(\alpha)$ is some arbitrary function. The slicing condition is so named because it drives K to a constant value, K_0, in a relatively short amount of time and therefore driving the simulation towards a stationary solution. Another feature of the K-driver condition is that it causes the lapse to collapse, or vanish, exponentially at physical singularities at late times. This is very desirable for numerical simulations as the singularity within the BH stops evolving, effectively avoiding the singularity.

It was noted by Bona *et al.*. [40] that if we choose $f(\alpha) = 2/\alpha$ and $K_0 = 0$, the K-driver condition yields the condition

$$(\partial_t - \beta^i \partial_i)\alpha = -2\alpha K. \tag{2.25}$$

This condition is dubbed the "1+log" condition as the analytic solution is simple in terms of the spatial metric's determinant:

$$\alpha = 1 + \log \sqrt{\gamma}. \tag{2.26}$$

This particular condition mimics maximal slicing at the singularity since $f \to \infty$ when α vanishes.

The lapse condition is not the only condition we need to specify the gauge. Similar in concept to the K-driver is the $\tilde{\Gamma}^i$-driver which drives $\partial_t \tilde{\Gamma}^i$ to zero. This yields a shift condition

$$(\partial_t - \beta^k \partial_k)\beta^i = \lambda \partial_t \tilde{\Gamma}^i. \tag{2.27}$$

Before the major breakthroughs of 2005 it had become commonplace to excise the area within the apparent horizon (see Sec. 3.3) of the BHs. This method came with an array of problems such as specifying accurate inner boundary conditions, finding the apparent horizon before setting the final grid structure, and difficulties moving excised regions through a grid. Though excision is still in use and has improved, the method which the Penn State / Georgia Tech Numerical Relativity group uses for BBH simulations is the puncture method described in Section. 3.1.3. Punctures complicate the shift condition as the basis is

a mapping of another asymptotically flat spacetime to within the BH's horizon. The actual point of the puncture is a mapping of asymptotically flat infinity. Since infinity does not move, the shift which embodies how coordinates change should also vanish at that point. This spurred the development of MPT [27, 55], effectively excising the BH through the gauge conditions [48] and therefore leading to the first successful BBH simulations involving punctures. Evolving the lapse as the "1+log" slicing of Eq. 2.24, we alter the $\tilde{\Gamma}^i$-driver as follows:

$$(\partial_t - \beta^k \partial_k)\beta^i = \xi B^i \tag{2.28a}$$

$$(\partial_t - \beta^j \partial_j)B^i = -\eta B^i + \lambda \partial_t \tilde{\Gamma}^i - \zeta \beta^j \partial_j \tilde{\Gamma}^i \tag{2.28b}$$

where we choose the set of gauge parameters $\xi = \frac{3}{4}, \lambda = 1, \eta = 2, \zeta = 1$ to avoid superluminal gauge waves. These are the gauge conditions used in the studies of 4 and 5.

2.2 The MayaKranc Code

The simulation code used in this dissertation, developed first in 2005 by the Pennsylvania State University's Numerical Relativity group, now based at the Georgia Institute of Technology, is dubbed the MayaKranc code. Based on the Maya code developed at Penn State in the early 2000s, the MayaKranc code improved on the efficiency of the Maya code and makes use of the latest breakthroughs in formulation and gauge.

The MayaKranc code is based on the infrastructure of Cactus [3, 1], an open source code which provides an environment for communicating between processors. This includes splitting variables between processors, output utilities, a modular environment in which problem-specific code can interact (*thorns*), and a handful of basic thorns needed for solving initial value problems. Cactus is portable enough that we can compile our code on the various architectures of the different computing clusters available to us without too much extra effort.

On top of the Cactus infrastructure our grid approach to solving the equations requires adaptive mesh refinement for which we use Carpet [163, 2]. The need to extract gravitational waveforms requires we extend the physical outer boundary of our grids well away from any dynamics, to hundreds if not thousands of M where M is the total irreducible mass in the system. Simultaneously we also need very high resolution to resolve areas of strong gravity: for a non-spinning BH using the puncture method 3.1.3 a resolution of $M/25$ is a minimum. The need for speed and the limited and expensive computational resources available requires us to use refinement levels. Carpet is an open-sourced driver for the Cactus infrastructure which implements adaptive mesh refinement and utilities required to interface with it somewhat transparently.

The MayaKranc code itself is an array of thorns built on Cactus. The basic evolution thorn was generated using Kranc [108], a package which generates code through Mathematica from a script containing the equations in tensor notation. Kranc was used in generating the evolution thorn and the heart of the gravitational wave extraction thorn, among others. The basic spacetime evolution uses the Method of Lines from

Cactus to evolve the initial data on a Cartesian grid. All the simulations for this dissertation were done using 4th order Runga-Kutta as our integrator, though other choices are also available. There are thorns to track moving BHs and a thorn separate from Carpet to move finer refinement levels to follow the moving BHs. Besides setting basic analytical solutions as initial data, MayaKranc uses Ansorg's TwoPunctures [13] thorn to solve the basic BBH system. We will discuss initial data in more depth in Sec. 3.1. For analysis, MayaKranc has thorns to extract and analyze gravitational waveforms (Sec. 3.4), calculate the ADM spacetime quantities at finite radius, and calculate the spins of BHs. We also utilize thorns from the publicly available AEIThorns repository developed at the Albert Einstein Institut (AEI). In particular we utilize Erik Schnetter's branch of Thornburg's AHFinderDirect [175, 176, 177] to find the AHs in our spacetimes.

For the studies in Chapters 4 and 5 we use the vacuum version of MayaKranc. More specifically, in the evolution and constraint equations (Eq. 2.20, 2.23 and 2.19), we let the stress-energy-momentum quantities (ρ, S_{ij}, S^i) vanish. Starting in Ch. 6 we discuss the theoretical basis of Scotch, a new code based on the public version of Whisky [22] which is coupled to MayaKranc such that we can evolve spacetimes fully coupled with continuum hydrodynamics evolutions.

Chapter 3

Initial Data and Analysis

> "There are two mistakes one can make along the road to truth ... not going all the way, and not starting." – *Buddha*

Every initial value problem requires a beginning, but exactly where and what is the beginning? The stability of an evolution and the quality of the physics extracted from an evolution are directly related to the quality and type of initial data one evolves. We begin this chapter with a discussion of the various methods one can generate initial data, with a focus on the standard initial data evolved by the Numerical Relativity community in recent years and thus used in the studies described in Chapters 4 and 5. Initial data involving matter fields will be discussed in Ch. 6.

Yet just as there is a beginning, so to everything there must be an end and particularly an end result. We need to gain something of use besides a resulting four-dimensional spacetime that can be compared to intuition, to other evolutions, and particularly to experimental results. For discussions of gravitational waves we extract the waveforms using the method discussed in Sec. 3.4. As with all physics we want to build intuition and compare our results to this intuition, specifically a perspective of an object's mass and energy. Unlike in Newtonian gravity, this is a topic rife with complications which are discussed in Sections 3.2 and 3.3.

3.1 Binary Black Hole Initial Data

As an initial value problem, solving the Einstein equations using a '3+1' decomposition requires initial data which solves a set of constraints $\{\mathbb{C}_H, \mathbb{M}_i\}$ such that they are satisfied everywhere on the initial hypersurface. For the BSSN formulation, these constraint equations (Eq. 2.23) are a coupled set of elliptic equations which are difficult to solve, particularly when there is a BH in the spacetime. Cook [63], Pfeiffer *et al.* [149], and Gourgoulhon [94] have written reviews of recent initial data construction techniques.

There are two schools of initial data generation: conformal transverse-traceless (CTT) decompositions and conformal thin-sandwich decompositions (CTS). The conformal transverse-traceless decomposition such as the one detailed below, allows us to freely choose the conformal spatial metric $\tilde{\gamma}_{ij}$, the trace of the extrinsic curvature K, and the symmetric, transverse-traceless portion of the conformal extrinsic curvature $\mathcal{A}^{ij}$. For some people this is too much freedom. Needing more guidance to choose , the second school uses a conformal thin-sandwich decomposition. This decomposition couples with a gauge choice (see Sec. 2.1.3), taking a freely specifiable transverse tensor and conformal lapse to create the extrinsic curvature while being able to write down the time derivative of the spatial metric explicitly. This last point creates some guidance in choosing the freely specifiable quantities.

The ideal initial data for a BBH simulation given infinite computational resources would start with the BHs infinitely far apart with all objects in the spacetime that you wish to interact with it eventually also present. Failing this, what would be *correct* is an initial hypersurface containing the gravitational wave information from the entire system dynamics *before* the initial hypersurface plus any deformation of the BH's horizons due to other energy and mass in the spacetime (e.g., another BH). To date, neither of these ideal initial hypersurfaces can be generated and there are more types of new initial data being suggested than NR groups willing to forgo template bank and data analysis work to test the initial data's possible improvements on waveforms.

A brief survey of initial data generation shows several schools of thought. There have been attempts of varying degrees of success in the latter for BBH systems using straight post-Newtonian (PN) techniques. The initial data of Tichy *et al.* [180] and later improved by Kelly *et al.* [115] use PN to generate the initial $\{\tilde{\gamma}_{ij}, \tilde{A}_{ij}\}$ required for the CTT initial data. Nissanke [143] presents another 2nd-order PN solution for both CCT and extended CTS (XCTS) initial data.

Beyond straight PN techniques there are attempts to marry PN with other approximations. Alvi [9] followed by Yunes *et al.* [196, 195] combined PN solutions with asymptotic expansions to stitch together solutions from PN and perturbative solutions in the inner zone of each BH. Then of course there are attempts to modify the standard method detailed below by changing the conformal metric to something which is still well-behaved but not flat [99, 128].

Many of these approaches still need improvement. More importantly, while still computationally expensive to create and time-consuming to code up, they are generally only applicable, by design, to a limited type of BBH system such as equal-mass, non-spinning, or quasi-circular BBHs. This would require a large repository of initial data thorns, differing for the other spacetime decompositions and coordinate choices. In the following sections we take a closer look at the method considered standard for BBH initial data in this age where many groups have started combining the numerical waveforms with data analysis for the first LIGO science runs, spending considerable computational resources evolving BBH systems to generate the first waveform template banks. This initial data requires making some basic assumptions to simplify the constraint equations and choose the initial coordinates carefully in order to end up with a stable evolution.

It is the effects of the errors in this initial data that are the focus of the studies in the next chapters.

3.1.1 Spacetime Full of Holes

In order to create BBH initial data, it is first enlightening to consider a single BH system. Every introductory course on general relativity starts its discussion of BHs with the standard Schwarzschild metric for a single static BH:

$$ds^2 = -\left(1 - \frac{2M}{r}\right) dt^2 + \left(1 - \frac{2M}{r}\right)^{-1} dr^2 + r^2 d\theta^2 + r^2 \sin^2\theta d\varphi^2. \tag{3.1}$$

Our formulation involves a conformal decomposition and, in particular, an assumption of conformal flatness to simplify the constraint equations. We can change coordinates in the above line element to *isotropic* coordinates related to Schwarzschild coordinates by $r = \tilde{r}\left(1 + \frac{M}{2\tilde{r}}\right)^2$ to yield the isotropic line element

$$ds^2 = -\left(\frac{2\tilde{r} - M}{2\tilde{r} + M}\right)^2 dt^2 + \left(1 + \frac{M}{2\tilde{r}}\right)^4 \left(d\tilde{r}^2 + \tilde{r}^2 d\theta^2 + \tilde{r}^2 \sin^2\theta d\varphi^2\right). \tag{3.2}$$

In isotropic coordinates, then, foliating the spacetime by surfaces of constant coordinate time t creates hypersurfaces with a conformally flat intrinsic spatial metric, $\gamma_{ij} = \psi^4 \delta_{ij}$, where $\psi = 1 + \frac{M}{2\tilde{r}}$ is the conformal factor.

Unlike Schwarzschild coordinates with its coordinate singularity at the event horizon $r = 2M$, the only singularity in isotropic coordinates is the location of the BH singularity itself when the conformal factor diverges there. It is worth noting that the isotropic spatial metric is invariant under the transformation

$$\tilde{r} \to \left(\frac{M}{2}\right)^2 \frac{1}{\tilde{r}'} \tag{3.3}$$

where the fixed points of the isometry are the points on the event horizon in isotropic coordinates, $\tilde{r} = \frac{M}{2}$, and the singularity point $\tilde{r} = 0$ maps to infinity on another spacetime [46].

With this interpretation in mind, the problem with multiple BH spacetimes is that each new BH opens a doorway to another asymptotically flat spacetime while simultaneously breaking the symmetries which allows us to write the metric in the above form. Realizing this, Brill-Lindquist [46, 125] constructed a naïve approach to this problem by noting that under the assumptions of conformal flatness and time-symmetry ($K_{ij} = -K_{ij} = 0$) the Hamiltonian constraint is linear. Therefore one could satisfy the constraints by constructing a conformal factor from a superposition of single BH spacetimes. Given a spacetime with N BHs of masses m_n located at coordinates Ξ_n^i, a point x^i in the conformal space is attributed the Brill-Lindquist conformal factor

$$\psi_{\mathrm{BL}} \coloneqq 1 + \sum_n^N \frac{m_n}{2|\boldsymbol{x} - \boldsymbol{\Xi}_n|}. \tag{3.4}$$

This Brill-Lindquist initial data creates a spacetime with multiple BHs which are initially stationary,

but the interpretation is more valid the farther apart the BHs are. The resulting manifold for the spacetime actually as a topology that encompasses $N + 1$ asymptotically flat universes, one additional infinity mapped inside the horizon of each BH. Our method for solving the multiple-BH problem is a generalization of Brill-Lindquist data detailed in Sec. 3.1.3.

3.1.2 Bowen-York Approach

The way around waiting for a vast library of analytic initial data thorns for various physical scenarios is to employ some knowingly false assumptions to create a more flexible constraint solver which, though not exact, can be shown to be sufficient for generating the phenomenology of BBH mergers and waveforms to the accuracy where they become useful to the data analysis community in searching for gravitational waves from observatories such as LIGO. The Bowen-York approach [42, 41, 191], the basis of our initial data solver, assumes both conformal flatness and maximal slicing and requires an additional transverse decomposition of the extrinsic curvature.

For the sake of generating initial data we consider the constraint equations not from the BSSN formulation of Equations 2.23, but using a different conformal transformation. We still decompose the spatial metric by the same conformal factor $\gamma_{ij} = \psi^4 \tilde{\gamma}_{ij}$, but this time we decompose the traceless extrinsic curvature by a different factor of ψ, namely $A_{ij} = \psi^{-2} \tilde{A}_{ij}$ and the dual $A^{ij} = \psi^{-10} \tilde{A}^{ij}$. In this way, the full extrinsic curvature is decomposed as

$$K^{ij} = \psi^{-10} \tilde{A}^{ij} + \frac{1}{3} \gamma^{ij} K \tag{3.5}$$

and the constraint equations, assuming vacuum, imply

$$\tilde{\nabla}^i \tilde{\nabla}_i \psi - \frac{1}{8} \psi \tilde{\mathcal{R}} - \frac{1}{12} \psi^5 K^2 + \frac{1}{8} \psi^{-7} \tilde{A}_{ij} \tilde{A}^{ij} = 0, \tag{3.6a}$$

$$\check{\nabla}_j (\psi^{-10} \tilde{A}^{ij}) - \frac{2}{3} \check{\nabla}_j K = 0 \tag{3.6b}$$

where $\tilde{\mathcal{R}}$ is the Ricci scalar with respect to the conformal spatial metric $\tilde{\gamma}_{ij}$. We leave the spatial derivative in the momentum constraint for now as it is convenient later. We can now apply the assumptions of maximal slicing ($K = 0$) and conformal flatness ($\tilde{\mathcal{R}} = 0$) so three more terms vanish, leaving us with

$$\tilde{\nabla}^i \tilde{\nabla}_i \psi + \frac{1}{8} \psi^{-7} \tilde{A}_{ij} \tilde{A}^{ij} = 0, \tag{3.7a}$$

$$\check{\nabla}_j (\psi^{-10} \tilde{A}^{ij}) = 0 \tag{3.7b}$$

The Bowen-York approach to solving the constraints requires an additional decomposition: splitting the conformal traceless extrinsic curvature $\tilde{A}_{ij}$ into transverse and longitudinal tensors. Denoting the conformal

longitudinal operator as $\tilde{\mathbb{L}}$, this decomposition can be written

$$\tilde{A}^{ij} = \tilde{\mathcal{A}}^{ij} + (\tilde{\mathbb{L}}\mathcal{W})^{ij}. \tag{3.8}$$

Given our choice of conformal factor, we can show for any symmetric, transverse-traceless tensor $\mathcal{S}^{ij}$ that $\check{\nabla}_j \mathcal{S}^{ij} = \psi^{-10}\tilde{\nabla}_j(\psi^{10}\mathcal{S}^{ij})$. This simplifies the first term of the momentum constraint

$$\psi^{-10}(\tilde{\nabla}_j(\tilde{\mathcal{A}}^{ij}) + \tilde{\nabla}_j(\tilde{\mathbb{L}}\mathcal{W})^{ij}) = 0 \tag{3.9}$$

Since by definition $\tilde{\nabla}_j \tilde{\mathcal{A}}^{ij} = 0$, the first term vanishes and we are left with a simple vector Laplacian equation

$$(\tilde{\triangle}_L \mathcal{W})^i = 0 \tag{3.10}$$

where

$$\tilde{\triangle}_L \mathcal{W}^i := \tilde{\nabla}_j(\tilde{\mathbb{L}}\mathcal{W})^{ij} = \tilde{\nabla}^2 \mathcal{W}^i + \frac{1}{3}\tilde{\nabla}^i(\tilde{\nabla}_j \mathcal{W}^j) + \tilde{\mathcal{R}}^i_j \mathcal{W}^j. \tag{3.11}$$

Thus the additional transverse decomposition has successfully *uncoupled* the constraint equations and leaving us with an equation where we can solve for W, and thus $\tilde{A}_{ij}$, separately.

For a single BH of arbitrary linear momentum $\mathcal{P}^i$ and spin $\mathcal{S}^i$,

$$\tilde{A}_{ij} = \frac{3}{2r^2}\left[\mathcal{P}_i \mathfrak{n}_j + \mathcal{P}\mathfrak{n}_i - (\delta_{ij} - \mathfrak{n}_i\mathfrak{n}_j)\mathcal{P}^k \mathfrak{n}_k\right] + \frac{3}{r^3}\left[\epsilon_{kil}\mathcal{S}^l \mathfrak{n}^k \mathfrak{n}_j + \epsilon_{kjl}\mathcal{S}^l \mathfrak{n}^k \mathfrak{n}_i\right] \tag{3.12}$$

where r is the coordinate radius to the BH at Ξ^i, $\mathfrak{n}^i$ is the unit outward normal away from this BH ($\mathfrak{n}^i := (x^i - \Xi^i)/r$), and ϵ_{kil} is the Levi-Civita tensor. We can verify the interpretation of $\mathcal{P}^i$ and $\mathcal{S}^i$ as the linear momentum and spin by computing the ADM momentum and spin as discussed in Sec. 3.2 below. Since the momentum constraint in the Bowen-York approach is linear, a multiple-BH system's momentum constraint would be satisfied by a superposition of $\tilde{A}_{ij}$ for each BH center Ξ_n just like the Brill-Lindquist conformal factor.

3.1.3 Punctures

While the Bowen-York approach uncouples the scalar and vector constraint equations and gives us an analytical solution to the momentum constraint, we still have to solve the scalar constraint equation

$$\tilde{\nabla}^i \tilde{\nabla}_i \psi + \frac{1}{8}\psi^{-7}\tilde{A}_{ij}\tilde{A}^{ij} = 0. \tag{3.13}$$

Given a physical situation we can already calculate $\tilde{A}_{ij}$ so we need only solve for the conformal factor ψ. For this we generalize the Brill-Lindquist conformal factor of Eq. 3.4 to

$$\psi = \psi_o + u = \sum_n^N \frac{M_n}{2|\boldsymbol{x} - \boldsymbol{\Xi}_n|} + u \tag{3.14}$$

where u is some smooth function which incorporates the interaction between the N BHs. If the BHs are sufficiently far apart, $u = 1 + O(r^{-1})$. As in the original Brill-Lindquist conformal factor, the parameter M_n is the $\mathcal{M}_{\text{ADM}}$ (see Sec. 3.2) of the n^{th} BH should it be isolated from the others, but in general this is just a parameter we call the *bare* mass.

The ansatz that ψ takes this form allows us to rewrite the constraint equation again as an equation for u. Since ψ_o satisfies the homogeneous Laplace equation, this becomes a second-order differential equation for u

$$\tilde{\nabla}^i \tilde{\nabla}_i u + \frac{1}{8}(\psi_o + u)^{-7} \tilde{A}_{ij} \tilde{A}^{ij} = 0. \tag{3.15}$$

For a general set of parameters $M_n, \mathcal{P}^i_{(n)}, \mathcal{S}^i_{(n)}$, and $\Xi^i_{(n)}$ we still have a messy elliptic equation to solve for u. For a BBH system, we proceed farther by calling upon `TwoPunctures`, a code by Ansorg which solves the Hamiltonian constraint numerically on a single-domain using pseudo-spectral methods [13]. The key to this method is a chain of four coordinate transformations to reach a compactified bi-spherical coordinate system with the two punctures at the focal points, regular at both puncture locations, and spanning all of $\mathbb{R}^3$.

For the spectral solver's internal grid we choose coordinates (A, B, φ) where A_i and B_j are the zeros of the Chebyshev polynomials $T_{n_A}(1-2x)$ and $T_{n_B}(-x)$ respectively and φ_k are the zeros of the sinusoidal basis $\sin(n_\varphi \varphi)$. We are free to choose the spectral resolutions (n_A, n_B, n_φ) of the solver, knowing that the exponential convergence of spectral methods allows a relatively coarse spectral resolution such as $(30, 30, 16)$. The spectral solver's coordinates are then given by

$$A_i = \sin^2\left[\frac{\pi}{2n_A}\left(i + \frac{1}{2}\right)\right], \tag{3.16a}$$

$$B_i = -\cos\left[\frac{\pi}{n_B}\left(j + \frac{1}{2}\right)\right], \tag{3.16b}$$

$$\varphi_k = 2\pi \frac{k}{n_\varphi}. \tag{3.16c}$$

These coordinates are related to the conformal Cartesian spatial coordinates (x, y, z) by the transformation

$$x = b\,\frac{A^2+1}{A^2-1}\,\frac{2B}{1+B^2}, \tag{3.17a}$$

$$y = b\,\frac{2A}{1-A^2}\,\frac{1-B^2}{1+B^2}\cos\varphi, \tag{3.17b}$$

$$z = b \frac{2A}{1-A^2} \frac{1-B^2}{1+B^2} \sin\varphi. \tag{3.17c}$$

Having solved for u in the spectral coordinates using a Newton-Raphson iteration method, we transform back to our conformal Cartesian coordinates and fill in the gridpoints by calculating the superposition of Chebyshev polynomials and sinusoidal functions. In practice it is generally sufficient, and certainly more efficient, to just Taylor expand between the Cartesian points that map to the collocation points used in the spectral solver.

The coordinate transformation above is effective in solving the Hamiltonian constraint for BBH systems of arbitrary momenta and spins, and medium mass ratios (around $q = M_1/M_2 \simeq 0.3$). In the studies which follow in Chapters 4 and 5 we use modified versions of Ansorg's constraint solver to generate initial data which differs from this standard initial data.

No initial data is complete without setting the initial gauge. We choose $\beta^i = 0$ since the maximal slicing assumption does not require the coordinates to be shifting from the initial hypersurface to the next hypersurface. This quickly evolves away from zero with our slicing condition detailed in Sec. 2.1.3. As discussed in that section, we also use a K-driver which eventually collapses the lapse to zero at the BH. This collapse takes a significant time, though, so we hasten the process by creating a pre-collapsed lapse derived from our solution for the conformal factor, $\alpha = \psi^{-2}$.

3.1.4 Solving the Constraints: A Few Comments

It should be noted here that though we can introduce a linear momentum $\mathcal{P}^i$ or spin $\mathcal{S}^i$ to any BH in our initial data, this is an approximation. Due to the maximal slicing assumption, our BHs are stationary on the initial hypersurface though they build up linear momentum quickly over the first few M of evolution. Our use of the puncture method in solving the Hamiltonian constraint also assumes the singularity take the form of a point, but when spin is added to a BH, the geometry of the actual singularity becomes a ring instead. Garat and Price [86] showed that, because of this, there is no conformally flat coordinate system for a Kerr spacetime. Despite this, the initial data we construct from the method above allows for a non-zero spin parameter. This means spinning punctures are not true spinning BHs, but the spacetime outside the BHs' horizons evolve to a Kerr spacetime. Since it is the spacetime outside the horizons that interest us, the BHs are effectively spinning. Due to the kludge attempt at adding spin, the initial spin parameter cannot be set too high. Initial puncture spins of up to $j = |\mathcal{S}|/M^2 \simeq 0.8$ have been stably evolved without significantly increasing the resolution and post-merger spins have been observed and verified up to $j \simeq 0.96$. If a puncture spins up too much without high resolution at the puncture, the insufficient resolution dissipates the extra angular momentum. Thus, by increasing the resolution inside the puncture, higher initial spins can be made stable but at a high cost in computational resources and efficiency [65].

Another topic which merits discussion is the topology of our spacetime. In creating our puncture initial data, we compactify the infinities of the punctures to within the event horizon in our $\mathbb{R}^3$ manifold. Theoret-

ically we also excise the singularities themselves from the spacetime manifold $\mathcal{M}$ since the metric diverges there. In practice, though, this is done by either staggering the grid such that the singularity is *between* gridpoints, or by modifying the radial coordinate by $r \rightarrow \left(r^4 + \epsilon^4\right)^{1/4}$ where ϵ is a small parameter of order 10^{-5}. Studies by Brown *et al.* [48] have shown that punctures work precisely *because* we under-resolve the punctures within the horizons. By plotting the puncture region's gridpoints on a Kruskal diagram, he shows that the resolution of the region within the BH actually worsens as the evolution progresses with the standard shift condition. In `MayaKranc` we also set a minimum value for our conformal factor, $\chi = \psi^{-1/4}$, in calculating the right hand sides of the spacetime variables to avoid numerical problems.

Finally we should consider the viewpoint of constraint surfaces. The evolution equation for the conformal connection functions $\tilde{\Gamma}^i$ is just a rewritten form of the momentum constraint which is actively enforced throughout the evolution [87], yielding a *partially* constrained evolution system. It would be correct to solve the constraint equations on every timestep of our evolution, but this is prohibitively expensive in computational resources. Instead, we solve the constraints for the initial data and calculate the constraint violations $\left(\mathbb{C}_H, \mathbb{M}^i\right)$ to monitor how well the Einstein equations are being satisfied. In so doing, the space of *mathematical* solutions to the evolution equations given an initial data set, are all possible results. The set of solutions $\{\gamma_{ij}, K_{ij}\}$ at all time steps on which the constraint equations are satisfied span a subset of all the mathematical solutions to the evolution equations. A fully constrained system of evolution equations starting from an initial hypersurface on which all the constraints are exactly satisfied everywhere would ideally stay on this set of solutions, called a *constraint surface*. Computers don't function that way, though. Numerical errors create small constraint violations, moving the solution off the constraint surface into the space of solutions beyond. No study to date has sufficiently considered how far the BBH solutions move from the constraint surface or what ramifications this has on observable science.

It is impossible to remain on the constraint surface itself, but in the BSSN formulation the constraint surface has proved to be fairly stable – small constraint violations do not accelerate the system away from the constraint surface. In part, this is also due to artificial dissipation added to the spacetime variables to damp high frequency noise that would otherwise drive the system off the constraint surface. Precisely how much constraint violation is permissible before the gauge-invariant quantities extracted for physical interpretation become significantly corrupt is unknown and part of the motivation for the study in Ch. 5.

3.2 Analysis: Arnowitt-Deser-Misner (ADM) Mass and Momenta

To begin an analysis it is useful to connect the gauge-dependent quantities of our spacetime to Newtonian notions of mass and momentum. The problem herein lies in finding gauge-independent ways of calculating such quantities that can indeed be interpreted as, for instance, the mass on a given hypersurface. There are three classes of such quantities: local, quasi-local, and asymptotic. We leave the local quantities, derived from the notion of horizons, to Sec. 3.3 while the quasi-local notions are considered with the waveform

extraction in Sec. 3.4.

The asymptotic quantities, defined at spatial infinity, are notions of the *global* energy and momenta on the hypersurface. Termed the ADM mass and the ADM momenta, they traditionally take on the form found in Chapter 11 of Wald [184]. The definitions for the mass and linear momentum are given in his equations (11.2.14) - (11.2.15) while the angular momentum is left as an exercise at the end of the chapter. These definitions rely on the assumption of asymptotic flatness, that the full metric converges to flat space sufficiently quickly, to convert what would intuitively be a volume integral into a surface integral over a sphere at spatial infinity.

The integrals were rewritten assuming the BSSN's conformal decomposition by Murchadha *et al.* [139] and Bowen and York [42, 193]. In these quantities the ADM mass $\mathcal{M}_{\text{ADM}}$ is given by

$$\mathcal{M}_{\text{ADM}} \coloneqq -\frac{1}{2\pi} \oint_{\infty} \tilde{\nabla}^i \psi \mathrm{d}^2 S_i \tag{3.18}$$

where $\mathrm{d}^2 S_i$ is the area element on the sphere at infinity. Similarly the ADM linear momentum $\mathcal{P}^i_{\text{ADM}}$ is

$$\mathcal{P}^i_{\text{ADM}} \coloneqq \frac{1}{8\pi} \oint_{\infty} \tilde{K}^{ij} \mathrm{d}^2 S_i \tag{3.19}$$

and the ADM angular momentum $\mathcal{J}_{\text{ADM},\,i}$ is

$$\mathcal{J}_{\text{ADM},\,i} \coloneqq \frac{\epsilon_{ijk}}{8\pi} \oint_{\infty} x^j K^{kl} \mathrm{d}^2 S_l \tag{3.20}$$

where ϵ_{ijk} is the Levi-Civita tensor.

Since the method used in `MayaKranc` has a finite outer boundary, we cannot calculate this explicitly on our grid. Instead, we extrapolate by calculating the ADM quantities at many large radii. The radial dependence can then be empirically removed by fitting a polynomial in $1/r$ to the calculated ADM quantities provided the radii of the detectors are sufficiently far from the dynamical region. This also implies no gravitational waves should be radiating past any detectors, so the calculation must only be done on the initial data and final (if stationary) hypersurfaces.

3.3 Analysis: Horizons

The ADM mass and momenta described in Sec. 3.2 are very useful for discussing spacetime as a whole, but to understand the dynamics in a simulation we need to define a way of stating the mass of *one* of the BHs in a spacetime or the mass of a BH separated as best we can from the dynamics around it. That is, we need a local notion of mass, linear momentum, and angular momentum. Ideally this would be done through the event horizon as it bounds the region where everything is doomed to fall into the singularity. The difficulty here lies in that the event horizon is a three-dimensional object embedded in the full four-dimensional

spacetime that can only be found by looking backwards from the final hypersurface. It is possible to evolve null geodesics or null surfaces near the anticipated event horizon *backwards* in time given the full evolved spacetime so they would converge to the event horizon [68, 177]. This, unfortunately, is both expensive in memory storage and requires the simulation to be fully complete. We need a local notion of a horizon which can be defined and found on a single hypersurface to aid in both deriving physically-based notions for final analysis and for on-the-fly diagnostic checks that a simulation is still being physical. In this section we briefly describe two such notions. The first, apparent horizons, have a fast implementation to derive local notions of mass. The second, isolated and dynamic horizons, can also supply a notion of mass, but we instead use the framework for a quick and dirty method to calculate the spin of a BH.

3.3.1 Apparent Horizon

AHs are defined as *outermost* Marginal Outer Trapping Surfaces (MOTS). That is, an AH is a smooth (differentiable) closed orientable 2-sphere embedded in a three-dimensional hypersurface whose future-pointing, outgoing null geodesics have zero expansion Θ. For a Cauchy '3+1' foliated spacetime, this definition can be explicitly written as a 2-surface where the following elliptic equation is satisfied:

$$\Theta := \check{\nabla}_i \mathfrak{n}^i + \mathfrak{n}^i \mathfrak{n}^j K_{ij} - K = 0 \tag{3.21}$$

where $\mathfrak{n}^i$ is the (3-dimensional) unit normal to the 2-surface. With this definition we see that the AH is a gauge-dependent quantity whose interpretation must be handled with care. In fact, even for a stationary, single BH a gauge can be chosen where no AH exists. The concept has nonetheless proven quite useful in studies of BHs with the standard gauges used in numerical relativity.

The presence of an AH implies there is a BH contained within the horizon. There may, however, be *several* surfaces which satisfy Eq. 3.21 on a hypersurface, each surrounding one or more BHs. To find the true AH we would need to constantly check for a *common* AH, initially highly distorted, which indicates that the BHs inside can already be observed from outside as one distorted BH.

For a single, stationary BH, it can be shown that the event horizon and the AH coincide. More generally, an AH by definition will lie on or completely *within* the event horizon. This is fortunate as excision techniques use the AH as a guide to where excision must occur. More closely related to these studies, the accuracy of the initial data within the AH is not important as it is causally disconnected from the rest of the spacetime where our interests lie.

In our group's studies the AH is used primarily to provide a notion of a BH's mass. The effective AH mass $\mathcal{M}_{AH}$ is derived from the area of the AH by

$$\mathcal{M}_{AH} := \sqrt{\frac{A}{4\pi}}. \tag{3.22}$$

The location of the AH is also used in the calculation of the proper distance between BHs in Ch. 4. In other studies not included in this work, the shape of the AH, particularly the ratio of the circumferences, are utilized as a measure of the BH's distortion.

There is one more important drawback to AHs. As their definition is completely confined to a single hypersurface, there is no requirement for them to evolve smoothly between hypersurfaces. That is, if we combine the AHs found around a singularity into a world tube of apparent horizons, there is no requirement for this tube to be smooth and timelike or null. In fact, when the common AH is first found, the world tube will be spacelike and generally discontinuous. In our simulations, we typically follow the individual BH's AHs close to the merger, realizing that the common AH forms several 10s of M before merger. `AHFinderDirect` uses provided parameters for the center of the AHs, but the common horizon forms well before the coordinate locations of the punctures have reached the center of the common AH. For this reason the AH finder has a tendency to crash the simulation, so there is a break around merger when no AH mass is necessarily considered. The capability of dynamically shutting down one horizon search after another has been found has been developed, but this drawback has been left in order increase the speed of the AH finder.

3.3.2 Isolated and Dynamic Horizons

Since the advent of AHs there have been several new frameworks considered for horizon finding which yield new notions of local mass, momentum, and spin. Hayward [102], for instance, developed the notion of a "trapping horizon" similar to the world tube of AHs described above where the expansion is non-zero the horizon evolves. This led to the isolated horizon framework by Ashtekar, Beetle, and Fairhurst [17] and later the dynamical horizons framework by Ashtekar and Krishnan [18, 19]. Numerical implementations of isolated and dynamical horizon concepts were discussed by Dreyer *et al.* [71] and Schnetter *et al.* [164] respectively.

Isolated and dynamical horizons are $S^2 \times \mathbb{R}$ tubes defined in terms of null tetrads with expansions defined for the outgoing (l^μ) and ingoing (n^μ) null normals. Isolated horizons are null surfaces with no matter or radiation crossing them within a specific time frame and thus are both expansion and shear free. Dynamical horizons, on the other hand, are the generalization of isolated horizons when matter and/or radiation crosses the horizon [20].

Isolated and dynamic horizons cannot be found on a single hypersurface in isolation. Unlike AHs they need several timesteps in order to create a null tetrad with a time-like component. Requiring several timesteps, though, is a vast improvement from requiring all timesteps as the event horizon does, and its smoothly evolving geometry avoids the discontinuities found in AHs.

The results presented in this dissertation do not use the isolated or dynamical horizon framework to find a local notion of mass due to the current implementation's inefficiency. We do, however, use the notion of a local horizon spin derived in this framework. Given a Killing vector ξ^i associated with the spacetime, the

spin of a BH in the direction of ξ^i can be defined by

$$\mathcal{S}_\xi := \frac{1}{8\pi} \oint_{\mathrm{AH}} \xi^i \mathfrak{n}^j K_{ij} d^2S \tag{3.23}$$

where $\mathfrak{n}^i$ is the outward-pointing unit normal to the AH. Campanelli *et al.* [58] introduced the flat space coordinate rotational Killing vectors

$$\xi^i_x = (0, -\hat{z}, \hat{y}) \ , \tag{3.24a}$$

$$\xi^i_y = (\hat{z}, 0, -\hat{x}) \ , \tag{3.24b}$$

$$\xi^i_z = (-\hat{y}, \hat{x}, 0) \ . \tag{3.24c}$$

where the coordinates $(\hat{x}, \hat{y}, \hat{z})$ are relative to the coordinate center of the BH. The spin $\mathcal{S} = \left(\mathcal{S}_x, \mathcal{S}_y, \mathcal{S}_z\right)$ obtained with Campanelli's rotational Killing vectors agrees well with the one using the Killing vector ξ^i when one exists [58]. The spins calculated in this dissertation make use of either the Campanelli Killing vectors derived on a coordinate sphere of approximately the same radius as an AH would be expected (thus not requiring the AH finder to be active at all) or approximate Killing vectors derived on the AH itself. Herrmann *et al.* [105] found these methods to be approximately equal until the common AH is formed.

3.4 Analysis: Gravitational Waveforms

As no numerical study can claim to represent actual physics without tying into experiment, we need to extract information from our evolutions that can be compared to experiment (i.e. physics). In the case of BBH simulations, this requires extracting the gravitational waveforms that could be incident on a gravitational wave observatory such as LIGO or LISA from such physical situations. These waveforms are extracted through a calculation of a scalar, the 4th Weyl pseudo-scalar Ψ_4, using a fiducial tetrad whose construction is detailed in [24]. Together with I. Hinder, I wrote a wave extraction thorn, WeylScal4, for the `Cactus` infrastructure based on this method to replace a similar though inefficient wave extraction thorn.

3.4.1 Weyl Scalars

The Newman-Penrose formalism [141, 59] is a special tetrad formalism that has proven particularly useful in studying spacetimes with BHs. In tetrad formalisms, the Einstein equations are not considered using local, convenient, coordinate bases for the given problem. Instead they take a tetrad, 4 linearly independent vector fields, as their basis. The quantities of interest are then written by projections onto this tetrad basis. In the Newman-Penrose formalism, this tetrad is composed of four *null* vectors, $\boldsymbol{z} = \{\mathfrak{l}^\mu, \mathfrak{n}^\mu, \mathfrak{m}^\mu, \overline{\mathfrak{m}}^\mu\}$. Two vectors, $\mathfrak{l}^\mu$ and $\mathfrak{n}^\mu$, are real while the remaining two, $\mathfrak{m}^\mu$ and $\overline{\mathfrak{m}}^\mu$, are complex conjugates of each other. They

are also required to satisfy the following orthogonality condition:

$$\mathfrak{l}^\mu \mathfrak{m}_\mu = \mathfrak{l}^\mu \overline{\mathfrak{m}}_\mu = \mathfrak{n}^\mu \mathfrak{m}_\mu = \mathfrak{n}^\mu \overline{\mathfrak{m}}_\mu = 0. \tag{3.25}$$

Generally there is an additional convenient though unnecessary normalization condition imposed:

$$\mathfrak{l}^\mu \mathfrak{n}_\mu = 1, \tag{3.26a}$$
$$\mathfrak{m}^\mu \overline{\mathfrak{m}}_\mu = -1. \tag{3.26b}$$

The trace-free component of the Riemann tensor $R_{\alpha\beta\gamma\delta}$, dubbed the Weyl tensor, has 10 independent components for the full four-dimensional Riemann tensor. In the Newman-Penrose formalism, we project the Weyl tensor onto a set of four tetrad vectors to encase those 10 independent components in 5 complex scalars called Weyl scalars. Given the Weyl tensor $C_{\alpha\beta\gamma\delta}$, these are defined as

$$\Psi_0 = C_{\alpha\beta\gamma\delta} \mathfrak{l}^\alpha \mathfrak{m}^\beta \mathfrak{l}^\gamma \mathfrak{m}^\delta, \tag{3.27a}$$
$$\Psi_1 = C_{\alpha\beta\gamma\delta} \mathfrak{l}^\alpha \mathfrak{n}^\beta \mathfrak{l}^\gamma \mathfrak{m}^\delta, \tag{3.27b}$$
$$\Psi_2 = C_{\alpha\beta\gamma\delta} \mathfrak{l}^\alpha \mathfrak{m}^\beta \overline{\mathfrak{m}}^\gamma \mathfrak{n}^\delta, \tag{3.27c}$$
$$\Psi_3 = C_{\alpha\beta\gamma\delta} \mathfrak{l}^\alpha \mathfrak{n}^\beta \overline{\mathfrak{m}}^\gamma \mathfrak{n}^\delta, \tag{3.27d}$$
$$\Psi_4 = C_{\alpha\beta\gamma\delta} \mathfrak{n}^\alpha \overline{\mathfrak{m}}^\beta \mathfrak{n}^\gamma \overline{\mathfrak{m}}^\delta. \tag{3.27e}$$

These quantities are not true scalars as they are not constant under a rotation of the tetrad by an angle ψ (See Appendix A). As will be discussed in Sec. 3.4.2, for gravitational wave extraction Ψ_4 is the Weyl scalar of interest. The calculations for the remaining Weyl scalars are included in Appendix A. The version of the code available to the public only calculates Ψ_4.

The definition of Ψ_4 can be written in terms of the full Riemann tensor [52, 51, 54, 53], where in the following the 0th component denotes projection of the quantity onto the normal to the hypersurface n^μ. In this way we can write the Weyl scalars as

$$\begin{aligned}\Psi_4 = {} & R_{ijkl} \mathfrak{n}^i \overline{\mathfrak{m}}^j \mathfrak{n}^k \overline{\mathfrak{m}}^l + 2R_{0jkl} (\mathfrak{n}^0 \overline{\mathfrak{m}}^j \mathfrak{n}^k \overline{\mathfrak{m}}^l - \overline{\mathfrak{m}}^0 \mathfrak{n}^j \mathfrak{n}^k \overline{\mathfrak{m}}^l) \\ & + R_{0j0l} (\mathfrak{n}^0 \overline{\mathfrak{m}}^j \mathfrak{n}^0 \overline{\mathfrak{m}}^l + \overline{\mathfrak{m}}^0 \mathfrak{n}^j \overline{\mathfrak{m}}^0 \mathfrak{n}^l - 2\mathfrak{n}^0 \overline{\mathfrak{m}}^j \overline{\mathfrak{m}}^0 \mathfrak{n}^l)\end{aligned} \tag{3.28a}$$

where, for example, $R_{0jkl} = n^\alpha \perp^\beta_j \perp^\gamma_k \perp^\delta_l R_{\alpha\beta\gamma\delta}$. Using the ADM '3+1' decomposition, we can rewrite the projections of the full Riemann in terms of quantities defined on a single hypersurface (e.g., the spatial Riemann and Ricci tensors and the full extrinsic curvature) by

$$R_{ijkl} = \mathcal{R}_{ijkl} + 2K_{i[k}K_{l]j} \tag{3.29a}$$
$$R_{0jkl} = -2\left[\partial_{[l}K_{k]j} + \Gamma^p_{j[k}K_{l]p}\right] \tag{3.29b}$$

$$R_{0j0l} = \mathcal{R}_{jl} - K_{jp}K^{p}_{l} + KK_{jl}. \tag{3.29c}$$

We don't expand this farther into BSSN quantities since `MayaKranc` keeps a copy of ADM variables in memory that are updated after every timestep from the BSSN variables. It is more efficient and convenient to calculate the Weyl scalars in terms of the ADM quantities.

3.4.2 Tetrad Choice

The scalars as such are merely convenient quantities with which one can rewrite the Einstein equations. Given just the tetrad requirements of the Newman-Penrose formalism, we cannot say anything concretely concerning the interpretation of the Weyl scalars. By specifying a special tetrad, though, these quantities can be related to gravitational wave content in the far zone. In particular, Newman [141] showed a special behavior if you choose $\mathfrak{l}^{\mu}$ to be an "outgoing" vector in the null hypersurface of an asymptotically flat spacetime, $\mathfrak{n}^{\mu}$ as an "ingoing" vector on that same null hypersurface, and $\{\mathfrak{m}^{\mu}, \overline{\mathfrak{m}}^{\mu}\}$ to be in the angular directions of a 2-sphere. With such a tetrad, at some distance from the region of strong gravity the amplitude of Ψ_4 decreases with coordinate radius as $O\left(r^{-1}\right)$. Similarly, Ψ_3 decreases as $O\left(r^{-2}\right)$, Ψ_2 as $O\left(r^{-3}\right)$, Ψ_1 as $O\left(r^{-4}\right)$, and finally Ψ_0 decreases as $O\left(r^{-5}\right)$. Ψ_4 therefore has the radial dependence for radiation, but that is insufficient in and of itself.

The precise choice for these null vectors depends on what is convenient for the problem at hand, but it is standard for gravitational wave analysis to define $\mathfrak{l}^{\mu}$ as an "outgoing" null vector, $\mathfrak{n}^{\mu}$ as an "ingoing" null vector. The remaining two tetrad components, $\mathfrak{m}^{\mu}$ and $\overline{\mathfrak{m}}^{\mu}$, then span the angular directions. A particularly good way of seeing the roles of the Weyl scalars with such a tetrad is from the gravito-electric and gravito-magnetic formulation of the Weyl tensor [168]. By decomposing the Weyl tensor into electric and magnetic tensors it becomes easier to separate transverse and longitudinal portions of tensors. In a suitably chosen tetrad where $\mathfrak{l}^{\mu}$ is an outgoing null, Ψ_4 and Ψ_0 are then shown to be transverse. In such a tetrad, Ψ_4 can be interpreted as the "outgoing transverse" scalar while Ψ_0 is the "ingoing transverse" scalar. The "longitudinal" ingoing and outgoing scalars are then Ψ_1 and Ψ_3 respectively, and Ψ_2 is the mass/energy monopole. In such a tetrad where Ψ_4 is transverse, outgoing, and has the correct radial dependence, we can relate this quantity to gravitational radiation.

There are many explicit choices for the tetrad which display these characteristics, but with the finite grids of the Cauchy '3+1' decomposition the choice is particularly important. An obvious choice for perturbative studies is a tetrad lying along the principal null directions of the background spacetime's Weyl tensor. The perturbations in general vanish far from the area of interest, leaving the tetrad along the true principal null directions at distances where wave extraction is desired. Kinnersley [116] considered this and found a suitable analytic tetrad in Boyer-Lindquist coordinates, dubbed the Kinnersley tetrad [173]. Unfortunately, not all spacetimes allow an analytical and well-behaved Kinnersley tetrad, though attempts have been made to find "quasi-Kinnersley" tetrads that approximate the Kinnersley tetrad at large enough distances [50]. In

terms of a quasi-Kinnersley tetrad, the longitudinal Weyl scalars, Ψ_1 and Ψ_3, vanish while the Ψ_2 approaches a Kinnersley-tetrad value and the transverse scalars Ψ_0 and Ψ_4 differ from the values in a Kinnersley tetrad by only a complex factor.

The tetrad we use in this and other work uses a fiducial tetrad, created in a rather intuitive way to satisfy the criteria of Eqs. 3.25 and 3.26. We first assume that the '3+1' decomposition used allows a tetrad decomposition of the form

$$\mathfrak{l}^\mu = \frac{1}{\sqrt{2}}\left(n^\mu + r^\mu\right) , \tag{3.30a}$$

$$\mathfrak{n}^\mu = \frac{1}{\sqrt{2}}\left(n^\mu - r^\mu\right) , \tag{3.30b}$$

$$\mathfrak{m}^\mu = \frac{1}{\sqrt{2}}\left(\theta^\mu + \imath\varphi^\mu\right) \tag{3.30c}$$

where n^μ is the (normalized) normal to the hypersurface. The vectors r^μ, θ^μ, and φ^μ form an orthonormal *spatial* triad which we choose based on intuition for a standard 2-sphere on Minkowski and orthonormalize using the Gram-Schmidt method.

Being spatial, we can write the spatial four-vectors of the triad in terms of three-vectors. Let the spatial triad components take the form $r^\mu = \{0, v_3^i\}$, $\theta^\mu = \{0, v_2^i\}$, $\varphi^\mu = \{0, v_1^i\}$. Our initial guess for the set $\{v_1^i, v_2^i, v_3^i\}$ is for v_1^i to lie in the azimuthal direction and v_2^i to lie in the radial direction. We then create v_3^i from orthonormalization requirements. In Cartesian coordinates, this is

$$v_1^i = (-y, x, 0) , \tag{3.31a}$$

$$v_2^i = (x, y, z) , \tag{3.31b}$$

$$v_3^i = \sqrt{\det\gamma}\,\gamma^{ij}\epsilon_{jkl}v_1^k v_2^l \tag{3.31c}$$

We then apply the Gram-Schmidt process beginning with v_1^i. The order is important since v_1^i is affected the least by frame dragging. The resulting triad is

$$v_1^i \longrightarrow \frac{v_1^i}{\sqrt{\omega_{11}}} , \tag{3.32a}$$

$$v_2^i \longrightarrow \frac{\left(v_2^i - v_1^i\omega_{12}\right)}{\sqrt{\omega_{22}}} , \tag{3.32b}$$

$$v_3^i \longrightarrow \frac{\left(v_3^i - v_1^i\omega_{13} - v_2^i\omega_{23}\right)}{\sqrt{\omega_{33}}} \tag{3.32c}$$

where ω_{ij} is created from the various projections $\omega_{ij} := v_i^n v_j^m \gamma_{nm}$. Fiske *et al.* [80] showed this fiducial tetrad leads to an extracted wave which is convergent in the now standard numerical formulation and implementation, agreeing well with the analytical solutions of an outwardly propagating (linear) Teukolsky

wave [174].

3.4.3 Physics from Ψ_4

The Weyl scalar Ψ_4 is not, in itself, a useful physical quantity to interpret. It can, however, be used to generate easily interpretable information and is all that is necessary to calculate quantities vital to analyzing the evolution for future gravitational wave detection.

Multipolar Analysis It is standard procedure to decompose Ψ_4 onto spherical harmonics. Since Ψ_4 is a spin-2 psuedo-scalar, the standard spherical harmonics are not sufficient, so we decompose it onto spin-weighted spherical harmonics [142, 178] (see Appendix B for a discussion of spin-weighted spherical harmonics). There are several benefits to such a decomposition. First, this is a natural way of separating higher frequency (large l) contributions to Ψ_4 which contain more of the numerical noise. Second, considering our intuition and prior knowledge of symmetries, mode decompositions can aid in evaluating the validity and physicality of a particular numerical solution. Finally, the mode decomposition aids our understanding of system dynamics. Quasi-normal mode analysis of a distorted BH's ringdown, for instance, is based on the decomposition of waveforms into spin-weighted spherical harmonic modes. Additionally, the kicks seen in the final BHs of unequal mass and/or spinning BBH systems have been traced to asymmetric gravitational radiation in certain modes.

It can be shown that Ψ_4 is a spin -2 scalar (see Appendix B) so in the decomposition only $l \geq 2$ modes will contribute. The decomposition of Ψ_4 is then given by

$$\Psi_4 = \sum_{\ell=2}^{\infty} \sum_{m=-\ell}^{\ell} \mathcal{A}^{\ell,m} \left({}_{-2}Y^{\ell,m}(\theta,\varphi) \right) . \tag{3.33}$$

Inverting the relationship we calculate the mode coefficients $\mathcal{A}^{\ell,m}$ by

$$\mathcal{A}^{\ell,m} = \oint \Psi_4 \left({}_{-2}\overline{Y}^{\ell,m}(\theta,\varphi) \right) d\Omega \tag{3.34}$$

where $d\Omega$ is the standard solid angle element on a 2-sphere. For a detector at radius r_0, we interpolate Ψ_4 onto a sphere of radius r_0 from the Cartesian grid in the immediate vicinity and integrate as in Eq. 3.34.

Strain Waveform First and foremost in importance is the computation of the complex waveform strain, h, which is directly observable by gravitational wave observatories such as LIGO. In the transverse-traceless gauge, the strain can be decomposed as $h = h_+ - \imath h_\times$ where h_+ and $h_\times$ are the two polarizations of gravitational radiation. The complex strain is directly related to Ψ_4 by two time derivatives or, from the other point

of view, two integrations:

$$h = -\int_{-\infty}^{t} dt' \int_{-\infty}^{t'} \Psi_4 d\left(t''\right). \tag{3.35}$$

Note that the lower limit of the integral is *negative* infinity, which differs from our starting point. To account for this oversight, we need to find the constants of integration such that the strain starts at zero at $t = -\infty$ and ends at zero once the system has settled down to a final BH. In practice we find the constants of integration by fitting a line to the tail end of the waveform after the the radiation has propagated away, assuming there are sufficient points to get a good fit. In the remaining discussion we assume the constants of integration are taken into account as they are needed, for instance, to remove the sinusoidal modulation found in the radiated energy and angular momentum. In addition, to be completely accurate, all the quantities here should be calculated at infinity using a Ψ_4 that is extrapolated to infinity from an array of detectors far from the dynamical region.

Radiated Energy Between the asymptotic definitions of mass and momenta from Sec. 3.2 and the local definitions of mass and momenta from Sec. 3.3 are the energy and momenta carried to infinity by the gravitational radiation (see Ruiz *et al.* [160] for a good discussion on calculating radiated quantities). We approach extracting notions of energy and momentum from the viewpoint of a perturbation on an asymptotically flat hypersurface. As there are only two degrees of freedom in gravitational radiation (the two polarizations), we consider the gravitational wave as a transverse-traceless (TT) perturbation on flat space. That is, we assume a perturbation $g_{\mu\nu} = \delta_{\mu\nu} + \mathfrak{h}_{\mu\nu}$ where $\mathfrak{h}_{\mu\nu}$ is a TT tensor satisfying $\mathfrak{h}_{0\mu} = \mathfrak{h}^{i}{}_{i} = \nabla_j \mathfrak{h}^{ij}$ with ∇_j denoting the convariant derivative with respect to the background metric, flat space δ_{ij}.

The Isaacson stress-energy tensor [112] associated with such a perturbation in a locally inertial frame is

$$T_{\mu\nu} = \frac{1}{32\pi} \sum_{i,j} \left\langle \partial_\mu \mathfrak{h}_{ij}\, \partial_\nu \mathfrak{h}_{ij} \right\rangle \tag{3.36}$$

where $\langle\rangle$ denotes an average over several wavelengths. If we have, for instance, an outgoing wave in the z direction, $\mathfrak{h}_{ij}$ takes the form

$$\mathfrak{h}_{ij} = \begin{pmatrix} 0 & 0 & 0 & 0 \\ 0 & h_+ & h_\times & 0 \\ 0 & h_\times & h_+ & 0 \\ 0 & 0 & 0 & 0 \end{pmatrix} \tag{3.37}$$

with h_+ and $h_\times$ being the two gravitational degrees of freedom. Using this form of $\mathfrak{h}_{ij}$ the Isaacson stress-energy tensor becomes

$$T_{\mu\nu} = \frac{1}{16\pi} \left\langle \partial_\mu h_+ \partial_\nu h_+ + \partial_\mu h_\times \partial_\nu h_\times \right\rangle = \frac{1}{16\pi} \Re \left\langle \partial_\mu h\, \partial_\nu \overline{h} \right\rangle. \tag{3.38}$$

In the above we have also rewritten the Isaacson stress-energy in terms of the complex strain defined earlier

in this section. In our local Cartesian coordinates, the Isaacson stress-energy component T^{0r} is the energy flux in the radial direction:

$$\frac{dE}{dt\,dA} = T^{0r} = -\frac{1}{16\pi}\Re\left\langle \dot{h}\,\partial_r\overline{h}\right\rangle \tag{3.39}$$

where $dA = r^2 d\Omega$ is the area element normal to the radial direction and $\dot{h} = \partial_t h$. Since we have assumed an outgoing wave, the functional dependence of the perturbation is such that $h = f(r-t)/r$. This dependence lets us rewrite the radial derivative as a time derivative, $\partial_r h \simeq -\dot{h}$. Integrating over the entire sphere to get the total energy being radiated, we find

$$\frac{dE}{dt} = \lim_{r\to\infty}\frac{r^2}{16\pi}\oint \left|\dot{h}\right|^2 d\Omega. \tag{3.40}$$

Since $\Psi_4 = -\ddot{h}$, we can rewrite this energy in terms of Ψ_4

$$\frac{dE}{dt} = \lim_{r\to\infty}\frac{r^2}{16\pi}\oint \left|\int_{-\infty}^{t}\Psi_4 dt'\right|^2 d\Omega. \tag{3.41}$$

We utilize the decomposition onto spin-weighted spherical harmonics by calculating the energy instead from the mode coefficients, using only the lower order multipoles we've calculated and hence avoiding noise-ridden higher multipoles:

$$\frac{dE}{dt} = \lim_{r\to\infty}\frac{r^2}{16\pi}\sum_{\ell,m}\left|\int_{-\infty}^{t}A^{\ell,m}dt'\right|^2. \tag{3.42}$$

Radiated Angular Momentum The Isaacson method of deriving the radiated energy linearized the perturbation to first order in $1/r$ by averaging over several wavelengths, but angular momentum flux is of order $1/r^3$. In 1971, Bryce Dewitt first derived an expression for the flux of angular momentum from a gravitational wave of the form [178]

$$\frac{dJ^i}{dt\,dA} = \frac{1}{32\pi}\epsilon^{ijk}\left(x_j\partial_k \mathfrak{h}_{\mu\nu} + 2\delta_{\mu j}\mathfrak{h}_{\nu k}\right)\partial_r \mathfrak{h}^{\mu\nu}. \tag{3.43}$$

We write Dewitt's expression in more succinct form by utilizing the angular Killing fields of the background (flat) metric, $\boldsymbol{\xi}_i$. In Cartesian coordinates, the components of these vectors are $\xi_i^k = \epsilon_i^{jk}x_j$. Again assuming $\partial_r\mathfrak{h} = -\partial_t\mathfrak{h}$, we can then write the angular momentum more elegantly and intuitively as a Lie derivative of the metric perturbation along the Killing fields

$$\frac{dJ_i}{dt\,dA} = -\lim_{r\to\infty}\frac{r^2}{32\pi}\oint\left(\mathcal{L}_{\boldsymbol{\xi}_i}\mathfrak{h}_{\mu\nu}\right)\partial_t\mathfrak{h}^{\mu\nu}d\Omega. \tag{3.44}$$

Similar in fashion to the radiated energy calculation, we consider this first as Cartesian Killing vectors

in spherical coordinates (r, θ, φ) such that the Killing vectors are given as

$$\boldsymbol{\xi}_x = (0, -\sin\varphi, -\cos\varphi\cot\theta)\ , \tag{3.45}$$

$$\boldsymbol{\xi}_y = (0, \cos\varphi, -\sin\varphi\cot\theta)\ , \tag{3.46}$$

$$\boldsymbol{\xi}_z = (0, 0, 1)\ . \tag{3.47}$$

In order to calculate the Lie derivatives of $\mathfrak{h}_{\mu\nu}$ along these Killing vectors we need to first change basis. We introduce two complex vectors $\boldsymbol{\xi}_\pm := \boldsymbol{\xi}_x \pm \imath\boldsymbol{\xi}_y$ and an orthonormal spherical basis $\left(\hat{e}_r, \hat{e}_\theta, \hat{e}_\varphi\right)$ where we similarly define two complex vectors $\hat{e}_\pm := \left(\hat{e}_\theta \mp \imath\hat{e}_\varphi\right)/\sqrt{2}$. The Lie derivative of the new basis vectors $\hat{e}_\pm$ along $\xi_\pm$ is easily derived as

$$\mathcal{L}_{\boldsymbol{\xi}_\pm}\hat{e}^\mu_\pm = \mp\left(\imath e^{\pm\imath\varphi}\csc\theta\right)\hat{e}^\mu_\pm. \tag{3.48}$$

We can also rewrite the metric perturbation $\mathfrak{h}_{\mu\nu}$ in terms of the complex strain and the new basis vectors

$$\mathfrak{h}_{\mu\nu} = h\,(\hat{e}_-)_\mu\,(\hat{e}_-)_\nu + \overline{h}\,(\hat{e}_+)_\mu\,(\hat{e}_+)_\nu \tag{3.49}$$

Using both the above we can define angular operators for spin-weight s as $\hat{j}_\pm := \xi^\mu_\pm\partial_\mu - \imath s e^{\pm\imath\varphi}\csc\theta$ and find that

$$\mathcal{L}_{\boldsymbol{\xi}_\pm}\mathfrak{h}_{\mu\nu} = (\hat{e}_-)_\mu\,(\hat{e}_-)_\nu\,\hat{j}_\pm h + (\hat{e}_+)_\mu\,(\hat{e}_+)_\nu\,\hat{j}_\pm\overline{h}. \tag{3.50}$$

Noting that while h has a spin-weight of -2, it's complex conjugate has a spin-weight of +2,

$$\left(\mathcal{L}_{\boldsymbol{\xi}_\pm}\mathfrak{h}_{\mu\nu}\right)\partial_t\mathfrak{h}^{\mu\nu} = 2\Re\left\{\hat{j}_\pm h\,\partial_t\overline{h}\right\}. \tag{3.51}$$

A change of base and the definition of the Cartesian set of angular momentum operators $\hat{j}_i$ for spin-weight s as

$$\hat{j}_x = -\sin\varphi\,\partial_\theta - \cos\varphi\left(\cot\theta\,\partial_\varphi - \imath s\csc\theta\right)\ , \tag{3.52a}$$

$$\hat{j}_y = \cos\varphi\,\partial_\theta - \sin\varphi\left(\cot\theta\,\partial_\varphi - \imath s\csc\theta\right)\ , \tag{3.52b}$$

$$\hat{j}_z = \partial_\varphi \tag{3.52c}$$

yields the angular momentum flux

$$\frac{dJ_i}{dt} = -\lim_{r\to\infty}\frac{r^2}{16\pi}\Re\left\{\oint\partial_t\left(\overline{h}\right)\ \hat{j}_i h\,d\Omega\right\}. \tag{3.53}$$

As with the radiated energy, we can use the relation between the complex strain and Ψ_4 to write this in terms

of Ψ_4

$$\frac{dJ_i}{dt} = -\lim_{r\to\infty}\frac{r^2}{16\pi}\Re\left\{\oint\left(\int_{-\infty}^{t}\overline{\Psi}_4 dt'\right)\times\hat{j}_i\left(\int_{-\infty}^{t}\int_{-\infty}^{t'}\Psi_4 dt'' dt'\right)d\Omega\right\} \tag{3.54}$$

or similarly use the decomposition into spin-weighted spherical harmonics to rewrite this in terms of the mode coefficients

$$\frac{dJ_i}{dt} = -\lim_{r\to\infty}\frac{r^2}{16\pi}\Re\left\{\sum_{\ell,m}\sum_{\ell',m'}\int_{-\infty}^{t}\overline{\mathcal{A}}^{\ell',m'}dt'\times\int_{-\infty}^{t}\int_{-\infty}^{t'}\mathcal{A}^{\ell,m}dt''dt'\times\oint {}_{-2}\overline{Y}^{\ell',m'}\hat{j}_i\left({}_{-2}Y^{\ell,m}\right)d\Omega\right\} \tag{3.55}$$

Quasi-Normal Modes Analysis The final analysis quantity we utilize in this work are the quasi-local notions of mass and spin encoded in the ringdown portion of the waveform. After a merging BBH system has formed a common AH, the BHs can be seen from observers at spatial infinity as a single, highly distorted BH. This distorted BH can be viewed as undergoing a ringdown, shedding its distortion through the emission of gravitational radiation until it settles down into a stationary, possibly rotating BH (we disregard for the moment possible kicks). At some point in this process, the spacetime can be seen as a perturbation where the final BH system is the background metric. This is a regime where analytical approaches again bear fruit.

Just as bells have fundamental frequencies, or normal modes, at which they emit sound waves, so to do BHs have fundamental harmonics at which they emit gravitational waves when perturbed. The gravitational waveform emitted in the ringdown of a perturbed BH is approximated by a superposition of quasi-normal modes (QNMs) [118, 37] with a time dependence of $e^{\imath\omega t}$ where ω is complex frequency $\omega = \omega_{\ell mn} + \imath/\tau_{\ell mn}$. These modes are termed "quasi-normal" because the constant loss of energy from the system changes the nature of the modes so there is no truly complete set of modes. The real part of the frequency, $\omega_{\ell mn} = 2\pi f_{\ell mn}$ yields the real oscillations while $\tau_{\ell mn}$ is the damping time of the (ℓ, m, n) mode. The ℓ and m mode numbers choose the angular dependence of the mode while n refers to one (of infinite) overtones for an (ℓ, m) mode. Since the fundamental, $n = 0$, excitation has the longest damping time and will contribute the most to the signal detected at spatial infinity, we will ignore overtones in this work. In terms of its quasi-normal modes, the waveform can be decomposed as

$$\overline{h} = h_+ + \imath h_\times = \frac{M}{r}\sum_{\ell mn} C_{\ell mn} e^{\imath(\omega_{\ell mn}t+\phi_{\ell mn})} e^{-t/\tau_{\ell mn}} S_{\ell mn} \tag{3.56}$$

where $C_{\ell mn}$ are real constants and $S_{\ell mn}$ are spin-weighted *spheroidal* harmonics [36] which, for the fundamental ($n = 0$) mode of non-spinning BHs reduce to the spin-weighted *spherical* harmonics discussed above and in Appendix B. The puncture spacetimes we evolve are *not* Kerr spacetimes initially, but the gauge conditions used in the MPT underresolve the inner region enough that the system evolves to a nearly Kerr spacetime. Thus we find it sufficient to use the spin-weighted spherical harmonics ${}_sY^{\ell,m}$ as our basis.

During our standard mode analysis, as discussed above, we have the projection of Ψ_4 onto the set of spin-weighted spherical harmonics as a set of time-dependent mode coefficients $\mathcal{A}^{\ell,m}$. Since $\Psi_4 = -\ddot{h}$, we

can relate our generic mode decomposition to the quasi-normal mode decomposition

$$\mathcal{A}^{\ell,m} = (-1)^{m+2}\frac{M}{r}C_{\ell,-m}e^{-\imath\phi_{\ell,-m}}\left(\imath\omega_{\ell,-m} - \frac{1}{\tau_{\ell,-m}}\right)^2 e^{-\imath\left(\omega_{\ell,-m}+1/\tau_{\ell,-m}\right)t} \tag{3.57}$$

Since we are just interested in the time dependence of the complex coefficients $\mathcal{A}^{\ell,m}$, we find it easiest to consider its amplitude and phase as a function of time

$$\left|\mathcal{A}^{\ell,m}\right| \propto e^{t/\tau_{\ell,m}}, \tag{3.58a}$$

$$\arg\mathcal{A}^{\ell,m} \propto -\omega_{\ell,m}t. \tag{3.58b}$$

Thus, given a mode decomposition of Ψ_4 onto a basis of spin-weighted spherical harmonics, we can find $\tau_{\ell,m}$ from the slope $\ln\left|\mathcal{A}^{\ell,m}\right|$ and $\omega_{\ell,m}$ from the slope of $\arg\mathcal{A}^{\ell,m}$. These two quantities specify the full complex frequency for the (ℓ, m) mode.

The complex frequency for a quasi-normal mode depends on both the mass and spin of the final BH. In Chapter 4 we use the quasi-normal modes to find the spin given the final mass of the system, which we acquire using the radiated energy and energy conservation. From the final mass $\mathcal{M}$ and the complex frequency, we can construct the dimensionless quantity $\mathcal{M}\omega$ and compare this to analytical calculations of Kerr quasi-normal frequencies. In Appendix D of Berti *et al.* [37] there is a table of such frequencies for a range of spins. Interpolation across the spins gives us a function $j(\mathcal{M}\omega)$ for evaluating the spin of the final BH.

Other Quantities The radiated linear momentum can be calculated from the Isaacson stress-energy tensor method in a fashion similar to the radiated energy. This is useful for unequal or spinning BBH systems where the asymmetric gravitational radiation gives a "kick" to the final BH. In this dissertation, though, we do not consider BBH systems from which kicks are expected and therefore do not compute the radiated linear momentum in our analyses.

3.4.4 Comments on Ψ_4 Analyses

A recent joint analysis by Lindblom *et al.* [124] derives the accuracy requirements for parameter estimation and general signal detection (the complex strain) using numerically-generated, analytical, or hybrid numerical-analytical waveforms. Lindblom's study was not released until after the study of Ch. 4 was published. Our analysis of the waveform accuracy for data analysis in Ch. 5 remains rudimentary in light of this, but it is sufficient for the purposes of producing waveforms for LIGO. The comparisons performed, though, were for the purpose of evaluating the *numerical* waveform's robustness with only a rough calculation in Ch. 5 of what these results imply for data analysts.

The reader might have noticed the number of assumptions and requirements in the derivation of above.

Succinctly, these assumptions are:

- We calculate Ψ_4 far enough away that we can assume peeling (i.e. a pure amplitude fall-off of $1/r$), an assumption which can be readily tested by extracting at many radii).
- Asymptotic flatness
- The tetrad as derived truly exhibits all the properties it is constructed for (i.e. we neglect numerical error in its calculation).
- The fiducial tetrad constructed is truly sufficient to allow the interpretations of the Weyl scalars to hold.

Recently Lehner and Moreschi [121] published a careful study of the delicacy in using the Weyl scalars for wave extraction due to small violations of the above assumptions. Given the agreement between waveforms calculated as above across different implementations, the necessary corrections are unlikely to be large *for the systems currently studied*. Nonetheless, it should be kept in mind and might prove important in satisfying Lindblom *et al.*'s stringent accuracy requirements.

Chapter 4

The Effects of Spurious Radiation on Binary Black Hole Mergers

> "A single rogue wave has certainly been known to spell disaster for the mariner." – NWS Ocean Prediction Center

The coalescence of two black holes, long thought of as the holy grail of NR, is well on its way to being a solved problem. Many groups in NR have now demonstrated the ability to follow two black holes through several orbits [150] and their final orbits and merger to a single black hole [155, 27, 55, 103, 92, 119, 181]. From the first published waveform of equal-mass, non-spinning BBH coalescence, the simplicity of the waveform's dependence on time has been noted. Comparisons amongst the groups in NR have demonstrated a remarkable agreement to the solution of the BBH problem. A common aspect in all numerical relativity BBH evolutions is the presence of spurious radiation in the initial data. In this chapter, we present a study on how the standard equal-mass, quasi-circular BBH system responds to the presence of spurious radiation that has been added in a controlled manner and map that response as a function of the radiation's initial conditions. Our intent is to determine how much junk radiation the system can handle and how the waveforms and the physical properties of the final black hole deviate from the standard BBH result.

Several papers have compared BBH waveforms. One of the first papers to internally compare waveforms also demonstrated the first evidence of "universality"[26] in an equal-mass, non-spinning initial configuration. In the paper, Baker *et al.*demonstrated that differences in initial data characterized by a change in the initial orbital separation manifested as a time shift in the amplitude and phase of the gravitational waveforms. Once time-shifted, the waveforms were within 1% agreement over the merger and ringdown in $|r_0\Psi_4|$. We investigate the effect that the additional spurious radiation we add to the binary will have on this universality.

The first comparison of NR waveforms between several groups [25] includes the most popular methods used in the community to evolve BBHs. This includes excision with a hyperbolic formulation [155]

and moving punctures with the Baumgarte-Shapiro-Shibata-Nakamura (BSSN) formulation of the Einstein equation [27, 55]. The waveforms were in remarkable agreement once time-shifted, the largest differences, occurring at the beginning of the wave, being due to the spurious radiation in the initial data. A second, independent comparison of waveforms from different methods was conducted by Sperhake [169] in which he compared a Kerr-Schild/excision evolution to a puncture evolution within the same code. An interesting question is to what extent the spurious radiation in the initial data could cause differences in the merging time and thus affect waveform comparisons based on time-shifts to align the amplitude of the waveform.

Most groups remove the initial burst from the waveform during post-processing of the data [56, 60]. From the evolutions published, it appears that the spurious radiation that is present in the initial data is flushed out of the system within a crossing time, leaving the binary dynamics mostly untouched. There is still some concern about the impact that choices made in setting up the initial data for the evolutions, choices such as conformal flatness, have on the waveforms. Studies have looked at different ways of choosing the freely specifiable part of initial data [99, 128] which reduce the amplitude of the spurious radiation, but these have not been extensively implemented in the evolutions leading to the currently forming waveform template banks.

In this chapter, we test the robustness of the binary to the effects of spurious radiation. To this end we create a BBH system containing additional radiation with tunable initial energy initialized at the binary's center of mass. We then evolve a series series of spacetimes with a standard equal-mass, non-spinning, quasi-circular BBH system plus additional radiation using the PSU numerical code, `MayaKranc`, which implements the MPT [27, 55]. The initial data used to construct the modified BBH spacetime is presented in Section 4.2, the results in Section 4.3 and the conclusions in Section 4.4. Our main result is that the presence of spurious radiation causes a hastening of the merger, thus plausibly accounting for the differences in merger times seen in the NR waveform comparisons.

4.1 A Newtonian Perspective

Before describing our numerical experiment, we present a back-of-the-envelope calculation to build our intuition about this problem. For illustrative purposes, we investigate the effect a central pulse of energy might have on a binary by studying a two-body orbit in Newtonian gravity with a stationary mass placed at the orbit's center of motion while the bodies are at their apocenter. The addition of the third mass at the center of the Newtonian binary affects the orbit by deepening the potential in which the binary sits. We solve the problem using the standard central force solution to the two-body problem with the new potential. We assume $\dot{r} = 0$ initially since this is also assumed in our initial data for the standard quasi-circular BBH systems. Letting m be the masses of the black holes and m_w be the equivalent mass of the third body, we

write the ratio of the final eccentricity, e', to the original eccentricity as

$$(\frac{e'}{e})^2 = \frac{1}{(1+2f)^2}[1 + \frac{(4-2j^2/\mu d)f + 4f^2}{e^2}] \tag{4.1}$$

where $f = m_w/m$ is the fractional mass, $j = l/\mu$ is the angular momentum per unit reduced mass, and d is the initial separation of the binary.

This simple calculation indicates that, for sufficiently small eccentricities, the eccentricity increases. For the binary parameters studied herein, the eccentricity invariably increases for $e \leq 0.88$. Although the black holes in our BBH evolutions are not far enough apart to allow a valid determination of eccentricity, the trajectories are quasi-circular enough for the eccentricity to be low. This illustrates that, by adding extra gravitational radiation into the center of the studied system, we can expect the binary's orbit to become more eccentric.

4.2 Injecting Radiation into a BBH Evolution

We inject gravitational radiation into the standard, equal-mass, non-spinning, quasi-circular BBH evolution during the setup of the initial data. The initial data for the evolution is constructed via the puncture method [43] using the single-domain spectral method code developed by Ansorg *et al.*. [13] which assumes a conformally flat spacetime in solving the constraints. We have two building blocks for the data: 1) the quasi-circular BBH and 2) the tunable radiation. The BBH data is set-up using the input conditions for the Baker *et al.* [26] R1 run of two equal-mass irrotational black holes in quasi-circular orbits. The details of the R1 initial data are given in the first row of Table 4.1 and a convergence study was done in [183].

4.2.1 The Teukolsky-Nakamura Wave

The tunable wave is given by an even parity, quadrupolar gravitational wave: the linearized solution to a perturbation on Minkowski spacetime expanded over the modes of the Matthews tensor spherical harmonics [178] (see Appendix B for discussion and Appendix C for complete derivation). This wave was first derived by Teukolsky [174] and is typically known as a Teukolsky wave. The tensor which embodies the wave is the general traceless-transverse solution to the linearized Einstein equations. While Teukolsky [174] derived and wrote out the $\ell = 2$ wave explicitly, Nakamura and Oohara [140] later wrote out the solution for general ℓ and m modes. Instead of using the wave as a *spatial metric* perturbation, Nakamura and Oohara manifested their wave as an extrinsic curvature perturbation. In this study we implement the Nakamura version of the Teukolsky wave, herein called Teukolsky-Nakamura waves (TNWs), in order to satisfy the condition of a conformally flat metric imposed by the puncture method .

The Teukolsky-Nakamura (TN) extrinsic curvature tensor, as derived in Appendix C, is given by

$$\tilde{A}_{ij}^{\rm TN} = \sum_{\ell,m} \begin{pmatrix} a_{\ell,m}Y^{\ell,m} & b_{\ell,m}Y^{\ell,m}_{\theta} & b_{\ell,m}Y^{\ell,m}_{\varphi} \\ * & g_{\ell,m}Y^{\ell,m} + f_{\ell,m}W^{\ell,m} & f_{\ell,m}X^{\ell,m} \\ * & * & (g_{\ell,m}Y^{\ell,m} - f_{\ell,m}W^{\ell,m})\sin^2\theta \end{pmatrix} \tag{4.2}$$

where the coefficients $a_{\ell,m}$, $b_{\ell,m}$, $f_{\ell,m}$, and $g_{\ell,m}$ are functions only of the coordinate radius and time r, t as follows

$$a_{\ell,m} = r^{\ell-2}\left(\frac{1}{r}\partial_r\right)^{\ell}\frac{F(t-r)+F(t+r)}{r}, \tag{4.3a}$$

$$b_{\ell,m} = \frac{1}{\ell(\ell+1)r}\partial_r(r^3 a_{\ell,m}), \tag{4.3b}$$

$$g_{\ell,m} = -\frac{r^2}{2}a_{\ell,m}, \tag{4.3c}$$

$$f_{\ell,m} = \frac{1}{(\ell-2)(\ell+1)}\left[g_{\ell,m} + \partial_r\left(\frac{r}{\ell(\ell+1)}\partial_r(r^3 a_{\ell,m})\right)\right] \tag{4.3d}$$

and the angular functions $X^{\ell,m}$ and $W^{\ell,m}$ are

$$X^{\ell,m} = 2\partial_\varphi\left(\partial_\theta - \cot\theta\right)Y^{\ell,m}, \tag{4.4a}$$

$$W^{\ell,m} = \left(\partial_\theta^2 - \cot\theta\partial_\theta - \frac{1}{\sin^2\theta}\partial_\varphi^2\right)Y^{\ell,m}. \tag{4.4b}$$

Note that the TN solution lets us choose the radial dependence in the form of ingoing and outgoing functions which we have chosen to be the same symmetric functional form, $F(u)$. Our $F(u)$ is given by an Eppley packet [74]:

$$F(u) = Aue^{-u^2/\sigma^2}, \tag{4.5}$$

where $u = t \pm r$. The Eppley packet is a localized, smooth Gaussian packet with an extra factor of u present to ensure the wave is regular at the origin. This packet constitutes the bulk of our parameter space studies, but we later discuss the effects of modulating the Eppley packet by a cosine. Thus the TN solution gives us the freedom to choose the location, mode content, strength, and radial dependence of the injected radiation. Since the extrinsic curvature is real and the spherical harmonics are complex, we take only the real part of the TN tensor resulting in a superposition of m and $-m$ modes in our TNW.

4.2.2 BBH+TNW Initial Data

We add the TNW tensor to the extrinsic curvature such that our initial data $\{\gamma_{ij}, K_{ij}\}$ is

$$\gamma_{ij} = \psi^4\delta_{ij}, \tag{4.6a}$$

$$K_{ij} \quad = \quad \psi^{-2}(\tilde{A}^{BY}_{ij} + \tilde{A}^{TN}_{ij})\,, \tag{4.6b}$$

where δ_{ij} is the flat spatial metric and ψ is the conformal factor which satisfies the Hamiltonian constraint under York's conformal approach [192]. The extrinsic curvature $\tilde{A}^{BY}_{ij}$ is the Bowen and York solution [42] to the momentum constraint given in Eq. 3.12 and $\tilde{A}^{TN}_{ij}$ is the TN tensor. Notice that because the momentum constraint is linear in the extrinsic curvature, the superposition of the extrinsic curvatures also satisfies the momentum constraint. As a test case we evolved the above initial data with a vanishing Bowen-York tensor, i.e. Minkowski background. For the $\ell = 2$, $m = \pm 2$ case, we found that the Arnowitt-Deser-Misner (ADM) angular momentum $\mathcal{J}_{\rm ADM}$ calculated on the initial spacetime is zero to within machine error. The angular momentum of the BBH+TNW is therefore independent of the TNW to our numerical accuracy.

4.2.3 Configurations

The simplest geometry in which we can add additional spurious radiation to our BBH initial data is a wave pulse at the BBH's center of mass. We typically choose an $\ell = 2$, $m = 2$ mode, coinciding with the dominant mode for gravitational radiation from a BBH system, and vary the amplitude, A, and width, σ, of the Eppley packet. The values of σ/M are chosen from the set {0,3,4,5,6} and those of the amplitude A/M^3 from the set {0,0.1, 0.5, 1.0, 1.5} where the dry R1 BBH spacetime is recovered when $A/M^3 = 0$. Fig. 4.1 shows the shape of the wave in one of the components of the traceless-transverse extrinsic curvature, $A_{ij} = \psi^{-2}\tilde{A}_{ij}$, along the coordinate axis intersecting the two black holes, modulated by the inverse square of the conformal factor, for $A = 1M^3$ and $\sigma = 3M, 4M, 5M, 6M$.

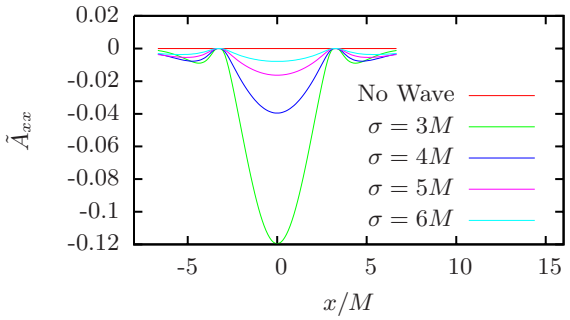

Figure 4.1. Comparison of the initial $\tilde{A}_{xx}$ between the Eppley packet widths, σ, for a wave amplitude of $1M^3$ added to the R1 BBH system. Being the *conformal* extrinsic curvature, this includes a modulation by $1/\psi^2$ so $\tilde{A}_{xx}$ vanishes at the punctures.

When adding the TNW to the spacetime we wanted to keep the initial black holes unaltered. We chose to keep the AH masses constant independent of the additional wave content. In practice the AH masses varied by as much as 0.04% from the R1 run without extra wave content (dry R1) due to insufficient parameter accuracy. The momenta remain constant as parameters to the initial data solver, and the ADM angular

momentum differs by at most 0.001% from the dry R1 run. The second column of Table 4.1 lists the ADM energy $\mathcal{E}_{\rm ADM}$ of the spacetime for each wave choice. We note that the waves increase the ADM energy from a negligible 10^{-4}% to a significant 8.9%, which scales empirically as $\mathcal{E}_{\rm ADM} \simeq A^2/\sigma^5$. The proper separation between the black holes changes from the dry case of $L = 9.94$ to a maximum of $L = 10.23$. In the most extreme case, the wave having $A = 1.5M^3$ and $\sigma = 3M$, we have added almost 9% additional energy into the BBH system and effectively moved the black holes apart by $0.29M$. The impact of these differences in initial data on the binary evolution are discussed further in the next section.

Pumping energy into the system while holding the coordinate separation and angular momentum constant necessarily means that we are changing the binding energy of the system. To study this change we map the effective potentials for each BBH+TNW case. We do this by repeatedly solving the initial data with incremented separations while holding the individual AH masses and total ADM angular momentum fixed. We calculated the quantity $E_b = \mathcal{E}_{\rm ADM} - \mathcal{M}_{\rm AH,1} - \mathcal{M}_{\rm AH,2}$ for each spacetime. The wave itself adds to the ADM energy and must be subtracted in this calculation; but, as we're only interested in the relative shapes, we can look at the relative binding energy, $E_b - E_{b,\rm min}$. For the waves with a σ of $4M$ the binding energy per unit reduced mass is plotted in Fig. 4.2 with a vertical line indicating the initial coordinate separation of the black holes. We can immediately see that the dry "quasi-circular" R1 case has some non-zero eccentricity as the imposed separation does not lie at the minimum of the curve. We also observe a shift of the minimum inwards as the wave strength increases. Since the coordinate separation in the parameter search is held fixed for the evolved initial data, the location of the system along the binding energy curve with respect to its minimum is sufficient to see that the eccentricity of the orbit is likely increasing. Unfortunately, the separation is too small to get a reliable measure of the eccentricity.

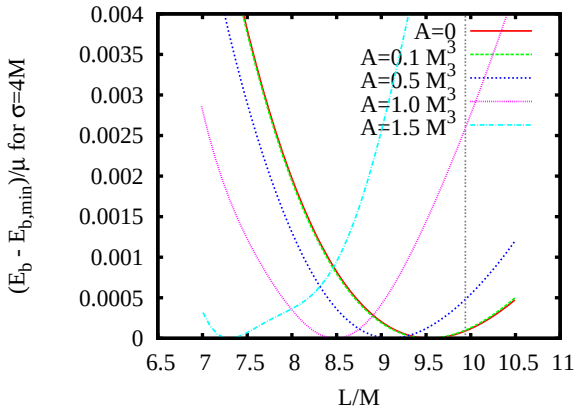

Figure 4.2. We plot the effect of the TNW on the binding energy per unit reduced mass in the initial data. The potentials were calculated by solving the initial data using Ansorg's code for various separations while keeping the individual AH masses and total ADM angular momentum fixed.

4.3 Evolutions of the BBH+TNW

Our simulations of the BBH+TNW initial data are summarized in Table 4.1, where the first row corresponds to the BBH system without added radiation, the dry R1 run. This will be our control case. We systematically evolved each BBH+TNW spacetime, varying A and σ of the TNW. We divide the results from evolving these simulations into four subsections: the main result concerning the merger time in § 4.3.1, the dynamical and radiated quantities from our runs are in § 4.3.2, the final spacetime quantities in § 4.3.3, and a comparison of the gravitational waves by time-shifting in § 4.3.4.

4.3.1 Merger Time

The main result of adding gravitational radiation to our BBH evolution is to hasten the merger of the black holes. With increasing $\mathcal{E}_{\rm ADM}$, the binary invariably merges *faster*. The sixth column in Table 4.1 lists the differences in merger times between the dry R1 and the BBH+TNW runs given by $\Delta T = (T_0 - T_{0,\rm dry})/M$. The time, T_0, is given in units of the total, initial AH masses of the black holes and evaluated at the peak amplitude of each waveform extracted at a radius of $75M$. The use of the waveform peak variation as a measure of the change in merger time agrees within a few percent in ΔT to the variation in the time it takes for the punctures to be separated by one grid spacing.

Figs. 4.3 and 4.4 show the change in merger times from the perspective of constant wave amplitude and constant pulse width. We can see that there is a strong dependence on the width of the pulse as well as the amplitude. Some cases show a positive value for ΔT; however, these are all equal to zero within the errors. For all the $A = 1M^3$ waves that have non-zero merger time we found an approximate power law relation between the width of the pulse and the change in merger time:

$$\Delta T(A = 1M^3) \propto \sigma^{-4.93} . \tag{4.7}$$

A more general look at the change in merger times is found in Fig. 4.5. Given our estimated error bars, significant changes in merger time occur when the TNW has increased the initial ADM energy of the spacetime by about 1% compared to that of the dry R1.

To isolate how much of ΔT is due to the additional spurious radiation introduced and how much is due to other factors, we perform a series of tests. We focus on the most significant sources of errors, namely the resolution of our grid, wave extraction radius, the change in proper distance in setting up the initial data, and the change in mass of the two black holes. We will look at each of these factors and assess their individual contribution to ΔT.

1. Resolution: The finest resolution for the simulations we present in Table 4.1 is $M/38.4$. We check the error due to the resolution by repeating several cases with finest resolutions of $M/44.8$ and $M/51.2$. We ran convergence tests on the strongest wave ($A = 1.5M^3$, $\sigma = 3M$) and the weakest wave ($A = 0.1M^3$, $\sigma = 6M$). A third, medium, wave with $A = 0.5M^3$ and $\sigma = 4M$ was run at just one more resolution, $M/44.8$. For all

Run Summary

A/M^3	σ/M	$\mathcal{E}_{\rm ADM}$	$E_{rad}/\mathcal{E}_{\rm ADM}$	$J_{rad}/\mathcal{J}_{\rm ADM}$	$\Delta T/M$	$\mathcal{M}_{AH}^{(f)}$	j_f
0.0	0	0.9957	0.0359	0.273	0.0	0.9599	0.682
0.1	3	0.996	0.0363	0.273	-0.6	0.9600	0.683
0.5	3	1.007	0.0451	0.271	-16.4	0.9609	0.682
1.0	3	1.037	0.0708	0.263	-56.1	0.9635	0.686
1.5	3	1.084	0.1058	0.244	-88.4	0.9696	0.693
0.1	4	0.996	0.0360	0.274	+1.5	0.9596	0.682
0.5	4	0.999	0.0385	0.272	-4.7	0.9604	0.682
1.0	4	1.007	0.0463	0.272	-14.3	0.9603	0.683
1.5	4	1.021	0.0589	0.270	-31.8	0.9607	0.683
0.1	5	0.996	0.0360	0.273	+0.2	0.9599	0.682
0.5	5	0.997	0.0369	0.273	-0.1	0.9599	0.682
1.0	5	1.000	0.0399	0.272	-4.6	0.9603	0.683
1.5	5	1.005	0.0448	0.272	-7.8	0.9599	0.686
0.1	6	0.996	0.0359	0.273	+0.2	0.9599	0.682
0.5	6	0.996	0.0364	0.273	+0.7	0.9599	0.682
1.0	6	0.998	0.0377	0.273	-0.3	0.9601	0.682
1.5	6	1.000	0.0399	0.272	-2.2	0.9602	0.682

Table 4.1. The first two columns are the parameters of the TNWs followed by the ADM energy of the initial spacetimes. Column 4 and 5 give the fraction of the ADM energy and angular momentum radiated over the simulation. Column 6 is the change in merger time calculated by the shift in extracted waveform peak in units of the total AH mass in the initial spacetime. Column 7 lists the final mass and Column 8 the final spin, $j_f = a_f/\mathcal{M}_{AH}^{(f)}$ of the black hole.

three cases, the merger time *decreased*. The merger time of the compact wave decreased little for a total of $0.1M$ over the three resolutions while the diffuse wave decreased more drastically for a total of about $0.5M$. The medium case had a $0.2M$ difference between the two resolutions.

2. Extraction Radius: The next source of error is wave extraction radius. In NR, waveforms are usually calculated in terms of the Newman-Penrose scalar, $\Psi_4(t,x,y,z)$, which are extracted on a sphere at a finite radius some distance from the source, then expanded into angular modes via the spin-weighted spherical harmonics, ${}_{-2}Y^{\ell,m}(\theta,\phi)$. With a proper choice of tetrad, this scalar is a measure of outgoing gravitational radiation. There has been recent work investigating the effects the choice of extraction radius can have on the correctness of the waveform [147, 121]. As the extraction radius increases, the errors caused by an incorrect tetrad and finite distance diminish. While it is still an open question whether or not there are observable effects from the methods groups currently use to extract the waveforms, the methodology of the extraction is not thought to contaminate the waveform. An indication the appropriate tetrad is being approached is that the waveform amplitude scales as $1/r$, which we tested. To get a rough estimate of the errors due to extracting at a finite radius, we compute ΔT using radiation extracted at $30M$ and extracted at $75M$. In Fig. 4.6 we plot the amplitude of the dominant waveform mode, $|\Psi_4^{2,2}|$, extracted at the two radii for both

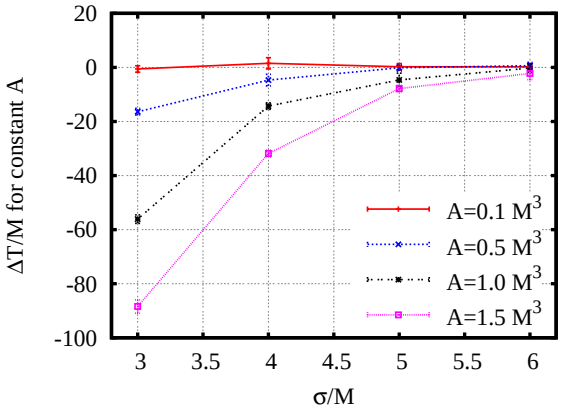

Figure 4.3. Changes in merger times compared to the dry R1 run as a function of packet width with estimated error bars.

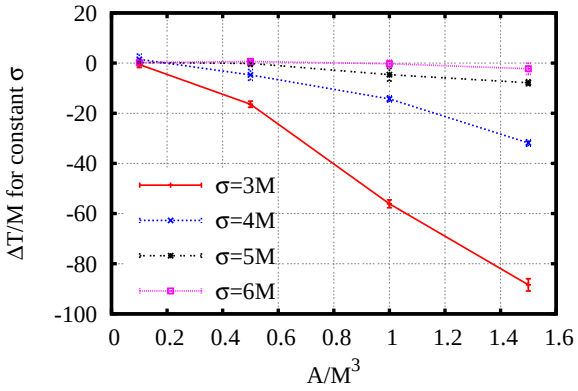

Figure 4.4. Changes in merger times compared to the dry R1 run as a function of wave amplitude with estimated error bars.

the dry R1 run and one where the merger time changed significantly. The merger time shift changed by no more than $0.4M$ between the two extraction radii.

3. Black Hole Mass: Aside from unphysical sources of error, the small differences in the initial data also change the merger time. Though we kept the initial AH masses nearly identical, there is still a variation of up to 0.04% compared to the dry R1 run. While conducting the research for this study, we found that a 0.14% change in initial AH masses of the punctures resulted in a change in merger time of $6.7M$. Although we do not include simulations with such a large deviation of masses, we used this knowledge and assumed the change in merger time was linear in the change in initial mass to estimate an error.

4. Proper Separation: As mentioned in § 4.2, the presence of the additional gravitational radiation also increased the proper separation, L, from the dry R1 $9.94M$ by up to 2.9%. We studied the effect of

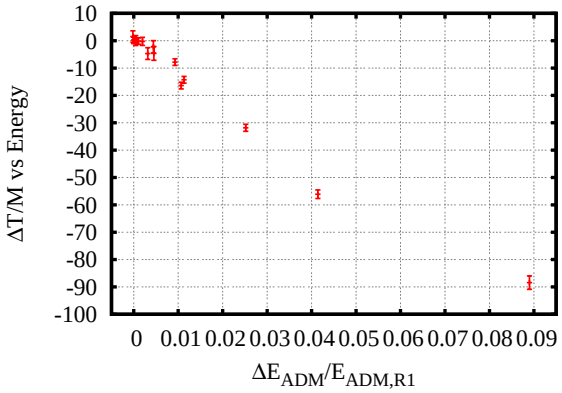

Figure 4.5. Changes in merger times compared to the fractional change in initial ADM energy of the spacetime with estimated error bars.

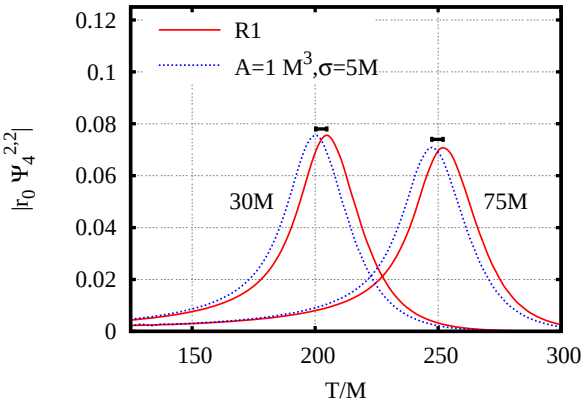

Figure 4.6. Sample comparison of waveforms extracted at different radii. Plotted are the waveforms for the dry R1 run and $A = 1M^3$, $\sigma = 5M$ run extracted at $30M$ and $75M$.

this change by evolving two BBH spacetimes with the same initial masses and angular momentum but increasing the coordinate to yield proper separations of $10.24M$ and $10.10M$. The merger time changed by at most $2.1M$. We assumed a linear relationship between the ΔT and ΔL in estimating the errors from this source at each data point.

The error bars presented in our figures are calculated by adding all the errors in quadrature:

$$\begin{aligned} \Sigma_{\Delta T}^2 &= \Sigma_T^2 + \Sigma_{T_0}^2 \\ \Sigma_T^2 &= (\frac{\Delta T}{\Delta L}\Delta L)^2 + (\frac{\Delta T}{\Delta m}\Delta m)^2 + \Sigma_{\rm res}^2 + \Sigma_{\rm tet}^2 , \end{aligned} \tag{4.8a}$$

where $\Sigma_{\Delta T}$ is the error in ΔT, Σ_T is the error in T, and Σ_{T_0} is the error in T for the dry R1 run. $\Sigma_{\rm res} = 0.75$

A/M^3	σ/M	$k \cdot M$	m	$E_{rad}/\mathcal{E}_{\mathrm{ADM},i}$	$J_{rad}/\mathcal{J}_{\mathrm{ADM},i}$	$\mathcal{M}_{AH}^{(f)}$	$\Delta T/M$
1	3	0	2	0.0696	0.252	0.970	-65.5
0.25	3	0	2	0.0382	0.272	0.970	-5.6
0.15	3	0	0	0.0382	0.271	0.961	-6.9
3×10^{-3}	4	2	2	0.0363	0.272	0.962	-4.5
7×10^{-4}	4	3	2	0.0358	0.272	0.962	-4.0
Dual 0.5	4	0	2	0.0411	0.271	0.960	-8.9

Table 4.2. Overview of the odd runs. The left four columns are the wave parameters, followed by the fraction of ADM energy radiated and the fraction of the ADM angular momentum radiated. The final masses are given in the 7th column followed by the merger time change as derived by the peak of the waveform extracted at $75M$.

and $\Sigma_{\mathrm{tet}} = 0.4$ are the largest measurements for the resolution and extraction radius errors. The accumulated errors do not account for the observed ΔT when $\mathcal{E}_{\mathrm{ADM}}/\mathcal{E}_{\mathrm{ADM,R1}} > 0.01$ and we note that the errors grow as the amplitude increases and the width decreases, most notably the errors associated with changes in the irreducible masses.

The parameter space of adding spurious radiation is large. In Table 4.2, we present the results from a few evolutions outside of our main parameter survey. The junk radiation present in the initial data of a typical BBH simulation may not be well represented by an $\ell = m = 2$ mode. Similarly the effect of the junk radiation might be sensitive to the wavelength of the pulse. In order to test how important a modulation in the frequency might be to our conclusions, we briefly investigated an Eppley packet modulated with a cosine wave, given by

$$F(u) = A\cos(ku)ue^{-u^2/\sigma^2}\,. \tag{4.9}$$

This modulation adds an extra parameter controlling the wavelength of the perturbation. We adjusted the amplitude of the wave to keep the energy approximately comparable to our standard runs. The resulting simulation merger time differed from the unmodulated packet by less than $1M$ in T, well within error bars. While this is still an avenue open to investigation, we concluded that the modulation was not affecting the results enough to warrant an additional parameter in our survey. We also conducted a test of the geometry of the wave by initiating a pulse with an $\ell = 2$, $m = 0$ mode. Again we changed the amplitude so that the energy in the wave was approximately constant and found that there was a change in merger time of $1M$ compared to the $\ell = 2$, $m = 2$ simulation, again within error bars. This points towards the wavelength and angular dependence of the pulse being secondary to the additional energy in determining the effect of the pulse on the merger time.

Finally, to make a stronger connection to the junk radiation being associated with each puncture, we added *two* identical waves centered at each of the black holes rather than at the center. Compared to the same wave initiated at the center, the dual waves added almost twice the energy and almost doubled the change in merger time, which is consistent with the center-of-mass TNW.

4.3.2 Dynamical and Radiated Quantities

We now investigate the effects of the TNWs on the radiated quantities derived from the waveforms. We calculate these quantities from the Weyl scalar Ψ_4 assuming, as in the calculation of the waveform, the fiducial tetrad of Baker *et al.*. [24] (see Sec. 3.4). A summary of the quantities obtained from Ψ_4 are listed in Table 4.1. The fraction of the initial ADM energy radiated was calculated across a detector at $40M$. As expected, the radiated energy increases with the strength of the wave. When $A < 0.5M^3$ and $\sigma \geq 5M$, there is no measurable difference between the BBH+TNW and the BBH cases within numerical error. For those cases, we can only conclude that the energy in the wave propagates out without a measurable interaction with the black holes. Similarly a trend emerges as we increase A for each σ, which corresponds to increasing $\mathcal{E}_{\rm ADM}$. The radiated angular momentum consistently decreases.

To look at the interaction of the TNW with the black holes as it propagates out, we study the radiated energy and angular momentum as functions of time. In Fig. 4.7 we plot the energy radiated across a detector at radius $r = 40M$. We see the energy grows from a time of $40M$ to around $80M$ as the initial burst of spurious radiation passes the detector. After this burst of energy the remaining energy radiated is approximately $0.035\mathcal{E}_{\rm ADM,R1}$ and is almost uniform across the various cases. From this we can see that most of the energy introduced in the spacetime is quickly flushed out of the system, leaving a system which radiates a further amount of energy that is independent of the junk radiation.

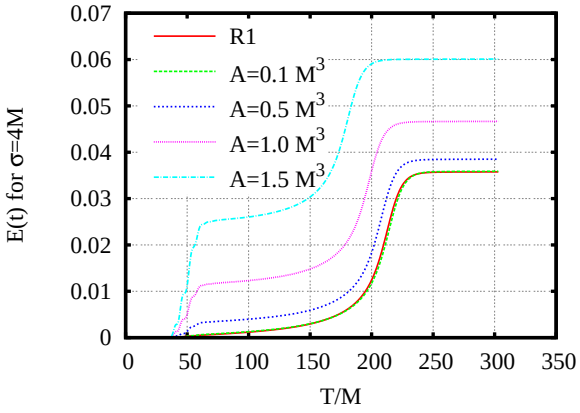

Figure 4.7. Energy radiated across a sphere of radius $r = 40M$ as calculated from the Weyl scalar Ψ_4.

All the evolutions started from spacetimes with equal $\mathcal{J}_{\rm ADM}$ since the TNW does not add angular momentum to the BBH spacetime. In column five of Table 4.1 and in Fig. 4.8, we see that the amount of angular momentum radiated across a detector located at $40M$ is independent of the wave with some numerical error. The difference in J_{rad} between the runs lies in *when* the system radiates the angular momentum. This is better seen in Fig. 4.9 where we present the angular momentum flux across the sphere at $r = 40M$ and in Fig. 4.10, a close-up of the initial part of the data. The spurious radiation is transporting extra angular

momentum as it is flushed out.

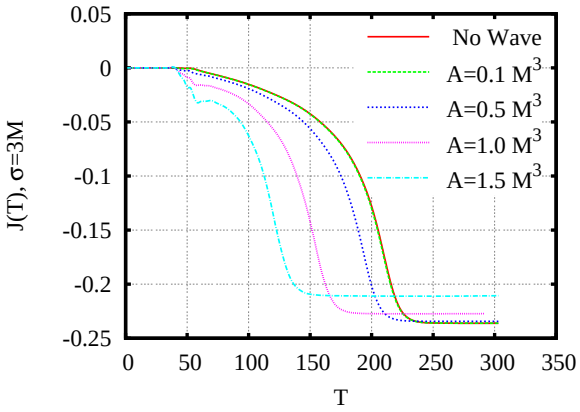

Figure 4.8. Angular momentum radiated across a sphere of radius $r = 40M$ for σ of $3M$ as calculated from the Weyl scalar Ψ_4.

Figs. 4.7 and 4.8 show some of the TNW propagating out at the same time as the spurious radiation is flushing out. One of the consequences of the wave traveling away from the center of the orbit is that it can interact with the black holes and potentially increase the mass of each black hole during the early part of the inspiral. Table 4.3 documents how the AH masses change as a function of A and σ for the stronger TNW cases. The black-hole mass is calculated using an AH tracker [176]. The $\Delta\mathcal{M}_{AH}$ is a measure of the change in the mass of each black hole up to $50M$, such that $\Delta\mathcal{M}_{AH} = \mathcal{M}_{AH}(t = 50M) - \mathcal{M}_{AH}(t = 0)$. The change in the initial ADM energy compared to the R1 run is given by $\Delta\mathcal{M} = \mathcal{E}_{\rm ADM} - \mathcal{E}_{\rm ADM,R1}$ at $t = 0$. We use this estimate of the differences in the mass of the spacetime between R1 and the rest of the runs to compute a naive estimate of the total fraction of energy absorbed by both black holes. Up to 7.89% of the extra ADM energy is observed to be absorbed by the black holes during the first $50M$ of the simulation, 3.9% by each black hole. The actual amount absorbed depends strongly on the width of the wave: the narrow, strong pulses are more readily absorbed than the weak, diffuse pulses that extend beyond the black holes in the initial data. In the weaker cases the change is barely visible above the noise in the AH mass calculation, in the stronger cases it is unmistakable.

To assess how important the absorption of energy by the black holes during the evolution is to the changes in merger time and radiated angular momentum, we refer to our discussion about the sensitivity of the merger time to a change in the initial AH masses in § 4.3.1. Given a change in mass of the individual black holes of 0.14%, the merger time changed by $6.7M$. In setting up the initial data, we do not allow the AH masses to change more than 0.04%. The amount of absorption measured during the evolution is as much as 3.9%; and, therefore, the increase in mass may be accounting for some, although not all, of the effects of the TNW. The outliers, the cases of most extreme merger times, merge so quickly that differentiating the burst of spurious radiation and region of pure inspiral is difficult. We also tried normalizing the time axis by

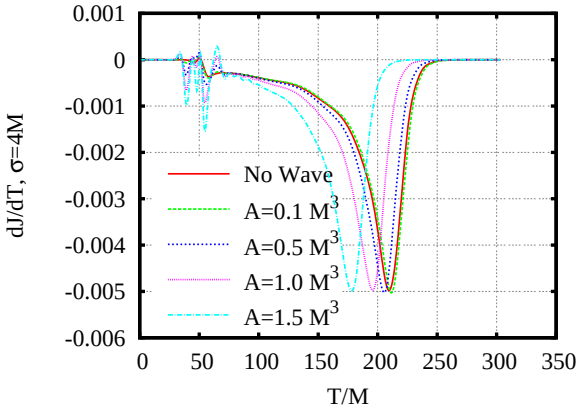

Figure 4.9. Flux of angular momentum across a sphere of radius $r = 40M$ for σ of $4M$ as calculated from the Weyl scalar Ψ_4.

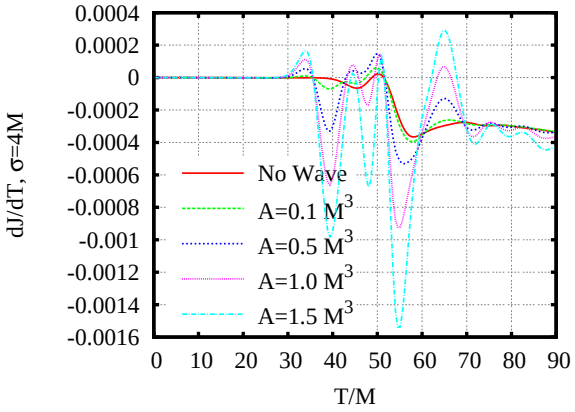

Figure 4.10. Closeup of angular momentum flux across a sphere of radius $r = 40M$ concentrating on what the spurious radiation carries.

the total AH masses after the wave has passed rather than that from the initial spacetime. This changed ΔT by no more than $1M$ so the choice of normalization does not account for the observed difference in merger times.

4.3.3 Final Spacetime

One of the important products of a BBH coalescence to relativists and astrophysicists are the final black hole's mass and spin. The final black-hole masses and spins are presented in the last two columns of Table 4.1. To compute the final mass, $M_{AH}^{(f)}$, we use energy conservation arguments by calculating the difference between the ADM energy and the radiated energy as calculated from the Weyl scalar Ψ_4. The final spin, $j_f = a_f/M_{AH}^{(f)}$, is calculated by finding the complex ringdown frequency in the $\ell = 2$, $m = 2$ mode and using the numerical Kerr frequencies given in Table II of Appendix D in Berti *et al.* [37] to find

Mass Analysis

A/M^3	σ/M	$\Delta\mathcal{M}_{AH}/M$	$\Delta\mathcal{M}/M$	$2\Delta\mathcal{M}_{AH}/(\Delta\mathcal{M})$	$\mathcal{M}_{AH}^{(f)}/(2\mathcal{M}_{AH}(t=50))$
0	-	0	0	0	0.950
0.5	3	3.90×10^{-4}	0.0106	7.34×10^{-2}	0.950
1.0	3	1.56×10^{-3}	0.0412	7.57×10^{-2}	0.951
1.5	3	3.49×10^{-3}	0.0886	7.89×10^{-2}	0.953
1.0	4	2.84×10^{-4}	0.0113	5.03×10^{-2}	0.950
1.5	4	6.41×10^{-4}	0.0251	5.11×10^{-2}	0.949
1.0	5	5.89×10^{-5}	0.0045	2.62×10^{-2}	0.950
1.5	5	1.26×10^{-4}	0.0092	2.74×10^{-2}	0.950
1.0	6	1.76×10^{-5}	0.0020	1.76×10^{-2}	0.950

Table 4.3. Change in AH mass compared to the difference in initial ADM energy for the stronger waves. $\Delta\mathcal{M}_{AH}$ is the change in a single black hole AH mass over the first $50M$, $\Delta\mathcal{M}$ is the additional ADM energy compared to the dry R1 run. Column 5 is the fraction of the extra ADM energy absorbed by both black holes combined, and the last column is the ratio of the final black hole mass to the total AH mass after the wave has been absorbed.

the corresponding spin parameter. This method agrees within stated errors to inverting the fit of Eq. (E2) of the same paper. Given the strong dependence of the spin on the damping time, we limit ourselves to the real part of the complex frequency and compare this to a separate spin calculation using the isolated horizon framework [71] where possible.

From the values of $\mathcal{M}_{AH}^{(f)}$ and j_f listed in Table 4.1, we can see that the final spins are constant within numerical accuracy and the final masses do not vary strongly with A and σ. The trend is an increase in the final mass with increasing $\mathcal{E}_{\rm ADM}$ becoming noticeably greater than our numerical errors for the four largest cases, $\mathcal{M}_{AH}^{(f)} \geq 0.963$. From this we can see that the narrower pulses not only have more energy, but they also interact more efficiently with the black holes. Being more readily absorbed by the punctures, they increase the individual masses and thus the final mass. The last column of Table 4.3 shows the ratio of the final mass to the total AH mass once the wave has interacted with the inspiraling black holes. We see the ratio is roughly constant, implying that approximately 5% of the initial AH mass is radiated away *if* we include the wave energy absorbed by the black holes. The exception is the most extreme wave where the black holes merged before all the spurious radiation has been absorbed into the AH. This would underestimate the AH growth and thus overestimate the value of the ratio. The change in final mass agrees within numerical error to the change in total AH mass after the wave has interacted with the inspiraling black holes except for the case of the strongest wave. In that case the AHs have not absorbed all the energy before the black holes begin to merge so we are underestimating the growth of these black holes.

4.3.4 Alignment of Amplitude and Phase

As stated in the introduction, a common method to compare waveforms is via a time-shift of the amplitude of each waveforms such that their peaks overlap, the result of which is shown in Fig. 4.11. We can see that

the waveforms overlap very well after the merger. The only noticeable difference is for the strongest TNW we evolved on the BBH system, the $A = 1.5M^3$, $\sigma = 3M$ case, where we find the largest difference in the final black hole compared to the dry R1 run. We can also see residual contamination of the merger portion of the waveform by the spurious radiation due to the binary merging so quickly. Similarly, we shift the waveform phase such that they overlap at $T = T_{\rm peak}$ in Fig. 4.12. The agreement in the phase's slope during ringdown is further confirmation that the mass and spin of the final black hole are not significantly altered.

The waveform overlap in the merger regime continues to start before the merger, as seen in [25], as long as the spurious radiation does not contaminate this region of the waveform. This alludes to the relatively simple form of the merger waveform seen in all the various situations currently tested. As long as the spurious radiation is not strong enough to noticeably alter the final black hole, the merger portion of the waveform remains essentially unaltered and the contamination to the system predominately results in the change in merger time and thus a time-shift of the waveform.

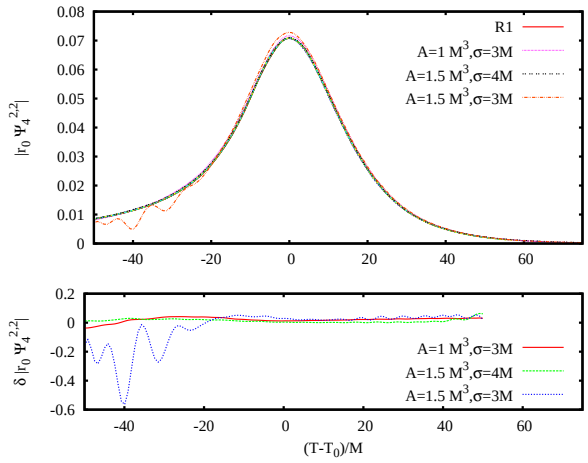

Figure 4.11. The top panel overlays the waveform amplitude $|r_0\Psi_4^{2,2}|$ for all runs shifted such that the peak amplitudes before ringdown coincide. This lets us compare the relative damping times of the ringdown and thus the properties of the final black hole. We also note the agreement for about $50M$ before ringdown as well. Though the legend only labels the distinguishable cases, all the runs are contained in the figure. In the bottom panel we show the fractional error for the three most extreme cases.

4.4 Conclusions

In this study, we simulated an equal-mass, non-spinning BBH system through its last orbits, merger and ringdown. The system is perturbed by the systematic addition of spurious radiation in the form of a Teukolsky-Nakamura gravitational wave at the binary's center of mass. The initial energy of the wave is tunable, specified by the amplitude and width of the radiation; in addition, the initial angular momentum was fixed for the entire sequence of runs. The binaries that contain the extra radiation invariably merge faster than

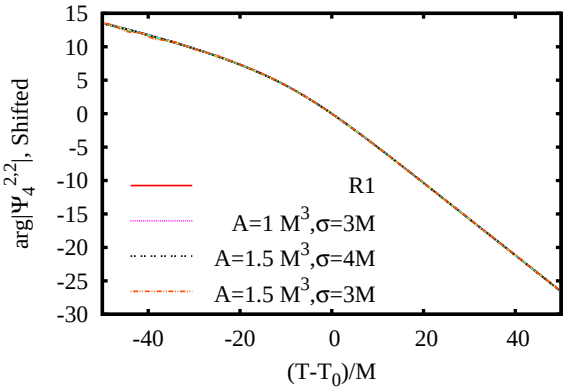

Figure 4.12. Comparison of arg($\Psi_4^{2,2}$) for all runs shifted such that the peak amplitudes before ringdown coincide and shifted vertically. This lets us compare the relative frequencies of ringdown. Though the legend only labels the distinguishable cases, all the runs are contained in the figure.

those with no additional radiation.

In addition to the main result of decreasing merger time, some changes to the radiated quantities and the final black hole were measurably above numerical error. This occurred once the additional energy provided by the TNW was equal to or greater than 1% of the dry BBH spacetime. As the TNW propagated out of the center, approximately 4% of additional ADM energy was absorbed by each black hole. In that strong-wave case, it was not possible to make an accurate measurement of the mass of the enlarged black holes before the plunge of the binary. The final spins of the black holes, however, remained unaffected by the gravitational radiation for all but the strongest case ($A = 1.5M^3$, $\sigma = 3M$). The constant black-hole spin is consistent with the wave slightly increasing the eccentricity of the orbit for small eccentricities [106, 170]. We also observed a decrease in the radiated angular momentum with increasing TNW strength.

We conjecture, based on the change in the initial binding energy of the BBH+TNW systems and Newtonian back-of-the-envelope calculation, that the spurious radiation increases the eccentricity of the original orbit. Unfortunately, the separation of the black holes was not large enough to enable a reliable calculation of the eccentricity. The merger time is very sensitive to the increase in individual black-hole masses via wave absorption; however, this was not enough to account for the observed change in the time of merger even when ignoring the strongest wave case. The combined effects of increasing the individual black-hole masses and the eccentricity of the orbit caused the binaries to merge faster with increasing energy.

One of the conjectures in the literature is that the spurious radiation, intrinsic to the construction of initial data for BBH evolutions, is flushed out of the simulation within a crossing-time and does not effect the radiation or the binary. We can relate the results of this study to other BBH evolutions by looking at the early changes in AH mass as well as how much energy leaves the system in the burst of spurious radiation. For the dry R1 run, the energy radiated in the initial pulse is $9\times10^{-4}\mathcal{E}_{\rm ADM,R1}$. We find that there is negligible

effect on the merger time at that level. Our results indicate that the spurious radiation present in initial data sets is unlikely to cause dramatic departures from the true BBH solution and therefore we can state that the simulated merger is robust to the presence of spurious radiation.

Chapter 5

The Effects of Approximate Initial Data on Binary Black Hole Mergers

> "Far better an approximate answer to the right question, than the exact answer to the wrong question, which can always be made precise." – *John Tukey*

With the developments of the past few years, numerical relativity simulations of BBH systems from inspiral to merger are now feasible, almost routine. Most importantly, they are quickly becoming a potent tool to study highly relevant astrophysical phenomena. Approximations such as those provided by PN theory have also proven to be valuable tools. They have the appeal of avoiding the computational complexities associated with finding exact solutions to the Einstein field equations. As the demand for more efficient simulations increases, it is desirable to consider approximate methodologies in conjunction with numerical relativity approaches. A natural "marriage" in this regard, which is the focus of this work, is to consider full Einstein evolutions of approximately constraint-satisfying initial data.

In general relativity, constructing initial data requires solving the Einstein constraints, a coupled set of elliptic equations (see Chapter 2 for a review on the mathematical foundations of numerical relativity and Sec. 3.1 for constructing initial data). Thus, in general obtaining solutions to the Einstein constraints necessitates solving elliptic equations, which is a complex numerical problem. When BH excision is used, the solvers are non-trivial [175, 152, 151] because of the excision boundaries. Even without excision, developing constraint solvers is demanding [13] and often requires introducing simplifying assumptions such as spatial conformal flatness.

Flexibility is also a very important issue. The family of problems addressed by numerical relativity is quickly expanding, involving non-traditional BH systems beyond the two-body problem [57, 127]. Without modifications to the standard initial data methodology, there will be limitations on the class of problems one is able to consider.

The focus of the study in this chapter is on the full Einstein numerical evolution of constraint-violating or approximate initial data. Evolutions of constraint-violating BBH initial data have been considered in the past. They were mostly done in the context of superposed Kerr-Schild BHs [171, 45, 130, 135], but there was also the study on the superposed "puncture Kerr" of Hannam *et al.* [99] as well as several studies evolving approximate post-Newtonian initial data [180, 115, 143]. More recently, constraint-violating initial data for punctures has been used for multiple BH evolutions [57, 127].

The difference with previous studies lies in the building blocks used to construct the data. In Refs. [67, 57, 127], the initial data sets were built from perturbative solutions of single punctures (boosted and/or spinning). Our approach, on the other hand, follows closely the *skeleton* solutions of the Einstein equations introduced by [78]. These solutions are derived from the full ADM Hamiltonian with the BHs represented by point-like sources modeled by Dirac delta function distributions. We consider configurations of non-spinning, equal-mass BBHs in quasi-circular orbits and investigate how well the evolution of these initial data is able to reproduce the corresponding results of constraint-satisfying initial data. We assess the effectiveness of the skeleton initial data by computing the matches with waveforms from constraint-satisfying initial data evolutions. We find that the differences in the evolutions, and thus waveforms, are due to negative Hamiltonian constraint violations present in the skeleton initial data. We observe that, during the course of the evolution, the skeleton data develops both Hamiltonian and momentum constraint violations which both propagate away and decay over time while the binary system relaxes to a constraint-satisfying solution with BHs of smaller mass and thus different dynamics.

In Sec. 5.1, we derive the procedure for constructing skeleton puncture initial data. In Sec. 5.2, we focus on quasi-circular configurations of equal-mass, non-spinning BBHs, and, using the effective potential method [63], we compare binding energies between skeleton and corresponding constraint-satisfying initial data. In Sec. 5.3, we investigate the structure of the Hamiltonian constraint violations in the skeleton data. In Sec. 5.4, we present results of the evolutions. Sec. 5.5 presents an analysis of the nature of the constraint violations with a model involving a single puncture. In Sec. 5.6, we discuss the impact of using waveforms from skeleton evolutions on data analysis. Conclusions are given in Sec. 5.7. The numerical simulations and results were obtained with the `MayaKranc` infrastructure as described in Sec. 2.2.

5.1 Skeleton Initial Data

The traditional approach to constructing initial data in numerical relativity involves specifying the pair $\{\gamma_{ij},\ K_{ij}\}$, where γ_{ij} is the intrinsic 3-metric to a t = constant hypersurface Σ_t, and K_{ij} denotes its extrinsiccurvature. We use the index convention that Latin indices in the first part of the alphabet denote 4-dimensional spacetime indices and those from the middle denote 3-dimensional spatial indices. The pair $\{\gamma_{ij},\ K_{ij}\}$ must satisfy the Einstein constraint equations:

$$\mathcal{R} + K^2 - K_{ij}K^{ij} \quad = \quad 16\,\pi\,\rho \tag{5.1}$$

$$\breve{\nabla}_j K^{ij} - \breve{\nabla}^i K \;=\; 8\pi S^i \,. \tag{5.2}$$

Equations (5.1) and (5.2) are respectively known as the Hamiltonian and momentum constraints. The operator $\breve{\nabla}_i$ denotes covariant differentiation with respect to γ_{ij} and $\mathcal{R}_{ij}$ its associated Ricci tensor. We follow the notation $K \equiv \gamma^{ij}K_{ij}$ and $\mathcal{R} \equiv \gamma^{ij}\mathcal{R}_{ij}$.

Although we are interested in vacuum spacetimes of BH systems, we have kept the matter sources ρ (total energy density) and S^i (momentum density). This is so we are able, as in Ref. [78], to represent the BHs as point-like sources modeled with Dirac delta distributions.

The constraints Eqs. (5.1) and (5.2) yield four equations; there are, thus, eight freely specifiable pieces in the data $\{\gamma_{ij},\, K_{ij}\}$. These free data can be used to single out the physical system under consideration (e.g., orbiting binary BHs) as well as to simplify solving the Einstein constraints. An elegant approach to identify the four pieces in $\{\gamma_{ij},\, K_{ij}\}$ that are fixed from solutions to the constraints was given in [192], based on work by [123] and others. The method is based on the following conformal transformations and tensorial decompositions:

$$\gamma_{ij} \;=\; \psi^4\,\tilde{\gamma}_{ij} \tag{5.3}$$

$$K_{ij} \;=\; A_{ij} + \frac{1}{3}\,\gamma_{ij}\,K \tag{5.4}$$

$$A^{ij} \;=\; \psi^{-10}\tilde{A}^{ij} \tag{5.5}$$

$$K \;=\; \tilde{K} \tag{5.6}$$

$$\tilde{A}^{ij} \;=\; \tilde{\mathcal{A}}^{ij} + (\tilde{\mathbb{L}}\mathcal{W})^{ij}\,, \tag{5.7}$$

where $A^i{}_i = \tilde{A}^i{}_i = 0$ and $\tilde{\nabla}_i\tilde{\mathcal{A}}^{ij} = 0$ with $\tilde{\nabla}_i$ covariant differentiation with respect to the conformal metric $\tilde{\gamma}_{ij}$. In the tensorial decomposition of $\tilde{A}^{ij}$ given by Eq. (5.7), $\tilde{\mathcal{A}}^{ij}$ gives the transverse part of $\tilde{A}^{ij}$, with the longitudinal part given by

$$(\tilde{\mathbb{L}}\mathcal{W})_{ij} \equiv 2\,\tilde{\nabla}_{(i}\,\mathcal{W}_{j)} - \frac{2}{3}\,\tilde{\gamma}_{ij}\,\tilde{\nabla}_k\,\mathcal{W}^k\,. \tag{5.8}$$

With the transformations Eqs. (5.3-5.7), the constraint Eqs. (5.1) and (5.2) become:

$$8\,\Delta\psi - \psi\,\tilde{\mathcal{R}} - \frac{2}{3}\psi^5 K^2 + \psi^{-7}\tilde{A}_{ij}\tilde{A}^{ij} \;=\; -16\,\pi\psi^5\rho \tag{5.9}$$

$$(\Delta_L\mathcal{W})^i - \frac{2}{3}\,\psi^{-6}\,\tilde{\nabla}^i K \;=\; 8\,\pi\psi^{10}S^i\,, \tag{5.10}$$

with $\tilde{\mathcal{R}}$ the Ricci scalar associated with the conformal 3-metric $\tilde{\gamma}_{ij}$ and $(\Delta_L\mathcal{W})^i \equiv \tilde{\nabla}_j(\tilde{\mathbb{L}}\mathcal{W})^{ij}$.

At this point, we introduce the assumptions of conformal flatness $\tilde{\gamma}_{ij} = \eta_{ij}$ and vanishing of both K and $\tilde{\mathcal{A}}^{ij}$. These assumptions exhaust the eight freely specifiable conditions at our disposal on $\{\gamma_{ij},\, K_{ij}\}$; five are

in $\tilde{\gamma}_{ij}$, one in K and two in $\tilde{\mathcal{A}}^{ij}$. The constraints then take the form:

$$\Delta\psi + \frac{1}{8}\,\psi^{-7}(\tilde{\mathbb{L}}\mathcal{W})^2 = -2\,\pi\psi^5\rho \tag{5.11}$$

$$(\Delta_L\mathcal{W})^i = 8\,\pi\psi^{10}S^i\,, \tag{5.12}$$

where $(\tilde{\mathbb{L}}\mathcal{W})^2 \equiv (\tilde{\mathbb{L}}\mathcal{W})^{ij}(\tilde{\mathbb{L}}\mathcal{W})_{ij}$. In the absence of matter sources, or if one sets $\tilde{S}^i = \psi^{10}S^i$, the constraints Eqs. (5.11) and (5.12) decouple. That is, one can solve first Eq. (5.12) for $\mathcal{W}^i$ and use this solution to solve Eq. (5.11) for ψ.

Following Ref. [78] albeit with considerable differences in notation, with the help of the momentum constraint Eq. (5.12), we notice that

$$\begin{aligned}(\tilde{\mathbb{L}}\mathcal{W})^2 &= 2\,(\tilde{\mathbb{L}}\mathcal{W})^{ij}\tilde{\nabla}_i\mathcal{W}_j \\ &= 2\,\tilde{\nabla}_i[(\tilde{\mathbb{L}}\mathcal{W})^{ij}\mathcal{W}_j] - 2\,\mathcal{W}_j\tilde{\nabla}_i(\tilde{\mathbb{L}}\mathcal{W})^{ij} \\ &= 2\,\tilde{\nabla}_i[(\tilde{\mathbb{L}}\mathcal{W})^{ij}\mathcal{W}_j] - 16\,\pi\,\psi^{10}\mathcal{W}_jS^j\,.\end{aligned} \tag{5.13}$$

Substitution of Eq. (5.13) into the Hamiltonian constraint Eq. (5.11) yields

$$\Delta\psi + \frac{1}{4}\,\psi^{-7}\tilde{\nabla}_i[(\tilde{\mathbb{L}}\mathcal{W})^{ij}\mathcal{W}_j] = -2\,\pi[\psi^5\rho - \psi^3\mathcal{W}_iS^i]\,. \tag{5.14}$$

We address now the matter sources. The stress-energy tensor for a set of non-interacting point-like particles with rest mass $\mathcal{M}_A$, 4-velocity U^a_A, and comoving number density $\mathcal{N}_A$ is given by

$$T^{ab} = \sum_A \mathcal{M}_A\,\mathcal{N}_A\,U^a_A\,U^b_A\,, \tag{5.15}$$

where the sum is understood to run over all the particles. For each particle A located at x^i_A, the comoving number density is given by a δ-function as

$$\begin{aligned}\mathcal{N}_A &= \int \frac{1}{\sqrt{-g}}\delta^4[x^a - x^a_A(\tau)]d\tau \\ &= \frac{1}{\alpha\,U^t_A\,\sqrt{\gamma}}\delta^3[x^i - x^i_A(t)] \\ &= \frac{\delta_A}{\mathrm{W}_A\,\sqrt{\gamma}}\,,\end{aligned} \tag{5.16}$$

with g the determinant of 4-dimensional spacetime metric, $\delta_A \equiv \delta^3(x^i - x^i_A)$, α the lapse function, $\mathrm{W}_A = \alpha\,U^t_A = -n_aU^a_A$, and n^a the future-directed unit normal to the hypersurface Σ_t. The stress-energy tensor can then be rewritten as

$$T^{ab} = \sum_A \frac{\mathcal{M}_A\,\delta_A}{\mathrm{W}_A\,\sqrt{\gamma}}\,U^a_A\,U^b_A\,. \tag{5.17}$$

Given Eq. (5.17), the matter sources take the form:

$$\begin{aligned}\rho &= n_a\, n_b\, T^{ab} \\ &= \sum_A \frac{\mathcal{M}_A\, \mathrm{W}_A\, \delta_A}{\psi^6\, \sqrt{\eta}}\,,\end{aligned} \tag{5.18}$$

and

$$\begin{aligned}S^a &= -\perp^a_b\ n_c\, T^{bc} \\ &= \sum_A \frac{\mathcal{M}_A\ \perp^a_b\ U^b_A\, \delta_A}{\psi^6\, \sqrt{\eta}} \\ &= \sum_A \frac{\mathcal{P}^a_A\, \delta_A}{\psi^{10}\, \sqrt{\eta}}\,,\end{aligned} \tag{5.19}$$

where we have used $\sqrt{\gamma} = \psi^6\, \sqrt{\eta}$, $\gamma_{ab} = g_{ab} + n_a\, n_b$ and $\perp^a_b = g^{ac} g_{cb}$. In deriving Eq. (5.19), we have also introduced the spatial momentum vector $\mathcal{P}^a_A \equiv \mathcal{M}_A\, \psi^4\ \perp^a_b\ U^b_A$. The vector $\mathcal{P}^a$ is related to the spatial part of the 4-momentum $p^a = \mathcal{M} U^a$ of the point-like particles by $\mathcal{P}^a = \psi^4\ \perp^a_b\ p^b$. Substitution of the source Eqs. (5.18) and (5.19) into Eqs. (5.12) and (5.14) yields

$$\Delta\psi + \frac{1}{4\,\psi^7}\tilde{\nabla}_i[(\tilde{\mathbb{L}}\mathcal{W})^{ij}\mathcal{W}_j] = -2\,\pi \sum_A \frac{m_A\, \delta_A}{\sqrt{\eta}} \tag{5.20}$$

$$(\Delta_L \mathcal{W})^i = 8\,\pi \sum_A \frac{\mathcal{P}^i_A\, \delta_A}{\sqrt{\eta}}\,, \tag{5.21}$$

where

$$m_A = \frac{\mathcal{M}_A\, \mathrm{W}_A}{\psi} - \frac{\mathcal{W}_i \mathcal{P}^i_A}{\psi^7}\,. \tag{5.22}$$

Bowen and York [42] found a solution to the momentum constraint as given by Eq. (5.21). The solution represent BHs with linear momentum $\mathcal{P}^i_A$ and is explicitly given as

$$\mathcal{W}^i = -\sum_A \frac{1}{4\,r}(7\,\mathcal{P}^i + \mathfrak{n}^i\, \mathfrak{n}_j\, \mathcal{P}^j)\Big|_A \tag{5.23}$$

with $\mathfrak{n}^i$ the unit normal of constant r spheres in flat space. In terms of Eq. (5.23), $(\tilde{\mathbb{L}}\mathcal{W})^{ij}$ takes the form:

$$(\tilde{\mathbb{L}}\mathcal{W})^{ij} = \sum_A \frac{3}{2\,r^2}\left[2\,\mathcal{P}^{(i}\,\mathfrak{n}^{j)} - (\eta^{ij} - \mathfrak{n}^i\,\mathfrak{n}^j)\,\mathfrak{n}_k\,\mathcal{P}^k\right]_A \tag{5.24}$$

In Eqs. (5.23) and (5.24), $r_A = \|x^i - \Xi^i_A\|$, $\mathfrak{n}^i_A = (x^i - \Xi^i_A)/r_A$ with Ξ^i_A the coordinate location of BH_A. It can be shown that the total ADM linear momentum is $\mathcal{P}^i = \sum_A \mathcal{P}^i_A$.

We now turn our attention to the Hamiltonian constraint Eq. (5.20). As pointed out in Ref. [78], the term

$\psi^7\tilde{\nabla}_i[(\tilde{\mathbb{L}}\mathcal{W})^{ij}\mathcal{W}_j]$ in Eq. (5.20) is a "flesh" term that provides the field between the particles and has the following contribution to the Hamiltonian:

$$\int \frac{1}{\psi^7}\tilde{\nabla}_i[(\tilde{\mathbb{L}}\mathcal{W})^{ij}\mathcal{W}_j]d^3x = -7\int \frac{1}{\psi^8}(\tilde{\mathbb{L}}\mathcal{W})^{ij}\mathcal{W}_j\tilde{\nabla}_i\psi\, d^3x\,.$$

The only approximation that goes into defining the skeleton initial data is to neglect the contribution from this term. With this approximation, the Hamiltonian constraint Eq. (5.20) reads:

$$\Delta\psi = -2\,\pi\sum_A \frac{m_A\,\delta_A}{\sqrt{\eta}} \tag{5.25}$$

with m_A given by Eq. (5.22). Notice that m_A is singular at $x^i = \Xi^i_A$ because ψ and $\mathcal{W}^i$ are singular at Ξ^i_A. Following Ref. [78], we solve Eq. (5.25) by means of Hadamard's "partie finie" procedure [113]; that is,

$$\begin{aligned}
\psi &= 1 - 4\,\pi\Delta^{-1}\left(\sum_A \frac{m_A(x^i)\,\delta_A}{2\,\sqrt{\eta}}\right)\\
&= 1 - 4\,\pi\Delta^{-1}\left(\sum_A \frac{m^{(\rm reg)}_A(\Xi^i_A)\,\delta_A}{2\,\sqrt{\eta}}\right)\\
&= 1 - 4\,\pi\sum_A \frac{m^{(\rm reg)}_A(\Xi^i_A)}{2}\,\Delta^{-1}\frac{\delta_A}{\sqrt{\eta}}\\
&= 1 + \sum_A \frac{m^{(\rm reg)}_A}{2\,r_A}\,,
\end{aligned} \tag{5.26}$$

where

$$m^{(\rm reg)}_A \equiv \frac{\mathcal{M}_A\,\mathrm{W}_A}{\Phi_A} - \frac{\mathcal{W}^A_i\mathcal{P}^i_A}{\Phi^7_A} \tag{5.27}$$

$$\Phi_A = 1 + \sum_{B\neq A}\frac{m^{(\rm reg)}_B}{2r_{AB}} \tag{5.28}$$

$$\mathrm{W}_A = \left[1 + \frac{\mathcal{P}^i\mathcal{P}_i}{\mathcal{M}^2\,\Phi^4}\right]^{1/2}_A \tag{5.29}$$

$$\mathcal{W}^A_i\mathcal{P}^i_A = \sum_{B\neq A}\left(\frac{-1}{4\,r_{AB}}\right)[7\,\mathcal{P}^i_B\mathcal{P}^A_i - (\mathfrak{n}^{AB}_i\mathcal{P}^i_A)(\mathfrak{n}^{AB}_i\mathcal{P}^i_B)]\,, \tag{5.30}$$

with $r_{AB} = \|\Xi^i_A - \Xi^i_B\|$ and $\mathfrak{n}^i_{AB} = (\Xi^i_A - \Xi^i_B)/r_{AB}$. The parameter $m^{(\rm reg)}_A$ is commonly known as the *bare* mass of the BH. On the other hand, $\mathcal{M}$ is known as the *irreducible* mass of the BH. Φ_A is the regularized value of $\psi(\Xi^i_A)$. In summary, the skeleton initial data $\{\gamma_{ij},\, K_{ij}\}$ is then given by $\gamma_{ij} = \psi^4\eta_{ij}$ and $K_{ij} = \psi^{-2}(\tilde{\mathbb{L}}\mathcal{W})_{ij}$ with ψ given by Eq. (5.26) and $(\tilde{\mathbb{L}}\mathcal{W})^{ij}$ given by Eq. (5.24).

For comparison, the exact or constraint-satisfying puncture initial data method [44] consists also of $\gamma_{ij} = \psi^4 \eta_{ij}$ and $K_{ij} = \psi^{-2}(\tilde{\mathbb{L}}\mathcal{W})_{ij}$ with $(\tilde{\mathbb{L}}\mathcal{W})^{ij}$ given by Eq. (5.24), but in this case

$$\psi = 1 + \sum_A \frac{\mathrm{m}_A}{2\,r_A} + u\,, \tag{5.31}$$

with u a regular solution to

$$\Delta u + \frac{1}{8\,\psi^7}(\tilde{\mathbb{L}}\mathcal{W})^2 = 0 \tag{5.32}$$

and m_A is another mass parameter similarly called the *bare* mass.

5.2 Quasi-circular Initial Data

We restrict our attention to initial data configurations representing two equal mass ($\mathcal{M}_1 = \mathcal{M}_2 \equiv \mathcal{M}$, $m_1^{(\mathrm{reg})} = m_2^{(\mathrm{reg})} \equiv m$), non-spinning BHs in quasi-circular orbits. That is $\mathcal{P}^i_1 = -\mathcal{P}^i_2 \equiv \mathcal{P}^i$, $r_{12} = \|\Xi^i_1 - \Xi^i_2\| \equiv d$, and $\mathfrak{n}^{12}_i \mathcal{P}^i = 0$. Under these assumptions:

$$\psi = 1 + \frac{m}{2\,r_1} + \frac{m}{2\,r_2} \tag{5.33}$$

where

$$m = \frac{\mathcal{M}\mathrm{W}}{\Phi} - \frac{7}{4}\frac{\mathcal{P}^2}{d\,\Phi^7} \tag{5.34}$$

$$\Phi = 1 + \frac{m}{2\,d} \tag{5.35}$$

$$\mathrm{W} = \left[1 + \frac{\mathcal{P}^2}{\mathcal{M}^2\Phi^4}\right]^{1/2}. \tag{5.36}$$

While deriving Eq. (5.34), we used that for circular orbits $\mathcal{W}_i\mathcal{P}^i = 7\,\mathcal{P}^2/(4\,d)$ with $\mathcal{P}^2 = \mathcal{P}^i\mathcal{P}_i = \mathcal{P}^i\mathcal{P}^j\eta_{ij}$ as can be seen from Eq. (5.30).

We focus now on the differences between the constraint-satisfying and skeleton initial data for quasi-circular sequences using the effective potential method [63]. The general idea of this method is to find configurations that satisfy the condition:

$$\left.\frac{\partial E_b}{\partial L}\right|_{M,\mathcal{J}_{\mathrm{ADM}}} = 0\,, \tag{5.37}$$

with $E_b = \mathcal{E}_{\mathrm{ADM}} - \mathcal{M}$ the binding energy of the system. The distance L is a measure of the proper separation between the BHs (e.g., horizon to horizon), and $M = 2\,\mathcal{M}$ is the sum of the irreducible masses. The quantities $\mathcal{E}_{\mathrm{ADM}}$ and $\mathcal{J}_{\mathrm{ADM}}$ are respectively the total ADM mass and angular momentum of the system (see

Run	d/M	$\mathcal{P}/M$	m/M	$\mathcal{M}/M$	$\mathcal{E}_{\rm ADM}/M$	$\mathcal{J}_{\rm ADM}/M^2$
QC0e	2.337	0.33320	0.45300	0.519071	1.0195	0.7787
QC0a	2.337	0.33320	0.48950	0.519071	0.9790	0.7787
R1e	6.514	0.13300	0.48300	0.505085	0.9957	0.8664
R1a	6.514	0.13300	0.49717	0.505085	0.9943	0.8664
D10e	10.00	0.09543	0.48595	0.500000	0.9895	0.9530
D10a	10.00	0.09543	0.49458	0.500000	0.9891	0.9530

Table 5.1. *Initial data parameters:* The punctures have bare masses m, linear momenta $\pm\mathcal{P}$ aligned with the y-axis and are separated by a distance d along the x-axis. The irreducible mass of each BH from $m^{(\rm reg)}$ is $\mathcal{M}$. The ADM masses and angular momenta of the spacetimes are given respectively by $\mathcal{E}_{\rm ADM}$ and $\mathcal{J}_{\rm ADM}$.

Sec. 3.2), which can be computed from:

$$\mathcal{E}_{\rm ADM} = -\frac{1}{2\pi}\oint_\infty \tilde{\nabla}_i\psi\, d^2S^i \tag{5.38}$$

$$\mathcal{J}_{{\rm ADM}\,i} = \frac{\epsilon_{ijk}}{8\pi}\oint_\infty x^j K^{kl}\, d^2S_l\,. \tag{5.39}$$

It is not too difficult to show from Eq. (5.39) that, given $K_{ij} = \psi^{-2}(\tilde{\mathbb{L}}\mathcal{W})_{ij}$, the ADM angular momentum for binaries initially in quasi-circular orbits is $\mathcal{J}_{\rm ADM} = d\,\mathcal{P}$. On the other hand, with ψ given by Eq. (5.33) the total ADM mass from Eq. (5.38) is given by the sum of the bare masses of the BHs, namely $\mathcal{E}_{\rm ADM} = 2\,m$; thus, the binding energy becomes $E_b = 2\,m - 2\,\mathcal{M}$. The bare masses for the skeleton initial data are obtained by solving the implicit Eq. (5.34) using a Newton-Raphson method.

Figure 5.1 (top panel) shows the comparison of the binding energy E_b as a function of the total ADM angular momentum $\mathcal{J}_{\rm ADM}$ between the constraint-satisfying initial data from [179] (squares) and the skeleton initial data in this work (triangles). The lower panel in Fig. 5.1 shows the corresponding % relative difference between both results. Not surprisingly, as the binary separation increases (i.e. larger angular momentum), the differences diminish. For reference, the vertical lines denote the angular momentum for typical data sets considered in the literature: QC0 in Ref. [55], R1 in Ref. [26] and D10 in Ref. [179]. The differences in binding energy between the skeleton and the constraint-satisfying initial data are $\sim 20\,\%$ for QC0, $\sim 6\,\%$ for R1 and $\sim 2\,\%$ for D10.

Table 5.1 provides the parameters of the initial configurations for both the skeleton and constraint-satisfying data sets. The cases of exact or constraint-satisfying initial data are labeled with the letter "e" and the corresponding skeleton or approximate case with the letter "a".

As mentioned before, the only fundamental difference between the two initial data sets is in the conformal factor ψ. For the constraint-satisfying data set ψ is computed from Eq. (5.31) by solving the Hamiltonian constraint in the form given by Eq. (5.32) and for the skeleton the conformal factor ψ is constructed using Eq. (5.26). In Fig. 5.2, we show the relative difference $\delta\psi/\psi = (\psi_{\rm a} - \psi_{\rm e})/\psi_{\rm e}$ from the two data along the axis joining the punctures (x-axis) for the D10, R1 and QC0 cases. Notice the large differences in the imme-

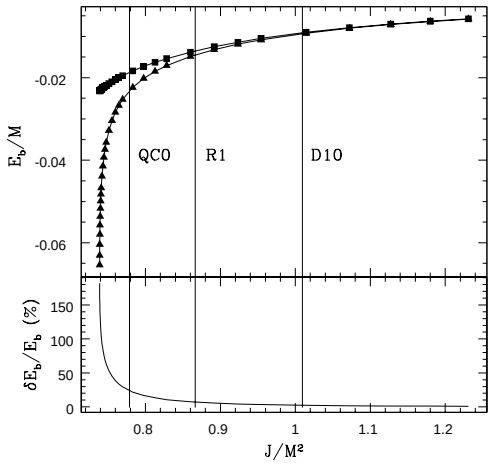

Figure 5.1. Comparison of the binding energy E_b as a function of the total ADM angular momentum $\mathcal{J}_{\rm ADM}$ between the initial data from [179] (squares) and the skeleton initial data (triangles)

diate vicinity of the punctures. In the next section, we will investigate how these differences translate into constraint violations.

5.3 Hamiltonian Constraint Violations

For the remainder of the chapter we will concentrate our attention on the D10 case: a situation in which the BHs are not too close to the merger and with an initial separation that permits a reasonable overlap with the post-Newtonian regime [28, 100]. It is important to point out that the numerical data D10e, although called exact, also violate the constraints initially. The violations in the exact initial data, however, are a consequence of numerical errors which can be made arbitrarily small in the limit to the continuum. On the other hand, the constraint violations in the skeleton data are strongly dominated by resolution-independent effects, converging at fourth order to some non-zero initial constraint violations.

In order to understand the nature of the constraint violations in the skeleton initial data and in particular their dynamics in the course of the evolution, we take the point of view that the violations introduce "spurious" sources ρ and S^i in Eq. (5.1) and (5.2), respectively. Notice that initially we do not have a "spurious" momentum density S^i because the skeleton initial data by construction are an exact solution to the momentum constraint. It is important to keep in mind that one should not assign physical properties to ρ and S^i. They are only used to quantify constraint violations. In particular, the violations ρ are not restricted to satisfy energy conditions and thus are free to take negative values.

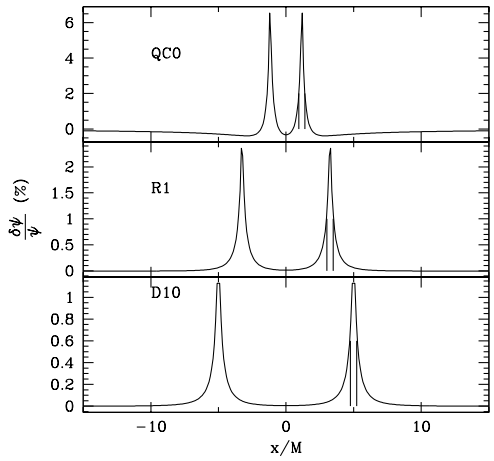

Figure 5.2. The relative difference in the conformal factor ψ between the skeleton initial data and the corresponding constraint-satisfying data along the x-axis joining the punctures for the three cases labeled in Fig. 5.1. The solid vertical lines represent the location of the AHs.

Fig. 5.3 shows a surface plot of ρ for the BBH skeleton initial data in the neighborhood of one of the punctures. Notice that the puncture seems to be embedded in a "cloud" or a pocket of negative ρ. Furthermore, the cloud is more negative in the direction aligned with the linear momentum of the puncture (in this case the y-axis). This effect is more evident from Fig. 5.4 where we plot ρ in the top panel along the x-axis (the direction joining the BHs) and in the bottom panel along the y-axis. The glitches at the bottom of the bottom of the constraint violation pockets are due to refinement boundaries.

5.4 Skeleton Evolutions

Given the initial data, we turn our attention now to evolutions. The evolution runs were done on a computational grid with 9 refinement levels, the finest 5 levels containing 24^3 gridpoints in radius and the remaining 4 with 48^3 gridpoints in radius. To check the dependence of the results with resolution, we considered grid spacings at the finest level of $M/38.4$, $M/44.8$ and $M/51.2$ and found the skeleton waveforms converge at the same order as the exact waveforms. The results presented here were done at the resolution of $M/51.2$.

Fig. 5.5 shows the trajectory of one of the BHs from the skeleton initial data (dashed line) as well as its constraint-satisfying counterpart (solid line). Both trajectories are very close to each other during the first quarter orbit. Beyond that point, the BH from the skeleton initial data follows an eccentric orbit. Finally, near merger or at the plunge, the trajectories once again lie very closely together.

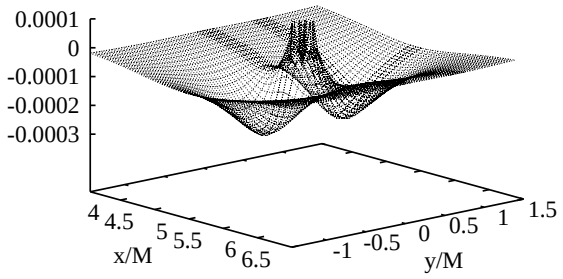

Figure 5.3. Surface plot of ρ, as derived from the Hamiltonian constraint violations, in the *xy*-plane surrounding one puncture for the skeleton initial data, D10a.

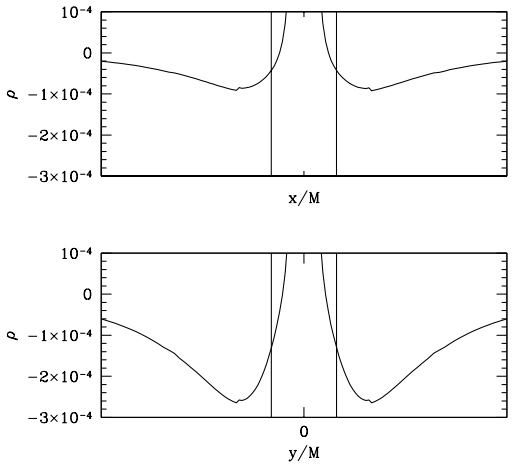

Figure 5.4. Sources ρ corresponding to Fig. 5.3 along the *x*-axis joining the BHs (top panel) and along the *y*-axis (bottom panel), the linear momentum direction. The solid vertical lines mark the mean coordinate radius of the AH.

In Fig. 5.6, we compare the waveforms of the skeleton initial data with its constraint-satisfying counterpart as detected at 50 M. The presence of a phase shift between the two waveforms is evident. The constraint-satisfying initial data evolution reaches the merger approximately 10 M before the skeleton initial data evolution. This difference remains within 1 M of this between different resolutions. Another difference in the two evolutions is in the inspiral. As mentioned before, the skeleton data yields a larger eccentricity in the inspiral. This can be clearly observed from Fig. 5.7 where the same comparison as in Fig. 5.6 is shown

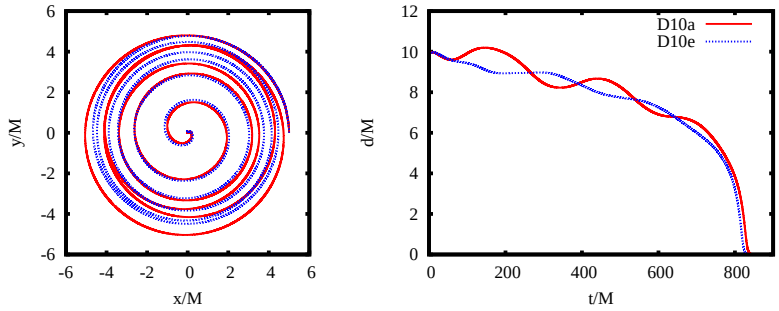

Figure 5.5. The left plot shows the trajectory of one of the BHs from the skeleton initial data (red line) as well as its constraint-satisfying counterpart (blue line). On the right we plot the coordinate separation between the BHs as a function of coordinate time.

but in terms of the amplitude (top panel) and phase (bottom panel). Here we have applied a time shift of $10\,M$ to align the point at which the waveforms reach their maximum values. The inspiral and plunge of the binary is before the "knee" in the phase or the maximum in the amplitude. On the other hand the quasi-normal ringing of the final BH takes place after the knee in the phase and the maximum in the amplitude. Notice that the phases are practically identical for both cases. Furthermore, both the post-knee phase and post-maximum amplitude are almost the same for skeleton and constraint-satisfying evolutions, which is an indication that the final BHs are almost identical [106]. On the other hand, the inspiral amplitudes in Fig. 5.7 clearly show differences in the level of eccentricity as seen by the oscillations in the amplitude.

From the waveforms, we have computed the energy $E_{\rm rad}$ and angular momentum $J_{\rm rad}$ radiated. For the constraint-satisfying initial data, we obtained $E_{\rm rad} = 0.0354\,M$ and $J_{\rm rad} = 0.3060\,M^2$ and for the skeleton data $E_{\rm rad} = 0.0359\,M$ and $J_{\rm rad} = 0.3063\,M^2$, which correspond to differences of 1.4% and 0.1% respectively. These differences are consistent with differences in amplitude of the ADM energy and angular momentum in the initial data ($< 10^{-4}$).

To better understand the change in trajectories and the corresponding phase shift reflected in the waveforms (see Fig. 5.6), we have tracked the evolution of the AH masses. The AH mass for one of the BHs is plotted in Fig. 5.8 where the error due to grid spacing resolution is of order $10^{-5}\,M$. While the AH mass for the constraint-satisfying evolution stays relatively constant (solid line), the AH mass for the skeleton evolution varies significantly (dashed line). In fact, the mass starts 1.4% higher than the constraint-satisfying value and monotonically decreases. Empirically, the AH masses decrease as $1/t$ at late times. By fitting a polynomial in $1/t$ to the AH evolution at late times, we find the mass asymptotes to $0.501 \pm 0.001M$, within 0.2% of the constraint-satisfying initial AH mass. However, the BHs merge before the skeleton AH mass could reach this asymptotic value. An interesting question currently under investigation is how the skeleton evolution's changing eccentricity compares to that of the Newtonian two-body problem with variable mass.

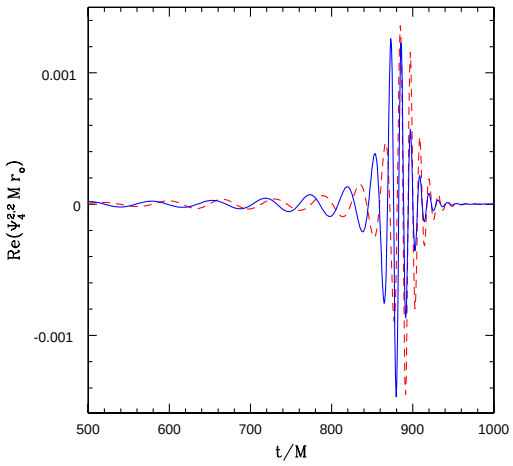

Figure 5.6. Real parts of the waveform, $r_o\Psi_4^{2,2}\,M$, extracted at $r_o = 50\,M$ for both the skeleton (red) and the constraint-satisfying (blue) initial data.

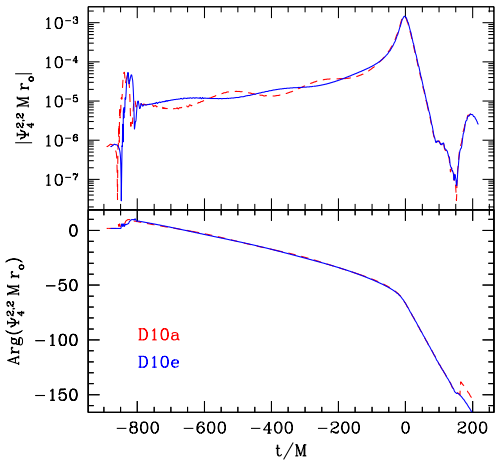

Figure 5.7. Amplitude (top panel) and phase (bottom panel) of the waveforms $r_o\Psi_4^{2,2}\,M$ in Fig. 5.6, skeleton data (red) and constraint-satisfying data (blue). The time axis has been shifted by 10 M to align the point at which the amplitudes reach their maximum values.

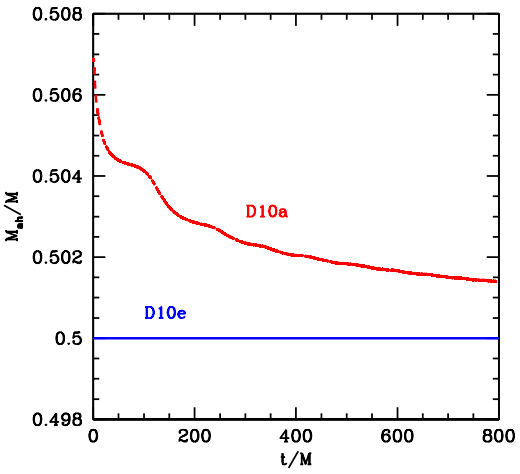

Figure 5.8. The evolution of the AH mass of one of the BHs shown for both the constraint-satisfying initial data D10e (blue) and its skeleton counterpart (red). Errors in AH due to grid spacing are of order $10^{-5}\,M$.

5.5 Single Puncture Analysis

As noted in Sec. 5.2, the Hamiltonian constraint violations are negative in the vicinity of the punctures. To better understand the evolutions of the skeleton initial data, we consider a test case where we evolve a single, non-spinning puncture and add by hand negative constraint violations surrounding it. That is, we solve the Hamiltonian constraint as if there were an additional matter field ρ present, namely

$$\Delta\psi = -2\,\pi\,\rho\,\psi^5\,. \tag{5.40}$$

For $\rho > 0$, the existence of a solution is not in general guaranteed as discussed in [192, 61]. For such ρ, one needs to re-scale the source according to the conformal rescaling $\hat{\rho} = \rho\,\psi^{-s}$, with $s > 5$. In our case, however, we are mostly interested in $\rho < 0$, which does not require any rescaling for existence of a solution.

Following the procedure for multiple BHs, see Eq. (5.31), we use the ansatz $\psi = \psi_o + u$, with $\psi_o = 1 + m/2r$ the solution to the homogeneous equation (i.e. the single puncture solution). We use ψ_o as the conformal factor for rescaling ρ and keep this constant while solving the constraint equation. With this ansatz, Eq. (5.40) becomes

$$\Delta u = -2\,\pi\,\hat{\rho}\,(\psi_o + u)^n \tag{5.41}$$

where n must be of opposite sign compared to ρ. We choose s such that $n = -3$ for $\rho > 0$, as is standard, and $n = 5$ for $\rho < 0$.

Model	F/M^2	$\mathcal{E}_{\rm ADM}/M$	$\mathcal{M}^i_{AH}/M$	$\mathcal{M}^f_{AH}/M$	E_ρ/M
F_1	0.001	1.0046	1.0012	1.0041	0.0034
F_2	-0.001	0.9902	0.9973	0.9911	-0.0071
F_3	-0.010	0.9102	0.9858	0.9183	-0.0756

Table 5.2. *Models:* Results of evolutions a single puncture in the presence of a Gaussian source ρ with $r_o = \sigma = 1\,M$ and amplitude F. The initial AH mass and ADM energy are $\mathcal{M}^i_{AH}$ and $\mathcal{E}_{\rm ADM}$ respectively. $\mathcal{M}^f_{AH}/M$ is the asymptotic final AH mass as extrapolated from the simulation, and $E_\rho = \mathcal{E}_{\rm ADM} - \mathcal{M}^i_{AH}$.

For simplicity, we choose

$$\rho = \psi_o^m F e^{-(r-r_o)^2/(2\sigma^2)} \tag{5.42}$$

where r_0 is the position with respect to the puncture, $m = 0$ for $\rho > 0$, and $m = -5$ for $\rho < 0$. The factor ψ_o^m is necessary for regularity of the solution u at the puncture. We also assume that the source ρ does not have initial momentum (i.e. $S^i = 0$); thus, the momentum constraint remains satisfied as in the vacuum case.

Table 5.2 lists the results from the evolutions for $r_o = \sigma = 1\,M$. The choice of centering the Gaussian at $r_o = 1\,M$ was aimed at favoring the amount of ρ accreted by the BH. The distribution, like the skeleton initial data, is thus peaked at twice the horizon coordinate radius. Unlike the dumbbell-like configuration of the skeleton initial data's constraint violations, the introduced constraint violations in these cases are spherically symmetric. Notice that case F_1 has a positive source (i.e. $F > 0$) yielding positive constraint violations while the other two have negative sources yielding negative Hamiltonian constraint violations. The effect of the source ρ is evident in the ADM mass ($\mathcal{E}_{\rm ADM}$) and initial AH mass ($\mathcal{M}^i_{AH}$). For the positive source, the masses are larger than the puncture mass in vacuum, $1\,M$, and smaller for the negative sources. Also in Table 5.2, we include $E_\rho = \mathcal{E}_{\rm ADM} - \mathcal{M}^i_{AH}$, which gives a measure of the extra energy content in the initial data due to ρ. The strength of F_3 was chosen such that the strength of the constraint violations and the change of the initial $\mathcal{M}_{AH}$ are comparable to those in the skeleton initial data. As the geometry of the constraint violations create a much larger change in the ADM energy, cases F_1 and F_2 have more modest constraint violations which yield more modest changes in ADM mass.

We evolved the models in Table 5.2 for $300\,M$. Fig. 5.9 shows how the AH mass evolves during the evolution. We have evolved the model F_3 at different resolutions and estimated the AH masses to have an approximate relative error of $\sim 0.009\%$. We observed that at late times the AH mass evolves as $\mathcal{M}^f_{AH} + C/t$. The values reported in Table 5.2 are those extrapolated to $t \to \infty$.

The evolutions of the single puncture models clearly demonstrate that depending on the signature of ρ, the mass of the BH, as measured from the AH, will increase or decrease. That is, over the course of the evolution, the AH masses evolve to approach the ADM energy, decreasing for a negative ρ and increasing for positive ρ. In other words, the source ρ initially hovering near a puncture will fall into the BH, increasing or decreasing its mass as the system becomes stationary depending on the sign of ρ. The extent to which the

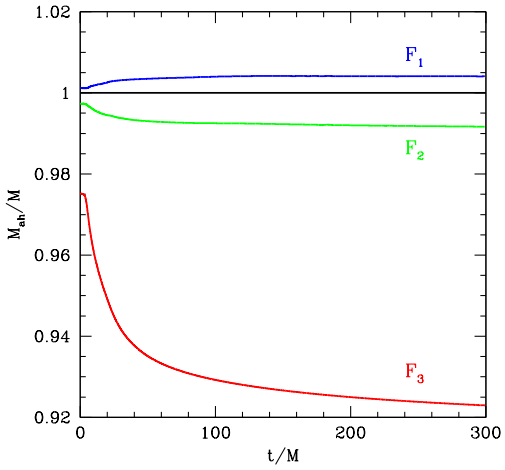

Figure 5.9. Evolution of the AH mass for the models described in Table 5.2. The error between resolutions for F_3 was of order 10^{-5} over the course of the evolution.

final mass of the BH approaches the total ADM energy depends on how much of the density ρ is "accreted" by the BH. Since in our case we do not impose the restriction of positivity on ρ, the BH is free to decrease its mass. Notice also that the final AH mass does not satisfy the condition $\mathcal{M}^f_{AH} = \mathcal{M}^i_{AH} + E_\rho$, which means that a fraction (< 1% in our cases) of E_ρ mass is radiated away.

Figure 5.10 shows the Hamiltonian constraint violation ρ near the beginning of the simulation at $t = 0.078\,M$ (top panel) and at the end, $t = 300\,M$, of the simulation (bottom panel). Solid lines represent the constraint-satisfying case and dashed lines the F_3 model. Fig. 5.11 shows the corresponding results for the momentum constraint violations S^i along the x-axis. By construction, initially there are only Hamiltonian constraint violations in the F_3 model. However, it is evident from the top panel in Fig. 5.11 that constraint violations in the momentum constraint develop also very early in the evolution. The growth of momentum constraint violations proceed up to a time $t \sim 3\,M$. The subsequent dynamics of the constraint violations consists of ingoing and outgoing waves. Because of the proximity to the puncture, the outgoing waves are a little bit weaker, with most of the constraint violations "accreted" by the BH. After approximately $t \sim 50\,M$ of evolution, the F_3 model relaxes to the configuration of the constraint-satisfying puncture and remains there as seen in the bottom panels in Figs. 5.10 and 5.11. The final constraint violations in the system arise from numerical errors.

An important aspect to point out is that although the constraint-violating cases relax to a constraint-satisfying solution, the solutions that they relax to are not necessarily the same solutions as a single puncture in a vacuum spacetime. The new solution satisfies the Einstein equations but for a single puncture spacetime

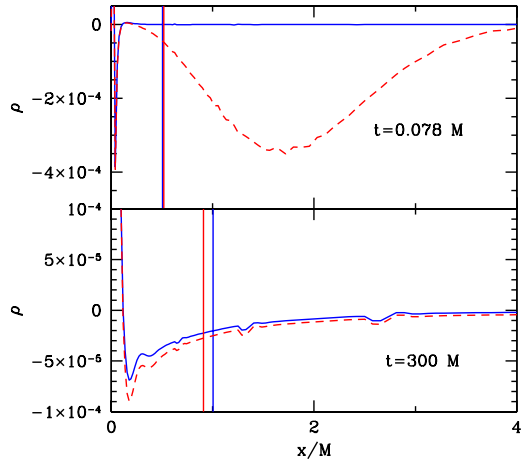

Figure 5.10. Hamiltonian constraint violation ρ near the beginning of the simulation at $t = 0.078\,M$ (top panel) and at the end, $t = 300\,M$, of the simulation (bottom panel). Solid blue lines represents the constraint-satisfying case and dashed red lines the F_3 model. The solid vertical lines are the mean coordinate radii of the skeleton (red) and constraint-satisfying (blue) AH at the given time. The constraint violations still present at late times are due to discretization around the punctures.

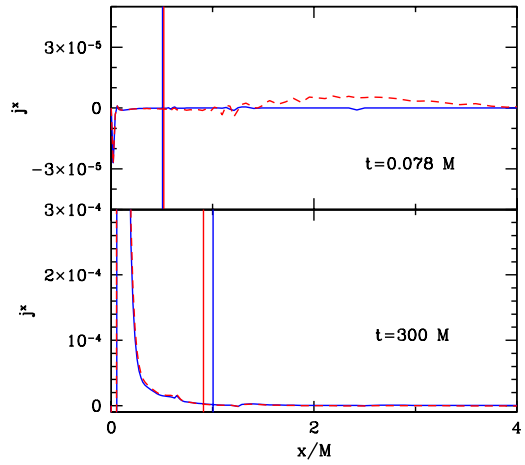

Figure 5.11. Same as in Fig. 5.10 but for the momentum constraint violation S^x. The constraint violations still present at late times are due to discretization around the puncture.

with a smaller mass. A similar situation occurs in the binary case; the system relaxes to a binary solution, but this solution is different than the vacuum case. The reason for this relaxation to a similar constraint-satisfying system is thought to be connected to the constraint damping nature of the BSSN formulation, but it is not fully understood.

5.6 Impact on Data Analysis

Finally, we want to address the extent to which the waveforms from evolutions of skeleton initial data may be of use in exploring gravitational wave astronomy. We will focus on computing the matches between the skeleton and the constraint-satisfying waveforms. In principle, the match would be between the detector output, h_1 and the template, h_2. Here h_1 is the waveform from the constraint-satisfying evolution and h_2 from the skeleton initial data evolution. Specifically, we will compare the waveforms using the minimax match given by [79, 146, 66].

$$\text{Match} \equiv \max_{t_0} \min_{\Phi_2} \max_{\Phi_1} \frac{\langle h_1 | h_2 \rangle}{\sqrt{\langle h_1 | h_1 \rangle \langle h_2 | h_2 \rangle}}, \tag{5.43}$$

where the inner product of two templates is defined by

$$\langle h_1 | h_2 \rangle = 4\,\text{Re} \int_{f_{\min}}^{f_{\max}} \frac{\tilde{h}_1(f)\tilde{h}_2^*(f)}{S_h(f)}\, df. \tag{5.44}$$

The match is maximized over the time of arrival of the signal, t_0, and minimized/maximized over the initial phase, Φ_1 and Φ_2, of the orbit when the signal/template enters the LIGO band. The variable $S_h(f)$ denotes the noise spectrum for which we use the initial [120] and advanced LIGO noise curves [5]. The domain $[f_{\min}, f_{\max}]$ is determined by the detector bandwidth and the masses of our signal – set such that the initial frequency of the numerical waveform just enters the LIGO band. We have chosen to study the match for values of the total mass of the BBH system greater than $20M_\odot$ because of the limited number of cycles that our waveforms include, stopping at $130M_\odot$ for initial LIGO and $250M_\odot$ for advanced LIGO as the ringdown-dominated match at such masses is close to unity. A more detailed description of our minimax match calculation is given in [183].

The match between the constraint-satisfying and skeleton data versus mass is plotted in Fig. 5.12 for both noise curves. In general, the match between the waveforms increases with increasing total mass, reaching > 0.99 at $60M_\odot/100M_\odot$ for initial/advanced LIGO . At such large total mass, the signal is dominated by the plunge and ringdown. Comparisons of the plunge and ringdown show (see Fig. 5.7) that the difference between the skeleton and constraint-satisfying evolution are very small. At masses lower than about $40M_\odot$, the match drops below 0.97 due to the difference in the binary dynamics prior to merger. Overall, advanced LIGO is more sensitive to differences in the data, but these differences still remain above 0.98 for most of the

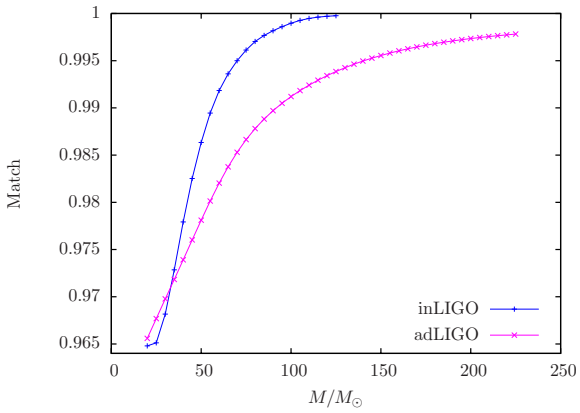

Figure 5.12. Waveform matches between the waveform extracted from the standard, D10e, and that extracted from the skeleton initial data evolution, D10a, using both the initial and advanced LIGO noise curves.

mass range investigated indicating that it is unlikely to have an impact on detection. Despite the high match, the differences between the data due to constraint violations would likely impact the accuracy of parameter estimation. We note that our calculation of match did not maximize over the mass of the two waveforms. Maximizing over the mass would have diminished the differences between the two waveforms.

5.7 Conclusions

We have carried out a study of the evolution of skeleton, puncture BBH initial data as proposed by [78]. We focused on non-spinning punctures at initial separations of 10 M, where the difference in binding energy with the constraint-satisfying initial data is $< 2\%$. We showed that during the inspiral the skeleton data yields different dynamics; however, this difference significantly diminishes as the binary enters the plunge, merger and ringdown.

We tested the match between the constraint-satisfying and skeleton data for a series of total masses between $20M_\odot$ and $130M_\odot/250M_\odot$ for initial/advanced LIGO respectively. Our results indicate that gravitational wave data analysis would have some tolerance for constraint-violating data, especially for those binaries in which the signal is plunge-merger dominated, as is the case of high mass BHs. We conclude that although the two systems were different, with one clearly violating the Einstein equations, the differences were not enough to impact the match statistics for the mass ranges we included in our study and for the number of cycles present in our numerical waveforms. Clearly, the advanced LIGO detector was more sensitive to the errors that are introduced into the system by the constraint violations. If these systems were evolved starting with a larger initial BH separation, the constraint violations would be smaller and, therefore, the waveforms generated could be useful for detection over the complete BBH mass range for initial LIGO. If, however, larger constraint violations are present in the data that drive the early BH mass lower,

the differences may lead to errors in parameter estimation.

We also analyzed the impact of the Hamiltonian constraint violations. We showed that the main feature of the skeleton data is two packets of negative constraint violations in front of and behind the BH, along the direction of its momentum. We conjectured that these negative constraint violations acted as a source density that gets absorbed by the BHs during evolution. To test our conjecture, we considered a model consisting of a single, non-rotating puncture in which we artificially added a stationary Gaussian shell source that mimics the Hamiltonian constraint violations in the skeleton data. The evolutions of this single puncture model reproduce the decrease in the mass of the BH observed in the evolution of the skeleton data.

One remarkable aspect of our study is the ability of the BSSN equations and moving puncture gauges to stably evolve data away from the constraint surface. What is even more remarkable is how the evolution brings the data back to the Einstein constraint surface. We are currently investigating a broader class of solutions with this property.

Our results suggest that for the class of constraint violations found in the above studies, the evolutions of such systems with the BSSN formulation approach a constraint-satisfying system with BHs of different AH masses. For general classes of constraint violations we cannot conclude anything from this study.

In summary, our numerical evolutions show that the skeleton initial data proposed by [78] embeds the BHs in a “cloud” of negative constraint violations. These constraint violations act as a source field that when accreted by the BHs decreases their masses. The change in the masses modifies the binding energy of the binary and thus affects its orbital dynamics (e.g., adding eccentricity) but had little effect on the match of the two waveforms for initial or advanced LIGO for high mass black holes. The observed effects will decrease as the initial binary separation increases.

Chapter 6

Theoretical Framework: Coupling Hydrodynamics to a Relativistic Code

"We are all dependent on one another, every soul of us on earth." – *George Bernard Shaw*

As we exist, the universe is not all vacuum. In general relativity, spacetime and matter evolve together, each directing the other. Matter, however, adds a completely new set of length scales to the problem. By evolving *realistic* matter, we must also grapple with its shock waves, instabilities, turbulence, electromagnetic fields, and even chemistry and composition. A few codes attempt to incorporate all of these in their study of gravitational core collapse and the subsequent cause of core-collapse supernovae, but including all of these is much too computationally expensive for the time scales we must simulate for BBH systems and of questionable importance to the scale of phenomena we wish to consider.

There are many methods used in describing and evolving matter in general relativity. The gridless smooth particle hydrodynamics (SPH) treatment such as that used in [145] uses a set of extended Lagrangian particles and is currently extended to relativistic circumstances but only includes self-gravity terms. Not only is the spacetime coupling minimal in such treatment, but difficulties arise in boundary conditions, hydrodynamic instabilities, and resolving physics at many length scales (see e.g., [4]). On the other hand, some hydrodynamics codes like `CoCoNuT` [69] use spectral methods which *can* cover many length scales well with their quick convergence. These have been developed extensively for use with spectral spacetime evolution codes [153]. Like the codes `GENESIS` [8], `SACRA` [188], and the unnamed code of Duez [72], the method we employ uses a conservative formulation [132, 110, 111] of an Eulerian approach [186].

As general relativity is a field theory, we describe the matter in a way that lends itself well to the framework already in place: describing it as a matter *field* defined everywhere with its variables stored at the verticies of a grid structure and evolved using finite differencing methods. This chapter will detail the important aspects of evolving coupled relativistic hydrodynamic fields which are implemented in `Scotch`

and used in Chapter 7 (see Font [82] for a more general review of methods in general relativistic hydrodynamics). `Scotch` is based on the publicly-available hydrodynamics code `Whisky` [22] but altered to use the HydroBase infrastructure being added to the CactusEinstein Cactus repository and extra functionality to handle the BHs from puncture spacetime initial data (see Sec. 3.1.3) among other structural changes. Like `MayaKranc`, `Scotch` is based on a the `Cactus` infrastructure and evolution systems are evolved by the Method of Lines.

6.1 Matter Evolution Equations

In general relativity, a matter field couples to the spacetime evolution through the creation of the stress-energy-momentum tensor $T_{\mu\nu}$, present on the right-hand side of the Einstein equations. Aside from letting the spacetime know about the matter through $T_{\mu\nu}$ the matter itself must evolve, interacting both with itself and with the curvature of spacetime. For a general matter field, this evolution is captured by the equations

$$\nabla_\mu T^{\mu\nu} = 0 \tag{6.1}$$

where ∇_μ is the covariant derivative of the full four-dimensional metric.

In our work, we assume the stress-energy-momentum tensor of a perfect fluid. That is, we choose $T_{\mu\nu}$ to be of the form

$$T^{\mu\nu} = \rho_o h u^\mu u^\nu + P g^{\mu\nu} \tag{6.2}$$

where ρ_o is the rest-mass density of the fluid, $h \coloneqq 1 + \epsilon + P/\rho_o$ is the specific enthalpy of the fluid , ϵ is the internal energy of the fluid, u^μ is the co-moving four-velocity, and P is the pressure. For a fluid stress-energy tensor as such we can reconsider the evolution equation (Eq. 6.1) under the same foliation of spacetime as used in formulating the spacetime evolution equations. The temporal projection of Eq. 6.1

$$n^\nu \nabla_\mu T^\mu_{\ \nu} = 0 \tag{6.3}$$

can be interpreted as local energy conservation as seen from considering the non-relativistic limit. Similarly, the spatial projection,

$$\perp^\nu_i \nabla_\mu T^\mu_{\ \nu} = 0 \tag{6.4}$$

is interpreted as local momentum conservation. To create a realistic fluid field, it is also standard to impose baryonic conservation

$$\nabla_\mu \left(\rho_o u^\mu\right) = 0. \tag{6.5}$$

The co-moving four-velocity u^μ must be normalized such that $u^\mu u_\mu = -1$ to be physical, so it is standard to introduce a spatial velocity vector v^i derived from u^μ in different ways depending on the formulation. At this point there are six unknowns $\left(\rho_o, \epsilon, P, v^i\right)$ and five evolution equations. The remaining degree of

freedom is specified by assuming an equation of state, generally written as defining the pressure P as a function of the rest-mass density and internal energy: $P = P(\rho_o, \epsilon)$. Thus the matter field is described by five physically-interpretable variables ρ_o, ϵ, and v^i, dubbed the "primitive" variables.

These primitive variables are convenient for analysis, but they are not ideal for evolving. Since Wilson's seminal work [186] on formulating the Eulerian description in general relativity many studies utilized formulations based on evolving the primitive variables directly while others used formulations based on the conservative approach of Martí *et al.* [132, 110, 111] and Banyuls *et al.* [29]. These conservative formulations rewrite the matter evolution equations in the form

$$\frac{1}{\sqrt{-g}}\left(\partial_t\left(\sqrt{\gamma}\boldsymbol{C}\right) + \check{\nabla}_{x^i}\left(\sqrt{-g}\boldsymbol{\mathcal{F}}^{(i)}\right)\right) = \boldsymbol{\mathcal{S}} \tag{6.6}$$

where $\boldsymbol{C}$ is a set of "conserved" variables, $\boldsymbol{\mathcal{F}}^{(i)}$ their related fluxes in the direction of x^j, and $\boldsymbol{\mathcal{S}}$ contains the source terms. The conservative form guarantees that the solution, should it converge, converges to a weak solution according to the Lax-Wendroff theorem. The choice of conserved variables $\boldsymbol{C}$ is not unique. Additionally, they make use of approximate Riemann solvers and High-Resolution Shock Capturing (HRSC) schemes which we will discuss later in this chapter.

Recently, Anninos and Fragile [12] showed the non-conservative formulations were insufficient for evolving ultra-relativistic matter fields. Unlike the non-conservative approach, that of Ibáñez avoids the need for artificial dissipation by solving a local characteristic problem via an approximate Riemann solver and utilizing a HRSC method to handle shocks.

6.1.1 Valencia Formulation

The formulation used in `Scotch` is dubbed the Valencia formulation [29] for its origins at the Universidad de Valencia. The primitive variables, ρ_o, ϵ, and v^i, are the rest-mass density, internal energy, and velocity as seen by a Eulerian observer at rest on the hypersurface moving along the normal to the hypersurface $n^\mu = \frac{1}{\alpha}\left(\partial_t - \beta^i\partial_i\right)$. The 3-velocity v^i of the matter field is defined with respect to the 4-velocity u^μ as

$$v^i := -\frac{n^i\partial_i}{n_\mu u^\mu} = \frac{1}{\alpha}\left(\frac{u^i}{u^t} + \beta^i\right) . \tag{6.7}$$

Following the approach of Banyuls *et al.*. [29], we rewrite the evolution equations derived from Eq. 6.1 in conservation form. In the Valencia formulation, we define our conserved variables as the set D, S^i, and τ defined as

$$D := \sqrt{\gamma}\rho_o W \tag{6.8a}$$

$$S^i := \sqrt{\gamma}\rho_o h W^2 v^i \tag{6.8b}$$

$$\tau := \sqrt{\gamma}(\rho_o h W^2 - P) - D \tag{6.8c}$$

where $W := \alpha u^t = \left(1 - v^i v_i\right)^{\frac{1}{2}}$ is the Lorentz factor from special relativity. We interpret these conserved variables by looking at their special relativistic limit. D reduces to the energy density of a boosted field, S^i is the relativistic momentum current of that boosted field, and τ is related to the internal energy of the field. Note that the conserved variable S^i defined here and used in this chapter and Chapter 7 is *not* the S^i of Chapter 2, but a "densitized" version: $S_i \rightarrow \sqrt{\gamma} S_i$. The notation here conforms to standard notation.

Written explicitly in terms of the conserved variables in the standard spacetime foliation, the system of matter evolution equations (Eq. 6.1 and 6.5) can be rewritten in the conservative form as

$$\partial_t D + \partial_j((\alpha v^j - \beta^j)D) = 0 \tag{6.9a}$$

$$\partial_t S_i + \partial_j((\alpha v^j - \beta^j)S_i + P\delta_i^j) = T^{\mu\nu}(\partial_\mu g_{\nu i} + \Gamma^\delta_{\mu\nu} g_{\delta i}) \tag{6.9b}$$

$$\partial_t \tau + \partial_j((\alpha v^j - \beta^j)\tau + P v^j) = \alpha\sqrt{\gamma}(K_{\mu\nu}T^{\mu\nu} + T^{0i}(2K_{ij}\beta^j - \partial_i\alpha) + T^{00}(K_{ij}\beta^i\beta^j - K_{ij}\beta^i\partial^j\alpha)). \tag{6.9c}$$

Notice that we evolve not S^i but S_i as the evolution equation is much simpler in that case.

6.2 Important Aspects of a (Conservative) Hydrodynamics Code

The current successes in evolving relativistic hydrodynamic systems using finite-differencing schemes involve several crucial theoretical tools. As mentioned earlier, by solving the relativistic hydrodynamic evolution equations in their conservative form we can avoid adding artificial dissipation with all its thorny issues. We *do*, however, need a reconstruction technique, a Godunov-type finite differencing scheme and HRSC. We also need to carefully treat areas of the hypersurface with little or no matter, and consider carefully the matter field evolutions around the punctures.

6.2.1 Finite Differencing Scheme: Godunov Method and HRSC

The coupled matter evolution equations (Eq. 6.9) require special finite differencing methods to guarantee that the system converges to a solution. Thankfully a half-century of research on conservative evolutions in the fluid dynamics community and considerable efforts on special relativistic hydrodynamics by the astrophysics community can be drawn upon. For the past 50 years, much research and development has gone into Godunov-type methods for solving partial differential equations written in conservative form and solved on a grid [182].

Godunov methods specifically address evolutions of functions represented by data on a grid where certain quantities must be conserved. These data are interpreted as piecewise-constant functions littered with theoretical shock waves on the scale of the grid spacing. The evolution proceeds by setting up and solving the Riemann problem, the problem of evolving a conservative differential equation at a discontinuity, at each of the 6 theoretical shocks bordering a cell defined by a grid point we wish to evolve. In the analytical

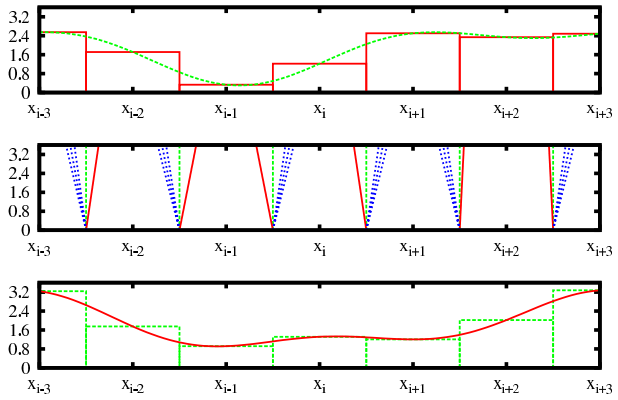

Figure 6.1. Schematic of Godunov-type methods. The top panel depicts the representation of a continuous function by a piecewise-constant function. The middle panel shows the characteristic lines of the Riemann problem solution at the discontinuities, composed of three different elementary waves. The bottom panel represents a time-averaged evolution of these waves and subsequent representation by the next piecewise-constant function.

solution to the Riemann problem, the discontinuity breaks up into three elementary waves: shock waves, rarefaction waves, and contact discontinuities. The contact discontinuity, an interface across which some hydrodynamic variables are discontinuous, remains at the cell border. On either side of the border either shock waves or rarefaction waves propate outwards at speeds characteristic of the material. The new time step is created from propagating these waves in time for a time interval no longer than that needed for the fastest such waves to interact with the waves emanating from the other side of the cell. A schematic of a Godunov-type method for a one-dimensional system is found in Fig. 6.1 where the lines in the middle panel are the characteristic lines found in solving the local Riemann problem.

Effectively applying a Godunov-type method requires a choice in Riemann solver for the cell interfaces [109]. There are many to choose from, both approximate and exact, depending on the problem at hand. The solvers available in `Scotch` (Roe, Marquina, or HLLE) use a characteristic approach to solve the Riemann problem. That is, they consider the three 5x5 Jacobian matrices $\mathcal{B}^i$ defined by

$$\mathcal{B}^i := \alpha \frac{\partial \mathcal{F}^{(i)}}{\partial \mathcal{C}}. \tag{6.10}$$

Each Jacobian leads to the flux into and out of the cell along one spatial coordinate. The eigenvalues of this Jacobian define the material and acoustic waves in this direction where the eigenvalues lead to left and right eigenvectors (see App.D) to decompose the variables into characteristic waves.

In the absence of sources (Cartesian Minkowski background), the Riemann problem can be solved exactly [133]. The situations which interest us, though, do not satisfy this. An important assumption made in such cases is that the resolution of the spacetime mesh is high enough that locally you can change coordinates to a flat spacetime. Given this assumption, the past twenty years have shown remarkable progress in solving hydrodynamics on flat space. Anile [11] thoroughly discusses the hyperbolic nature of the hydrodynamic

and magnetohydrodynamic evolution equations on a Minkowskian background, a discussion extended to an arbitrary reference frame by Font *et al.* [81]. Solving the Riemann problem exactly is also a very expensive procedure as it involves solving an implicit equation. Approximate Riemann solvers are often sufficient in catching much of the system dynamics, though they can also fail spectacularly [157]. For our work we use an approximate Riemann solver, the Marquina solver, derived first by Donat and Marquina [70], modified by Aloy *et al.* [8] and extended to general relativity by Frieben, Ibáñez and Pons. We leave a discussion of this solver to Appendix D.

Godunov-type methods are often extended to include HRSC schemes in their set-up of the Riemann problem. These determine how the fluxes derived from the Riemann problem solutions are used in calculating the evolution of the conserved variables, particularly how the time-averaging of the fluxes from the characteristic solution to the Riemann problem is performed. In `Scotch`, we solve the conservative form of the evolution equations by considering the 4-dimensional cell created by a gridpoint-centered spatial cell extended into the space between hypersurfaces Σ_t and $\Sigma_{t+\Delta t}$.

$$\int_\Omega \frac{1}{\sqrt{-g}}\frac{\partial(\sqrt{\gamma}\boldsymbol{C})}{\partial t}d\Omega + \int_\Omega \frac{1}{\sqrt{-g}}\frac{\partial(\sqrt{-g}\boldsymbol{\mathcal{F}}^{(i)})}{\partial x^i}d\Omega = \int_\Omega \boldsymbol{\mathcal{S}}d\Omega\,. \tag{6.11}$$

Averaging this equation over the spatial cell and dividing by the volume we find an evolution equation for the integral-averaged conserved variables

$$\frac{d}{dt}\bar{\boldsymbol{C}} = \bar{\boldsymbol{\mathcal{S}}} + \frac{1}{\Delta V}\int_t^{t+\Delta t}\int_{x^2-\Delta x^2/2}^{x^2+\Delta x^2/2}\int_{x^3-\Delta x^3/2}^{x^3+\Delta x^3/2}\left\{\boldsymbol{\mathcal{F}}^{(1)}\left(C(x^1-\Delta x^1/2,y,z)\right)-\boldsymbol{\mathcal{F}}^{(1)}\left(C(x^2+\Delta x^1/2,y,z)\right)\right\}dtdydz+... \tag{6.12}$$

where

$$\bar{\boldsymbol{C}} \;\coloneqq\; \frac{1}{\Delta V}\int_V \sqrt{\gamma}\,\boldsymbol{C}dx^1dx^2dx^3\,, \tag{6.13a}$$

$$\Delta V \;\coloneqq\; \int_{x^1-\Delta x^1/2}^{x^1+\Delta x^1/2}\int_{x^2-\Delta x^2/2}^{x^2+\Delta x^2/2}\int_{x^3-\Delta x^3/2}^{x^3+\Delta x^3/2}\sqrt{\gamma}dx^1dx^2dx^3 \tag{6.13b}$$

and $\bar{\boldsymbol{\mathcal{S}}}$ is defined similarly to $\bar{\boldsymbol{C}}$. Thus the evolution of the conserved variables can be written in a manner suited for the method of lines as

$$\frac{d}{dt}\bar{\boldsymbol{C}} = \bar{\boldsymbol{\mathcal{S}}} + \int_{x^2_{j-1/2}}^{x^2_{j+1/2}}\int_{x^3_{k-1/2}}^{x^3_{k+1/2}}\left\{\hat{\boldsymbol{\mathcal{F}}}^{(1)}\left(\boldsymbol{C}(x^1_{i-1/2},y,z)\right)-\hat{\boldsymbol{\mathcal{F}}}^{(1)}\left(\boldsymbol{C}(x^1_{i+1/2},y,z)\right)\right\}dydz+\dots\,. \tag{6.14}$$

The fluxes, $\hat{\boldsymbol{\mathcal{F}}}^{(i)}$ are calculated by the Riemann method discussed in App. D which addresses the time averaging of the fluxes in the final alteration of the flux formula.

6.2.2 Reconstruction: Piecewise Parabolic Method (PPM)

Setting up the Riemann problem from above uses the conserved variables on either side of a cell interface. The popular method we use is the Piecewise Parabolic Method (PPM) [62]. We assume the variable q is a scalar function of x, the dimension we are reconstructing along, and interpolate a quadratic polynomial to the cell boundary.

$$q_{i+1/2} = \frac{1}{2}(q_{i+1} + q_i) + \frac{1}{6}(\delta_m q_i - \delta_m q_{i+1}) \tag{6.15}$$

where

$$\delta_m q_i = \begin{cases} \text{sign}(\delta q_i)\min(|\delta q_i|, 2|q_{i+1} - q_i|, 2|q_i - q_{i-1}|) & \text{if}(q_{i+1} - q_i)(q_i - q_{i-1}) > 0 \\ 0 & \text{otherwise} \end{cases} \tag{6.16}$$

$$\delta q_i = \frac{1}{2}(q_{i+1} - q_{i-1}) \tag{6.17}$$

Setting the variable value on both the left and right of the cell interface as equivalent ($q_i^R = q_{i+1}^L = q_{i+1/2}$) results in oscillatory behavior in the vicinity of shocks.

The PPM includes the option to sharpen discontinuities for reconstructions of the matter density, or to flatten the zone structure near shocks by adding simple dissipation. Whether either option is used, we avoid oscillatory behavior by making the following replacements to preserve monotonicity:

$$q_{i+1}^L \to q_i^R = q_i \qquad \text{if} \quad (q_i^R - q_i)(q_i - q_{i+1}^L) \le 0 \tag{6.18a}$$

$$q_{i+1}^L \to 3q_i - 2q_i^R \qquad \text{if} \quad (q_i^R - q_{i+1}^L)\left(q_i - \frac{1}{2}(q_{i+1}^L + q_i^R\right) > \frac{1}{6}(q_i^R - q_{i+1}^L)^2 \tag{6.18b}$$

$$q_i^R \to 3q_i - 2q_{i+1}^L \qquad \text{if} \quad (q_i^R - q_{i+1}^L)\left(q_i - \frac{1}{2}(q_{i+1}^L + q_i^R\right) < \frac{1}{6}(q_i^R - q_{i+1}^L)^2 \,. \tag{6.18c}$$

The PPM then gives us the set of conserved and primitive variables on both sides of a cell interface which we can use to set up a Riemann problem. For more detail, see Appendix D.

6.2.3 Recovery of Primitives

As discussed above, the hydrodynamic variables evolved by `Scotch` are the set of conserved variables $\boldsymbol{C} = \{D, S_i, \tau\}$. While useful, they themselves are not easily interpreted. Instead, after every timestep we convert back to the primitive variables $\{\rho_o, v^i, \epsilon\}$. We also store the Lorentz factor $W = \alpha u^0$ and the pressure P to speed calculations and simplify analysis though both can be derived from the basic primitive variables.

Recovering the primitives from the conserved variables requires a bit of algebraic gymnastics. As with most things there are several methods to find the primitives that correspond to the new conserved variables [114]. The procedure in place, detailed in Appendix D, involves "undensitizing" the conserved variables through division by $\sqrt{\gamma}$. This projects the conserved variables onto a nearly flat spacetime, removing

any strong gravitational contribution. We then proceed to use a Newton-Raphson type iteration to minimize a function which constrains the definition of the conserved mass/energy density for a polytropic equation of state ($\rho_o W = D/\sqrt{\gamma} = \check{D}$) and otherwise constrains the equation of state itself ($P = P(\rho_o, \epsilon)$).

6.2.4 Atmosphere Handling

In regions of sufficiently small or vanishing densities, the matter field of Eulerian codes must be handled carefully. In the vacuum limit, the speed of sound approaches the speed of light and the Riemann problem as well as the conversion between conserved and primitive variables fails. In many cases the matter field is confined to a small region of space (e.g., a star) so confining the matter evolution to just the vicinity of the non-trivial matter field also increases the efficiency of the code. The current rule of thumb [89] is to allow ~ 7 orders of magnitude below the initial data's peak matter density to remain dynamic. Anything below that is not evolved: its velocity is set to zero and its density set to the atmospheric value. The region around non-atmospheric matter is given the opportunity to become non-atmosphere.

6.2.5 Physicality

With the exception of Faber *et al.*'s study on hydrodynamics with punctures [77], fully-relativistic hydrodynamic studies of BH systems have been done on spacetimes with the BHs excised from the evolved spacetime. In our studies with `Scotch`, though, we continue to use the proven puncture approach of Sec. 3.1.3 for the BHs. This requires some special handling in the vicinity of the puncture as numerical error quickly causes the momentum to diverge. This error is primarily found in the conversion from the conserved variables to the primitive variables. Following Faber *et al.* [77], we impose the physicality of the matter field everywhere on the conservative variables before converting to the primitive variables, where an unphysicality would be amplified.

The specific enthalpy, $h := 1 + \epsilon + P/\rho_o$, satisfies $h \geq 1$ for physical matter where $h \to 1$ is the dust limit. In this dust limit, $\tau \to D(W-1)$ as can be readily seen from its definition in Eq. 6.8.

The dust limit on the magnitude of S^i is derived from the requirement that $u_\mu u^\mu = -1$. This can be rewritten in terms of the conserved variables as

$$\gamma^{ij}\frac{S_i S_j}{h^2} = D^2(W^2 - 1). \tag{6.19}$$

Combining this with the definition for τ, we find that as $h \to 1$,

$$|S|^2 = \gamma^{ij} S_i S_j \to \tau(\tau + 2D). \tag{6.20}$$

It can be shown that this is an upper limit. In our simulations we keep our total matter current well within this limit by impose an upper limit on its magnitude of $0.98\tau(\tau + 2D)$ as per Faber *et al.* [77].

Chapter 7

The Effects of Surrounding Gas on Binary Black Hole Mergers

> "Clouds come floating into my life, no longer to carry rain or usher storm, but to add color to my sunset sky." – *Rabindranath Tagore*

Black holes do not exist in vacuum; they have accretion disks and sometimes, as in the case of Active Galactic Nuclei (AGN), relativistic jets. Simulations of BBH systems to date have not considered the effects of any surrounding matter on merging BBHs in the fully non-linear relativistic regime. Nevertheless, matter is expected to play a non-trivial role in the merger dynamics. Accretion disks, for instance, may provide torque such that the BHs' spins slowly align [39] which feeds back into the orbital dynamics via the spin-orbit coupling. In fact, Armitage *et al.* [15] noted that a gas medium could speed the merger of BBHs from eccentric binaries in such a way that LISA may be able to detect a signal encoded with physics beyond the standard vacuum BBH waveforms currently being generated en masse. In this chapter we take the first steps to considering these questions through fully-coupled, nonlinear simulations.

Early N-body simulations by Milosavljevic and Merritt [136] and subsequent studies [194, 35] found supermassive BBH inspirals stalled at 0.01-1 parsecs. In these studies, for sufficiently massive BBH mergers ($M \gtrsim 10^8 M_\odot$), three-body interactions with stars in the galaxy are no longer sufficient to extract enough angular momentum from the pair for the BHs to merge. At that distance, gravitational wave radiation alone merges the BBH on a timescale of the order of a Hubble time since circularized BBHs are much less efficient at emitting angular momentum through gravitational radiation. For these supermassive BBHs, angular momentum transportation via surrounding gas may be a dominant mechanism in hastening a merger [32, 93, 14, 75, 76]. A recent numerical study using post-Newtonian terms in N-body simulations found that incorporating relativity into such systems may be sufficient to overcome this stalled inspiral [154]. In another study, Cuadra *et al.* [64] evolved wet binaries using SPH around BBHs, suggesting hydrodynamics could be important in the last phase of the inspiral.

This chapter discusses a study in progress which aims at addressing this question. In Sec. 7.1 we consider an initial system where the standard BBH vacuum initial data is embedded in a *stationary* gas cloud whose density is astrophysically motivated. In Sec. 7.2 we discuss the current progress in evolving wet BBHs.

7.1 Initial Data

7.1.1 Constraint Solving with Matter

Spacetimes coupled with matter must start with constraint-satisfying initial data which are once again coupled. Consider the constraint equations (Eq. 3.6) from Chapter 3 with the matter fields reinserted

$$\tilde{\nabla}^i\tilde{\nabla}_i\psi - \frac{1}{8}\psi\tilde{\mathcal{R}} - \frac{1}{12}\psi^5 K^2 + \frac{1}{8}\psi^{-7}\tilde{A}_{ij}\tilde{A}^{ij} = -2\pi\psi^5\rho, \tag{7.1a}$$

$$\check{\nabla}_j(\psi^{-10}\tilde{A}^{ij}) - \frac{2}{3}\check{\nabla}_j K = 8\pi\psi^{10}\tilde{\gamma}^{ij}J_j \tag{7.1b}$$

where we replaced the S_j from the vacuum chapters with J_j to avoid confusion. The matter quantities ρ and J_j can now be written in terms of primitive variables using the perfect fluid stress-energy-momentum tensor as

$$\rho \coloneqq n_\mu n_\nu T^{\mu\nu} = \rho_o(1+\epsilon)W^2 + P\left(W^2 - 1\right), \tag{7.2}$$

$$J_j \coloneqq -\perp^\nu_j n_\mu T^{\mu\nu} = \rho_o h W^2 v_j = \frac{1}{\sqrt{\gamma}}S_j\,. \tag{7.3}$$

The popular method to solve these coupled equations is based on the extended thin sandwich method, but in this work we follow a different approach. By imposing our initial matter field be stationary, S_j vanishes initially, uncoupling the constraints again. Though a cloud of matter surrounding a binary system would not be stationary, this was a first step towards solving spacetimes containing matter, inspired by the alterations already in place for Sec. 5.5. Stationary matter simplifies the momentum constraint so the Bowen-York approach is again applicable. Our initial extrinsic curvature is again given by Eq. 3.12.

To create a *physical* matter field, solving the Hamiltonian constraint is more complicated than discussed in Sec. 5.5. Following the approach of Löffler *et al.* [126] for their Black Hole – Neutron Star (BHNS) initial data, we again rescale the quantity ρ by several factors of the BY conformal factor to guarantee the existence of a solution [61]. We rescale ρ as

$$\hat{\rho} = \psi^n\rho \tag{7.4}$$

where n must satisfy $n > 5$ so the source term in the Hamiltonian constraint is rewritten as $-2\pi\psi^{5-n}\hat{\rho}$. This is sufficient to guarantee a unique solution. As has become standard, we choose $n = 8$ such that the constraint equation is written

$$\tilde{\nabla}^i\tilde{\nabla}_i\psi - \frac{1}{8}\psi\tilde{\mathcal{R}} - \frac{1}{12}\psi^5 K^2 + \frac{1}{8}\psi^{-7}\tilde{A}_{ij}\tilde{A}^{ij} = -2\pi\psi^{-3}\hat{\rho}\,. \tag{7.5}$$

We compute $\hat{\rho}$ using a modified single-domain spectral method from Ansorg [13] and an initial guess for ρ. We keep the conformal factor ψ used in the rescaling fixed to our initial guess while we solve for the conformal factor.

As an additional complication, the quantity which feeds into the constraint equation is only the rest-mass density in the dust limit. For general stationary matter, the matter quantity ρ in the Hamiltonian constraint reduces to

$$\rho = \rho_o(1 + \epsilon). \tag{7.6}$$

We set the form of ρ to be a sum of (positive) Gaussians and solve the Hamiltonian constraint using a modified single-domain pseudo-spectral method from Ansorg [13]. With the final conformal factor ψ and the imposed ρ, we use a Newton-Raphson iteration to find a set of primitive variables which are consistent with the equation of state and ρ.

7.1.2 Choosing a Matter Field and Binary

In our current evolutions we embed the standard BBH used in Chapter 5, the D10 run of Tichy *et al.* [179], inside a Gaussian gas cloud large enough to encompass both BHs. Our choice in the peak of our Gaussian matter clouds is inspired by studies of the Central Molecular Zone (CMZ) in the center of the Milky Way as reviewed by Morris and Serabyn [138]. This zone, $\sim$ 200 pc in radius has been observed through emissions of CO lines from its surface. From this observation the surface matter density is estimated at $\sim 5\mathrm{M}_\odot/\mathrm{pc}^2$. Within this area the number density of CO is expected to be, on average, $10^4\mathrm{cm}^{-3}$. Given CO has a mass of 28 g/mole, for a spacetime with an ADM mass of 1 in code units representing a system of total mass $M_{\rm sys} = N\mathrm{M}_\odot$ the energy density is given by

$$\rho_{(\rm cgs)} = \frac{c^6}{M^2G^3}\rho_{\rm code} = \frac{7.6971\times10^7}{N^2}\rho_{\rm code}\ \frac{\rm g}{\rm cm^3}. \tag{7.7}$$

Thus a Gaussian peak at 10^{-5} in code units yields a physical density corresponding to $(7.697{\times}10^2/N^2)\,\mathrm{g/cm}^3$ which is equivalent to the CMZ's estimated density for a $4\times10^{10}\mathrm{M}_\odot$ system. For all the work in this chapter we assume, for simplicity, a polytropic equation of state

$$P = \kappa\rho_o^\Gamma. \tag{7.8}$$

This is a form of the ideal fluid which eliminates the need for the conserved variable τ to be evolved, decreased the computational expense of simulations.

In Table 7.1 we summarize the parameters used to build our initial spacetime as well as the physical properties of the resulting spacetime. As expected, the stationary matter field did not change the ADM angular momentum of the system, but it did add an additional 2.4% ADM energy. The presence of the matter field increased the AH masses of the BHs increased by only 0.09%. In Fig. 7.1 we present a surface

Run	D/M	$\lvert P^y\rvert/M$	ρ_o/M^2	σ/M	$\kappa/(M^{2(\Gamma-1)})$	Γ	$\mathcal{M}_{AH}/M$	$\mathcal{E}_{\rm ADM}/M$	$\mathcal{J}_{\rm ADM}/M^2$
Dry	10.0	0.0954325	–	–	–	–	5.000	0.9895	0.9531
Wet	10.0	0.0954325	1.083×10^{-5}	10.83	100	2	0.5004413562	1.0133	0.9531

Table 7.1. Overview of the properties of the initial data considered in this work. Here D/M is the coordinate separation of the binary, $|P^y|/M$ is the initial momentum of the BHs. ρ_o/M^2 and σ/M describe the geometry of the matter field. κ and Γ are the parameters for the equation of states. The final three columns describe the AH masses, ADM energy, and ADM angular momentum respectively.

plot of the rest-mass density ρ_o/M^2 in the area surrounding the BHs.

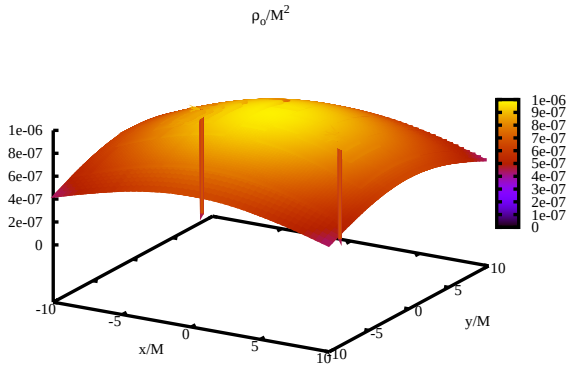

Figure 7.1. Surface plot of the rest-mass matter density ρ_o/M^2 across the xy-plane. The BHs are at $x = \pm 5$ as can be seen by the dropping density at the site of the punctures.

7.2 Current Progress

We have created the above "wet" BBH system and evolved it using the `MayaKranc` code coupled to `Scotch`. Thus far I have not been successful simulating *orbiting* BBH systems to and through merger. Roland Haas has shown that head-on collisions embedded in gas *can* be successful with this code, but the BBH system described above crashes after about $90M$, well after a head-on from the same separation would merge. The trouble currently lies in the vicinity of the puncture, within a grid point or two of the punctures themselves, where the curvature of the spacetime is great enough that the locally flat approximations made in `Scotch` are not sufficiently valid. When the density there becomes too high, the simulation crashes.

When a "wet" BBH system can successfully be evolved, the above initial data is just an entry point to a vast parameter space. Evolving eccentric binaries would study the effects of the gas on the circularization of the system. Spin and unequal masses would add more dimensions. All of these systems can shed light on the extent to which a surrounding gas cloud can affect the dynamics and subsequent gravitational wave

emissions from BBH systems, effects which may be observable with the next generation of gravitational wave observatories.

Chapter 8

Summary and Open Questions

"The important thing is not to stop questioning." – *Albert Einstein*

The recent breakthroughs in NR and subsequent frantic studies of waveforms and building of waveform template banks have changed the very nature of the field. No longer is NR a numerical side project of general relativistic studies, having fully realized its place as a connector between gravitational theory and experiment, the heart of matched-template signal searches, and relativistic astrophysics. The studies in this dissertation considered the robustness of generated waveforms for BBH mergers in the presence of the constraint violation, inaccuracies, and effects thereof still present in the initial data.

Not only did we find the waveforms robust to the spurious gravitational wave content present in standard initial spacetime (see Chapter 4), but we found that a full 1% additional $\mathcal{E}_{\rm ADM}$ can be added to such a standard BBH in the form of gravitational waves before the final BH is significantly altered. We additionally observed that such changes, when present, were consistent with the energy absorbed by the BHs while the spurious radiation flushed out of the system.

This study was expanded on in Chapter 5 where we considered a canonical choice in approximate initial data, representing the BHs as point sources in solving the ADM Hamiltonian on the initial hypersurface. We find that the Match between the waveforms generated by the skeleton and the standard initial data was sufficiently high (> 0.97) for binary systems with masses above $40M_{\odot}$, for both initial and advanced LIGO noise curves, that the resulting waveforms would be sufficient for signal detection purposes, though the differences could still lead to significant parameter estimation errors. Perhaps more important was the observation that the constraint violations were negative and, in certain regimes, can be interpreted as an unphysical energy field that gets absorbed by BHs as the constraint-violating system approaches a constraint surface of a BBH system with different masses.

In both the above studies, we found the dynamics of the AH masses during an evolution is a good indicator of the validity and accuracy of the generated waveform. In the first case the absorption of the waves increased the AH masses during inspiral while in the latter case the negative constraint violations

unphysically decreased it. Such an indicator is vital when more complicated spacetime configurations are considered, where the initial data is not so easily generated. The second study shows, after all, that for at least one type of approximate initial data, approximate can indeed be good enough for waveform generation in the LIGO band.

There are some caveats to these studies. The recent stringent requirements of Lindblom *et al.* [124] have yet to be taken into account. Similarly, the suspected small effects of issues with our wave extraction methods, as pointed out by Lehner *et al.* [121], have also not been considered in depth.

Beyond these conclusions and caveats, there remain many open questions. The above studies were done only for equal-mass, non-spinning BBHs. Spinning BHs, as discussed in Sec. 3.1.4, are implemented only through the extrinsic curvature. As such, they can produce much more spurious radiation. The question remains how much energy is seen in the resulting spurious radiation and how much does it change the AH masses of the BHs as it flushes out of the system. Similarly, the constraint violations from spinning BBHs in the skeleton initial data have not been considered. A follow-up side experiment which has not been published shows that if the AH mass of a spinning BH decreases enough for the dimensionless spin parameter to become extremal, the numerical solution diverges from the constraint surface and is no longer any use for generating waveforms. This would set an upper limit to the amount of constraint violations allowed in any initial data.

These studies can be extended in other directions as well. The interpretation of the constraint violations as matter fields is admittedly false, but it works in the sense of changing AH mass and the resulting convergence to a constraint surface begs the question of whether this is a feature of the BSSN formulation of Einstein's equations. A possible follow-up study [95] is to numerically evolve the constraint propagation system of equations on a single BH background to see what class of constraint violations damp away rather than diverge.

Finally, the results of these studies can be applied to other attempts at creating initial data such as the stitching of PN and perturbative regime solutions of Yunes *et al.* [195] or the PN initial data of Kelly *et al.* [115]. The degree of acceptable constraint violations or resulting spurious radiation can better guide the locations of the stitching regimes or delegate how many orders of PN must be used for sufficiently accurate initial data.

Currently still in progress, the work of Chapter 7 will eventually consider whether waveforms from BBHs detected by observatories like LIGO or LISA might contain information concerning the matter content surrounding the binary. The question would then become how dense the gas must be to significantly affect the BBH dynamics. If this is a physical density, these could also prove a valuable testbed for ultra-relativistic hydrodynamics, possibly feeding into studies of core-collapse supernovae which also require relativistic matter.

This dissertation could have addressed more of these questions, and indeed there are efforts currently underway to address some of them, but it is the way of science that there will always be more to under-

stand. As this dissertation stands, the robustness of the vacuum waveforms found in Chapter 4 will help in the detection of gravitational waves using the current template banks. The robustness of the waveforms generated in Chapter 5 question how well constraints must be satisfied for future, nontrivial systems as well as noting some behavior of the constraints in the BSSN formulation which may prove interesting to follow up on. Finally, the work in progress discussed in Chapter 7, while it may lead to a better understanding of how supermassive BBHs evolve through the last parsec, is primarily a bridge to the world of fully-nonlinear, fully-coupled ultrarelativistic hydrodynamics around BHs.

Appendix A

Weyl Scalars

A.1 Weyl Scalars on a Hypersurface

In Section 3.4 we considered only the derivations of Ψ_4 as this is the scalar used in waveform extraction. There are times, though, when consideration of the other four Weyl scalars is desirable. These Weyl scalars can be written in terms of the '3+1' hypersurface quantities in a fashion similar to that found in the Sec. 3.4 for Ψ_4.

Again, we construct the Weyl scalars from the project of the Weyl tensor $C_{\alpha\beta\gamma\delta}$ onto an array of tetrad components:

$$\Psi_0 = C_{\alpha\beta\gamma\delta}\mathrm{l}^\alpha \mathrm{m}^\beta \mathrm{l}^\gamma \mathrm{m}^\delta , \tag{A.1a}$$

$$\Psi_1 = C_{\alpha\beta\gamma\delta}\mathrm{l}^\alpha \mathrm{n}^\beta \mathrm{l}^\gamma \mathrm{m}^\delta , \tag{A.1b}$$

$$\Psi_2 = C_{\alpha\beta\gamma\delta}\mathrm{l}^\alpha \mathrm{m}^\beta \overline{\mathrm{m}}^\gamma \mathrm{n}^\delta , \tag{A.1c}$$

$$\Psi_3 = C_{\alpha\beta\gamma\delta}\mathrm{l}^\alpha \mathrm{n}^\beta \overline{\mathrm{m}}^\gamma \mathrm{n}^\delta , \tag{A.1d}$$

$$\Psi_4 = C_{\alpha\beta\gamma\delta}\mathrm{n}^\alpha \overline{\mathrm{m}}^\beta \mathrm{n}^\gamma \overline{\mathrm{m}}^\delta . \tag{A.1e}$$

We rewrite the Weyl tensor in terms of the full four-dimensional Riemann tensor $R_{\alpha\beta\gamma\delta}$ and its '3+1' decomposition. The Weyl scalars can be written as

$$\begin{aligned}\Psi_0 &= R_{ijkl}\mathrm{l}^i \mathrm{m}^j \mathrm{l}^k \mathrm{m}^l + 2R_{0jkl}(\mathrm{l}^0 \mathrm{m}^j \mathrm{l}^k \mathrm{m}^l - \mathrm{m}^0 \mathrm{l}^j \mathrm{l}^k \mathrm{m}^l) \\ &\quad + R_{0j0l}(\mathrm{l}^0 \mathrm{m}^j \mathrm{l}^0 \mathrm{m}^l + \mathrm{m}^0 \mathrm{l}^j \mathrm{m}^0 \mathrm{l}^l - 2\mathrm{l}^0 \mathrm{m}^j \mathrm{m}^0 \mathrm{l}^l) , \end{aligned} \tag{A.2a}$$

$$\begin{aligned}\Psi_1 &= R_{ijkl}\mathrm{n}^i \mathrm{l}^j \mathrm{m}^k \mathrm{l}^l + R_{0jkl}(\mathrm{n}^0 \mathrm{l}^j \mathrm{m}^k \mathrm{l}^l - \mathrm{l}^0 \mathrm{m}^j \mathrm{n}^k \mathrm{l}^l - \mathrm{l}^0 \mathrm{n}^j \mathrm{m}^k \mathrm{l}^l + \mathrm{m}^0 \mathrm{l}^j \mathrm{n}^k \mathrm{l}^l) \\ &\quad + R_{0j0l}(\mathrm{n}^0 \mathrm{l}^j \mathrm{m}^0 \mathrm{l}^l - \mathrm{n}^0 \mathrm{l}^j \mathrm{l}^0 \mathrm{m}^l - \mathrm{l}^0 \mathrm{n}^j \mathrm{m}^0 \mathrm{l}^l + \mathrm{l}^0 \mathrm{n}^j \mathrm{l}^0 \mathrm{m}^l) , \end{aligned} \tag{A.2b}$$

$$\Psi_2 = R_{ijkl}\mathrm{l}^i \mathrm{m}^j \overline{\mathrm{m}}^k \mathrm{n}^l + R_{0jkl}(\mathrm{l}^0 \mathrm{m}^j \overline{\mathrm{m}}^k \mathrm{n}^l - \mathrm{n}^0 \overline{\mathrm{m}}^j \mathrm{l}^k \mathrm{m}^l - \mathrm{m}^0 \mathrm{l}^j \overline{\mathrm{m}}^k \mathrm{n}^l + \overline{\mathrm{m}}^0 \mathrm{n}^j \mathrm{l}^k \mathrm{m}^l)$$

$$+R_{0j0l}(\mathfrak{l}^0\mathfrak{m}^j\overline{\mathfrak{m}}^0\mathfrak{n}^l - \mathfrak{l}^0\mathfrak{m}^j\mathfrak{n}^0\overline{\mathfrak{m}}^l - \mathfrak{m}^0\mathfrak{l}^j\overline{\mathfrak{m}}^0\overline{\mathfrak{m}}^l + \mathfrak{n}^0\mathfrak{l}^j\mathfrak{m}^0\overline{\mathfrak{m}}^l)\,, \tag{A.2c}$$

$$\Psi_3 = R_{ijkl}\mathfrak{l}^i\mathfrak{n}^j\overline{\mathfrak{m}}^k\mathfrak{n}^l + R_{0jkl}(\mathfrak{l}^0\mathfrak{n}^j\overline{\mathfrak{m}}^k\mathfrak{n}^l - \mathfrak{n}^0\overline{\mathfrak{m}}^j\mathfrak{l}^k\mathfrak{n}^l - \mathfrak{n}^0\mathfrak{l}^j\overline{\mathfrak{m}}^k\mathfrak{n}^l + \overline{\mathfrak{m}}^0\mathfrak{n}^j\mathfrak{l}^k\mathfrak{n}^l)$$
$$+R_{0j0l}(\mathfrak{l}^0\mathfrak{n}^j\overline{\mathfrak{m}}^0\mathfrak{n}^l - \mathfrak{l}^0\mathfrak{n}^j\mathfrak{n}^0\overline{\mathfrak{m}}^l - \mathfrak{n}^0\mathfrak{l}^j\overline{\mathfrak{m}}^0\mathfrak{n}^l + \mathfrak{n}^0\mathfrak{l}^j\mathfrak{n}^0\overline{\mathfrak{m}}^l)\,, \tag{A.2d}$$

$$\Psi_4 = R_{ijkl}\mathfrak{n}^i\overline{\mathfrak{m}}^j\mathfrak{n}^k\overline{\mathfrak{m}}^l + 2R_{0jkl}(\mathfrak{n}^0\overline{\mathfrak{m}}^j\mathfrak{n}^k\overline{\mathfrak{m}}^l - \overline{\mathfrak{m}}^0\mathfrak{n}^j\mathfrak{n}^k\overline{\mathfrak{m}}^l)$$
$$+R_{0j0l}(\mathfrak{n}^0\overline{\mathfrak{m}}^j\mathfrak{n}^0\overline{\mathfrak{m}}^l + \overline{\mathfrak{m}}^0\mathfrak{n}^j\overline{\mathfrak{m}}^0\mathfrak{n}^l - 2\mathfrak{n}^0\overline{\mathfrak{m}}^j\overline{\mathfrak{m}}^0\mathfrak{n}^l) \tag{A.2e}$$

where, for example, $R_{0jkl} = n^\alpha_\Sigma \perp^\beta_j \perp^\gamma_k \perp^\delta_l R_{\alpha\beta\gamma\delta}$.

Using the ADM '3+1' decomposition and following [52, 51, 54, 53], we can write the '3+1' decomposition of the Riemann tensor as

$$R_{ijkl} = \mathcal{R}_{ijkl} + 2K_{i[k}K_{l]j} \tag{A.3a}$$

$$R_{0jkl} = -2\left[\partial_{[l}K_{k]j} + \Gamma^p_{j[k}K_{l]p}\right] \tag{A.3b}$$

$$R_{0j0l} = \mathcal{R}_{jl} - K_{jp}K^p_l + KK_{jl}. \tag{A.3c}$$

The Weyl scalars are not a true scalars. Defined as projections of the Weyl tensor onto a tetrad basis, they are not invariant under a rotation of the tetrad. Just as tensors in general relativity can have weights, so can complex scalars related to the phase of their components. A quantity η of spin s transforms, under a rotation of angle ψ, as $\eta' = e^{-\imath s\psi}\eta$. Consider the effect on the Weyl scalars caused by a "spin" of the tetrad's complex components by an angle $\aleph$. The real tetrad components $\mathfrak{l}^\mu$ and $\mathfrak{n}^\mu$ remain unaltered. However, $(\mathfrak{m}^\mu)' = e^{\imath\aleph}(\mathfrak{m}^\mu)$. Applying this spin to Ψ_4, the two projections of the Weyl tensor onto $\overline{\mathfrak{m}}^\mu$ yields a transformation $\Psi'_4 = e^{-i2\aleph}\Psi_4$. Thus the Weyl scalar Ψ_4 is a spin 2 pseudo-scalar. Similarly derived, Ψ_3 is spin 1, Ψ_2 is spinless, Ψ_1 is a spin -1 pseudo-scalar, and Ψ_0 is spin -2.

Appendix B

Multipole Expansions

Expanding quantities on a basis of spherical harmonics has been a vital tool for both understanding physics and solving problems well beyond general relativity. Due to the gauge freedom of general relativity, not even scalars are simply scalars. From this basis, the array of bases has expanded, encompassing spin-weighted spherical harmonics, spherical vector harmonics, and spherical tensor harmonics. A very concise discussion of multipolar expansions can be found in [178], but we'll expand on this as pertains to this dissertation in this Appendix.

B.1 Spin-weighted Spherical Harmonics

In Appendix A we show that most of the Weyl scalars have a non-zero spin. The standard spherical harmonics, though, are spin-zero objects and thus would require coefficients that have spins themselves when expanded on such a basis. It is easier to define a set of spin-weighted spherical harmonics [142] and expand on such a basis instead.

Consider the operator $\eth$ and it's related operator $\overline{\eth}$ which, acting on a function f with spin s, are defined as

$$\eth f := -\sin^s\theta\left(\partial_\theta + \frac{\imath}{\sin\theta}\partial_\varphi\right)\left[f sin^{-s}\theta\right] \tag{B.1}$$

$$\overline{\eth} f := -\sin^{-s}\theta\left(\partial_\theta - \frac{\imath}{\sin\theta}\partial_\varphi\right)\left[f sin^{s}\theta\right] . \tag{B.2}$$

The spin-weighted spherical harmonics [142] are defined in terms of the (spin-zero) spherical harmonics operated on by the spin-lowering and spin-raising operators $\eth$ and $\overline{\eth}$ as

$${}_sY^{\ell,m} := \sqrt{\frac{(\ell-s)!}{(\ell+s)!}}\eth^s\left(Y^{\ell,m}\right) \qquad (0 \le s \le \ell), \tag{B.3a}$$

$$ {}_sY^{\ell,m} \;:=\; (-1)^s \sqrt{\frac{(\ell-s)!}{(\ell+s)!}}\,\overline{\eth}^{\,s}\left(Y^{\ell,m}\right) \qquad (-\ell \le s \le 0) \tag{B.3b} $$

Some basic properties of spin-weighted spherical harmonics.

- As noted in Appendix A, any object η of spin s transforms under a rotation through an angle ψ as $\eta' = e^{-\imath s\psi}\eta$. By taking the complex conjugate of this definition, it is clear that the complex conjugate of η has spin $-s$. With the conjugation properties of the spin-zero spherical harmonics,

$$ {}_s\overline{Y}^{\ell,m} = (-1)^{s+m}\,{}_{-s}Y^{\ell,-m}. \tag{B.4} $$

- The spin-weighted spherical harmonics are an orthonormal basis, satisfying

$$ \oint {}_sY^{\ell,m}(\theta,\varphi)\,{}_{s'}\overline{Y}^{\ell',m'}(\theta,\varphi)\,d\Omega = \delta_{s\,s'}\delta_{\ell\,\ell'}\delta_{m\,m'} \tag{B.5} $$

B.2 Vector Spherical Harmonics

There are times when the quantity one would like to decompose is not a scalar. While our goal is a discussion of tensor spherical harmonics, it is useful to consider first *vector* spherical harmonics, which link the scalar spherical harmonics to a convenient, standard spatial coordinate basis.

For convenience we consider a basis $\boldsymbol{\xi}^m$ related to the standard Cartesian basis as

$$ \boldsymbol{\xi}^0 \;=\; \hat{\boldsymbol{e}}_z\,, \tag{B.6a} $$

$$ \boldsymbol{\xi}^{\pm} \;=\; \frac{\mp 1}{\sqrt{2}}\left(\hat{\boldsymbol{e}}_x \pm \imath\hat{\boldsymbol{e}}_y\right)\,. \tag{B.6b} $$

On this basis, we define the vector spherical harmonic (VSH) in terms of the spin-zero scalar spherical harmonics $Y^{\ell m}$ as

$$ \boldsymbol{Y}^{\ell',\ell m} := \sum_{m'=-\ell'}^{\ell'}\sum_{m''=-1}^{1}\left\langle 1\,\ell'\,m''\,m' \,|\, \ell\,m\right\rangle \boldsymbol{\xi}^{m''}Y^{\ell' m'} \tag{B.7} $$

where $\langle \ell\,\ell'\,m\,m' \,|\, l''\,m''\rangle$ are Clebsch-Gordan coefficients.

Defined in this way, this set of VSHs are *pure-orbital* because they are eigenvectors of the orbital angular momentum operator $\boldsymbol{L}^2 = -r^2\nabla^2 + \partial_r\left(r^2\partial_r\right)$

$$ \boldsymbol{L}^2\boldsymbol{Y}^{\ell',\ell m} = \ell'\left(\ell'+1\right)\boldsymbol{Y}^{\ell',\ell m} \tag{B.8} $$

which is convenient as a basis in solving the vector Laplace equation such as that found in the Bowen-York initial data (Sec. 3.1.2).

There is another set of VSHs, though, which are *pure-spin* VSHs. Denoted as the three vectors ($\boldsymbol{Y}^{E,\ell m}$,

$\boldsymbol{Y}^{B,\ell m}$ and $\boldsymbol{Y}^{R,\ell m}$), they are defined from the spin-zero scalar spherical harmonics as

$$\boldsymbol{Y}^{E,\ell m} \coloneqq \frac{r}{\Lambda}\nabla Y^{\ell m}, \tag{B.9a}$$

$$\boldsymbol{Y}^{B,\ell m} \coloneqq \frac{\imath}{\Lambda}\boldsymbol{L}Y^{\ell m}, \tag{B.9b}$$

$$\boldsymbol{Y}^{R,\ell m} \coloneqq \hat{e}_r Y^{\ell m} \tag{B.9c}$$

where we, for convenience, let $\Lambda = \sqrt{\ell(\ell+1)}$, ∇ is the Euclidean gradient operator and $\boldsymbol{L} \coloneqq \frac{1}{\imath}\boldsymbol{x}\times\nabla$. These harmonics are best seen as being linked to another spatial coordinate basis, $\{\mathfrak{n}, \mathfrak{m}, \overline{\mathfrak{m}}\}$ given by

$$\mathfrak{n} = \hat{e}_r, \tag{B.10a}$$

$$\mathfrak{m} = \frac{1}{\sqrt{2}}\left(\hat{e}_\theta + \imath\hat{e}_\varphi\right), \tag{B.10b}$$

$$\overline{\mathfrak{m}} = \frac{1}{\sqrt{2}}\left(\hat{e}_\theta - \imath\hat{e}_\varphi\right). \tag{B.10c}$$

In this basis, we can relate the pure-spin VSHs to the spin-weighted spherical harmonics as derived by Goldberg *et al.* [91].

$$\boldsymbol{Y}^{E,\ell m} = \frac{1}{\sqrt{2}}\left({}_{-2}Y^{\ell,m}\,\mathfrak{m} - {}_{2}Y^{\ell,m}\,\overline{\mathfrak{m}}\right), \tag{B.11a}$$

$$\boldsymbol{Y}^{B,\ell m} = \frac{-\imath}{\sqrt{2}}\left({}_{-2}Y^{\ell,m}\,\mathfrak{m} + {}_{2}Y^{\ell,m}\,\overline{\mathfrak{m}}\right), \tag{B.11b}$$

$$\boldsymbol{Y}^{R,\ell m} = {}_{0}Y^{\ell,m}\,\mathfrak{n}. \tag{B.11c}$$

B.3 Tensor Spherical Harmonics

Expanding on the idea of vector spherical harmonics, *tensor* spherical harmonics couple the spin-zero scalar spherical harmonics not once, but twice to a coordinate basis. The choices in tensor spherical harmonics (TSHs) has varied frequently over the past forty years as various choices in normalization and orthogonality can be chosen and the obstacle of completeness has been tackled. Out of this came many sets of TSHs: the *pure-orbital* harmonics of Mathews [134], the *pure-spin* harmonics of Zerilli [197], the Regge-Wheeler harmonics [158], and the symmetric tracefree TSHs of Thorne [178]. For the Teukolsky-Nakamura wave solutions, the Mathews-Zerilli [197, 178] basis is used. The TSHs are generally derived for spatial perturbations and thus we will discuss them in that sense. Expansion to full 4-dimensional TSHs encompasses expanding the coordinate bases to four dimensions, which pads the spatial TSHs below with zeroes in the matrix representation and adds supplementary harmonics to perturb what in the '3+1' decomposition is the gauges.

B.3.1 Mathews Tensor Spherical Harmonics

For a spatial set of TSHs, Mathews links the coordinate basis $\boldsymbol{\xi}^m$ to itself in such a way that he attains a set of five symmetric basis tensors, $\boldsymbol{t}^m$ where m ranges from -2 to 2.

$$\boldsymbol{t}^m \coloneqq \sum_{m'=-1}^{1} \sum_{m''=-1}^{1} \left\langle 1\,1\,m'\,m'' \,|\, 2\,m \right\rangle \boldsymbol{\xi}^{m'} \otimes \boldsymbol{\xi}^{m''} \tag{B.12}$$

These basis tensors transform into each other via an irreducible representation of the 2nd order rotation group and are made complete by the related zeroth order representation which happens to be $1/\sqrt{3}$ times the Euclidean identity matrix:

$$\frac{1}{\sqrt{3}}\boldsymbol{\delta} \coloneqq -\sum_{m'=-1}^{1} \sum_{m''=-1}^{1} \left\langle 1\,1\,m'\,m'' \,|\, 0\,0 \right\rangle \boldsymbol{\xi}^{m'} \otimes \boldsymbol{\xi}^{m''}. \tag{B.13}$$

This basis is used by Mathews to create six basic TSHs denoted by $\boldsymbol{T}^{\lambda\,\ell',\,\ell\,m}$ where indicies denote, in the case of Mathews' TSHs, the harmonics such that ℓ' ranges from $\ell-\lambda$ to $\ell+\lambda$. As with the basis tensors $\boldsymbol{t}^m$, there are five such for $\lambda = 2$ and another linked for completeness where $\lambda = 0$. These TSHs are defined in terms of the above coordinate basis as

$$\boldsymbol{T}^{2\,\ell',\,\ell\,m} \coloneqq \sum_{m'=-\ell'}^{\ell'} \sum_{m=-2}^{2} \left\langle \ell'\,2\,m'\,m'' \,|\, \ell\,m \right\rangle Y^{\ell' m} \boldsymbol{t}^{m''}, \tag{B.14a}$$

$$\boldsymbol{T}^{0\,\ell,\,\ell\,m} \coloneqq -Y^{\ell m}\left(\frac{1}{\sqrt{3}}\boldsymbol{\delta}\right). \tag{B.14b}$$

The Mathews harmonics as above is complete (the original paper omits $\boldsymbol{T}^{0\,\ell,\,\ell\,m}$ and as such is not complete, but this is remedied by Thorne in his discussion in [178]. The properties of Mathews TSHs are as follows:

- Under a complex conjugate they transform as

$$\overline{\boldsymbol{T}^{\lambda\,\ell',\,\ell\,m}} = (-1)^{\ell'+\ell+m}\boldsymbol{T}^{\lambda\,\ell',\,\ell\,-m}. \tag{B.15}$$

- They are orthonormal

$$\int \boldsymbol{T}^{\lambda\,\ell,\,L\,M} \cdot \overline{\boldsymbol{T}^{\lambda'\,\ell',\,L'\,M'}}\, d\Omega = \delta_{\lambda\lambda'}\delta_{\ell\ell'}\delta_{LL'}\delta_{MM'} \tag{B.16}$$

  where we use the notation $\boldsymbol{x}\cdot\boldsymbol{y} \coloneqq x^i y_i$ to avoid too many indicies.

- They have parity $\pi = (-1)^{\ell'}$.

- They are eigenstates of the total angular momentum operator, $\boldsymbol{L}^2$

$$\boldsymbol{L}^2 \boldsymbol{T}^{\lambda\,\ell,\,L\,M} = \ell\,(\ell+1)\,\boldsymbol{T}^{\lambda\,\ell,\,L\,M} \tag{B.17}$$

B.3.2 Zerilli Tensor Spherical Harmonics

Just as there are pure-orbital vs pure-spin VSHs, so too are there pure-spin TSHs. These harmonics, denoted now identically as $\boldsymbol{T}^{\lambda\,\ell',\,\ell\,m}$ but with λ no longer indicating the angular momentum order, but chosen from the set L, T, E, B. They are related to the Mathews pure-orbital harmonics via a unitary transformation. It is easiest to consider them in terms of coupling the coordinate basis $\mathfrak{n}, \mathfrak{m}, \overline{\mathfrak{m}}$ to the spin-zero spherical harmonics. Define $[]^S$ as symmetrization of an object and $[]^{STT}$ as symmetrization and taking the transverse-traceless portion of the object. Then the Zerilli TSHs are

$$\boldsymbol{T}^{L\,0,\,\ell\,m} = (\mathfrak{n}\otimes\mathfrak{n})Y^{\ell m}\,, \tag{B.18a}$$

$$\boldsymbol{T}^{T\,0,\,\ell\,m} = \frac{1}{\sqrt{2}}(\boldsymbol{\delta}-\mathfrak{n}\otimes\mathfrak{n})Y^{\ell m}\,, \tag{B.18b}$$

$$\boldsymbol{T}^{E\,1,\,\ell\,m} = \left(\frac{2}{\ell(\ell+1)}\right)^{\frac{1}{2}}\left[\mathfrak{n}\otimes r\nabla Y^{\ell m}\right]^S\,, \tag{B.18c}$$

$$\boldsymbol{T}^{E\,2,\,\ell\,m} = \left(\frac{2(\ell-2)!}{(\ell+2)!}\right)^{\frac{1}{2}}\left[\boldsymbol{L}\boldsymbol{L}Y^{\ell m}\right]^{STT}\,, \tag{B.18d}$$

$$\boldsymbol{T}^{B\,1,\,\ell\,m} = \left(\frac{2}{\ell(\ell+1)}\right)^{\frac{1}{2}}\left[\mathfrak{n}\times\imath\boldsymbol{L}Y^{\ell m}\right]^S\,, \tag{B.18e}$$

$$\boldsymbol{T}^{B\,2,\,\ell\,m} = \left(\frac{2(\ell-2)!}{(\ell+2)!}\right)^{\frac{1}{2}}\left[\imath r\nabla\boldsymbol{L}Y^{\ell m}\right]^{STT} \tag{B.18f}$$

Just as we related the pure-spin VSHs to the spin-weighted spherical harmonics linked to the basis $\mathfrak{n}, \mathfrak{m}, \overline{\mathfrak{m}}$ so can we do so for the Zerilli TSHs.

$$\boldsymbol{T}^{L\,0,\,\ell\,m} = {}_0Y^{\ell,m}(\mathfrak{n}\otimes\mathfrak{n})\,, \tag{B.19a}$$

$$\boldsymbol{T}^{T\,0,\,\ell\,m} = \frac{1}{\sqrt{2}}\,{}_0Y^{\ell,m}(\boldsymbol{\delta}-\mathfrak{n}\otimes\mathfrak{n})\,, \tag{B.19b}$$

$$\boldsymbol{T}^{E\,1,\,\ell\,m} = \left[{}_{-1}Y^{\ell,m}\mathfrak{m}\otimes\mathfrak{n}-{}_1Y^{\ell,m}\overline{\mathfrak{m}}\otimes\mathfrak{n}\right]^S\,, \tag{B.19c}$$

$$\boldsymbol{T}^{E\,2,\,\ell\,m} = \frac{1}{\sqrt{2}}\left[{}_{-2}Y^{\ell,m}\mathfrak{m}\otimes\mathfrak{m}+{}_2Y^{\ell,m}\overline{\mathfrak{m}}\otimes\overline{\mathfrak{m}}\right]\,, \tag{B.19d}$$

$$\boldsymbol{T}^{B\,1,\,\ell\,m} = -\imath\left[{}_{-1}Y^{\ell,m}\mathfrak{m}\otimes\mathfrak{n}+{}_1Y^{\ell,m}\overline{\mathfrak{m}}\otimes\mathfrak{n}\right]^S\,, \tag{B.19e}$$

$$\boldsymbol{T}^{B\,2,\,\ell\,m} = \frac{-\imath}{\sqrt{2}}\left[{}_{-2}Y^{\ell,m}\mathfrak{m}\otimes\mathfrak{m}-{}_2Y^{\ell,m}\overline{\mathfrak{m}}\otimes\overline{\mathfrak{m}}\right] \tag{B.19f}$$

The properties of Zerilli's pure-spin TSHs are as follows

- A complex conjugate operates as

$$\overline{\boldsymbol{T}^{\lambda S,\ell m}} = (-1)^m \boldsymbol{T}^{\lambda S,\ell m} \tag{B.20}$$

- Unlike the version that appears in Zerilli's 1970 paper, the version above is orthonormal and complete under the inner product

$$\int \boldsymbol{T}^{\lambda S,\ell m} \cdot \overline{\boldsymbol{T}^{\lambda' S',\ell' m'}} d\Omega = \delta_{\lambda\lambda'}\delta_{SS'}\delta_{\ell\ell'}\delta_{mm'} \tag{B.21}$$

- These TSHs exhibit two types of parity. The "magnetic"-type TSHs ($\lambda = B$) have parity $\pi = (-1)^{\ell+1}$ while the "electric"-type TSHs ($\lambda \in \{L, T, E\}$) have parity $\pi = (-1)^{\ell}$.

- The TSH $\boldsymbol{T}^{L\,0,\ell m}$ is purely longitudinal (radial), thus having spin 0 like the Newman-Penrose Ψ_2.

- The TSH $\boldsymbol{T}^{T\,0,\ell m}$ is purely transverse but also with spin 0.

- The TSHs $\boldsymbol{T}^{E\,1,\ell m}$ and $\boldsymbol{T}^{B\,1,\ell m}$ are mixed longitudinal and transverse with spin 1 and therefore related to the Newman-Penrose Ψ_3.

- The TSHs $\boldsymbol{T}^{E\,2,\ell m}$ and $\boldsymbol{T}^{B\,2,\ell m}$ are transverse and traceless with spin 2 and therefore related to the Newman-Penrose Ψ_4.

The above pure-spin TSHs are not quite equivalent to Zerilli's TSHs. Zerilli (and therefore Nakamura and Teukolsky in their expansions) use a slightly different basis related to the above by

$$\boldsymbol{a}_{\ell,m} = \boldsymbol{T}^{L\,0,\ell m}, \tag{B.22a}$$
$$\boldsymbol{b}_{\ell,m} = \boldsymbol{T}^{E\,1,\ell m}, \tag{B.22b}$$
$$\boldsymbol{c}_{\ell,m} = -\imath \boldsymbol{T}^{B\,1,\ell m}, \tag{B.22c}$$
$$\boldsymbol{d}_{\ell,m} = -\imath \boldsymbol{T}^{B\,2,\ell m}, \tag{B.22d}$$
$$\boldsymbol{f}_{\ell,m} = \boldsymbol{T}^{E\,2,\ell m}, \tag{B.22e}$$
$$\boldsymbol{g}_{\ell,m} = \boldsymbol{T}^{T\,0,\ell m} \tag{B.22f}$$

B.3.3 Tensor Spherical Harmonics Decomposition

Given a spatial, symmetric tensor with 6 independent components, it can be expanded on a set of 6 TSHs for every (l, m) mode. For a system written in the spatial coordinate basis (r, θ, ϕ) we can expand a general tensor $\boldsymbol{K}$ using Zerilli's pure-spin TSHs. Using Zerilli's notation, this expansion is given as

$$\boldsymbol{K} = \sum_{\ell,m} \left\{ A_{\ell,m}\boldsymbol{a}_{\ell,m} + B_{\ell,m}\boldsymbol{b}_{\ell,m} + Q_{\ell,m}\boldsymbol{c}_{\ell,m} + D_{\ell,m}\boldsymbol{d}_{\ell,m} + F_{\ell,m}\boldsymbol{f}_{\ell,m} + G_{\ell,m}\boldsymbol{g}_{\ell,m} \right\} \tag{B.23}$$

or, in the above notation,

$$\boldsymbol{K} = \sum_{\ell,m} \left\{ A_{\ell,m}\boldsymbol{T}^{L\,0,\,\ell\,m} + B_{\ell,m}\boldsymbol{T}^{E\,1,\,\ell\,m} - \iota Q_{\ell,m}\boldsymbol{T}^{B\,1,\,\ell\,m} - \iota D_{\ell,m}\boldsymbol{T}^{B\,2,\,\ell\,m} + F_{\ell,m}\boldsymbol{T}^{E\,2,\,\ell\,m} + G_{\ell,m}\boldsymbol{T}^{T\,0,\,\ell\,m} \right\} . \tag{B.24}$$

Using the definitions in the previous section, it is convenient to write the matrices representing the above decomposition explicitly in terms of the spin-zero spherical harmonics for the derivation of the TNWs.

The pure longitudinal and pure transverse TSHs are, written explicitly,

$$\boldsymbol{a}_{\ell,m} = \boldsymbol{T}^{L\,0,\,\ell\,m} = \begin{pmatrix} Y^{\ell,m} & 0 & 0 \\ 0 & 0 & 0 \\ 0 & 0 & 0 \end{pmatrix} , \tag{B.25a}$$

$$\boldsymbol{g}_{\ell,m} = \boldsymbol{T}^{T\,0,\,\ell\,m} = \frac{r^2}{\sqrt{2}} \begin{pmatrix} 0 & 0 & 0 \\ 0 & Y^{\ell,m} & 0 \\ 0 & 0 & sin^2\theta Y^{\ell,m} \end{pmatrix} \tag{B.25b}$$

The TSHs with mixed longitude and transverse are

$$\boldsymbol{b}_{\ell,m} = \boldsymbol{T}^{E\,1,\,\ell\,m} = \Lambda r \begin{pmatrix} 0 & \partial_\theta Y^{\ell,m} & \partial_\varphi Y^{\ell,m} \\ * & 0 & 0 \\ * & 0 & 0 \end{pmatrix} , \tag{B.26a}$$

$$\boldsymbol{c}_{\ell,m} = -\iota\boldsymbol{T}^{B\,1,\,\ell\,m} = \iota\Lambda r \begin{pmatrix} 0 & csc\theta Y^{\ell,m}_{,\phi} & -sin\theta Y^{\ell,m}_{,\theta} \\ * & 0 & 0 \\ * & 0 & 0 \end{pmatrix} . \tag{B.26b}$$

where we conveniently let $\Lambda := (\sqrt{2\ell(\ell+1)})^{-\frac{1}{2}}$.

The remaining two TSHs are those that are transverse-traceless, written explicitly as

$$\boldsymbol{f}_{\ell,m} = \boldsymbol{T}^{E\,2,\,\ell\,m} = \frac{\Lambda r^2}{\sqrt{(\ell-1)(\ell+2)}} \begin{pmatrix} 0 & 0 & 0 \\ 0 & W^{\ell,m} & X^{\ell,m} \\ 0 & * & -sin^2\theta W^{\ell,m} \end{pmatrix} , \tag{B.27a}$$

$$\boldsymbol{d}_{\ell,m} = -\iota\boldsymbol{T}^{B\,2,\,\ell\,m} = \frac{-\iota\Lambda r^2}{\sqrt{(\ell-1)(\ell+2)}} \begin{pmatrix} 0 & 0 & 0 \\ 0 & -csc\theta X^{\ell,m} & sin\theta W^{\ell,m} \\ 0 & * & sin\theta X^{\ell,m} \end{pmatrix} \tag{B.27b}$$

where we introduce two new angular functions, $W^{\ell,m}$ and $X^{\ell,m}$, given by

$$W^{\ell,m} := \left(\partial_\theta^2 - \cot\theta\partial_\theta - \frac{1}{\sin^2\theta}\partial_\varphi^2 \right) Y^{\ell,m} , \tag{B.28}$$

$$X^{\ell,m} \quad := \quad 2\partial_\varphi \left(\partial_\theta - \cot\theta\right) Y^{\ell,m}. \tag{B.29}$$

Appendix C

Teukolsky-Nakamura Waves

Given a spacetime such as a binary black hole system, we could add gravitational radiation through a Brill wave [47], a solution to the fully-nonlinear Einstein equations. Unfortunately the Brill wave is difficult to interpret and control. We find it convenient to work instead with Teukolsky-Nakamura waves [174, 140, 166], a solution to the linearized Einstein equations. These gravitational waves, used in perturbing the initial spacetime of Ch. 4, are discussed and derived in this Appendix.

The linearized Einstein equations is the canonical starting point for deriving gravitational waves [184]. It is insightful to consider the metric perturbation that solves the linearized Einstein equations on a convenient basis, namely the tensor spherical harmonics. It was not until 1982 that such a solution was explicitly written out for the $\ell = 2$ modes of a TT perturbation on a spherical coordinate basis, call Teukolsky waves [174]. Teukolsky waves were useful in testing codes in a weak yet dynamic regime, but their use is limited in full non-linear numerical relativity. An alternative was an approach by Nakamura [140, 166] which not only solved the linearized Einstein equation on the tensor spherical harmonics basis for general (ℓ, m) modes, but also chose an initially conformally flat spatial metric, leaving the entire perturbation in the extrinsic curvature.

C.1 Metric Perturbation

Consider a perturbation of the metric, $\mathfrak{h}_{\alpha\beta}$

$$g_{\alpha\beta} = g^{(0)}_{\alpha\beta} + \mathfrak{h}_{\alpha\beta} \tag{C.1}$$

where $g^{(0)}_{\alpha\beta}$ is the background metric which we choose, for simplicity, to be Minkowskian flat space $\delta_{\alpha\beta}$. As we are looking for gravitational waves, we consider a transverse-traceless perturbation. That is, we consider

only spatial perturbations which satisfy

$$\nabla_\alpha \mathfrak{h}^\alpha_\beta = 0 \tag{C.2a}$$

$$\delta^{\alpha\beta}\mathfrak{h}_{\alpha\beta} = 0 \tag{C.2b}$$

where ∇_μ is the covariant derivative in terms of the background metric $\delta_{\alpha\beta}$. With the requirements of Eq. C.2a and the spatial nature of the perturbation, there are only two degrees of freedom corresponding to the two polarizations of gravitational radiation, h_+ and $h_\times$.

As we're considering this for initial data only, let us speak in the framework of the ADM formalism where we choose our shift to vanish and we assume a vacuum spacetime. With these assumptions, the evolution equations (Eq. 2.11 and Eq. 2.12) simplify to

$$\partial_t \gamma_{ij} = -2\alpha K_{ij}\,, \tag{C.3}$$

$$\partial_t K_{ij} = -\breve{\nabla}_i\breve{\nabla}_j\alpha + \alpha\mathcal{R}_{ij} + \alpha K K_{ij} - 2\alpha K_{ik}K^k_{\ j} \tag{C.4}$$

The constraint equations (Eq. 2.8 and Eq. 2.9) simplify to

$$\mathbb{C}_H = \mathcal{R} + K^2 - K^{ij}K_{ij}\,, \tag{C.5}$$

$$\mathbb{M}_i = \breve{\nabla}_j K^j_i - \breve{\nabla}_i K. \tag{C.6}$$

The evolution equation for γ_{ij} can be written in terms of the metric perturbation

$$K_{ij} = -\frac{1}{2\alpha}\partial_t \mathfrak{h}_{ij}. \tag{C.7}$$

Similarly, taking the trace of the evolution equation for K_{ij} and assuming $\mathbb{C}_H$ vanishes,

$$\partial_t K = -\breve{\nabla}^2\alpha - K_{ik}K^k_{\ j} \tag{C.8}$$

which, since K_{ij} is first order in $\mathfrak{h}_{ij}$, is second order in $\mathfrak{h}_{ij}$. We will only consider terms first order in the metric perturbation, so in this case $\partial_t K \simeq -\breve{\nabla}^2\alpha$.

Let us assume at this point we take $\alpha = 1$, which is approximately accurate far from any BH. Then $\partial_t K = 0$ to first order in $\mathfrak{h}$ and, assuming we start with maximal slicing ($K = 0$), the trace always vanishes. In this case the momentum constraint, assuming it is satisfied, reduces to

$$\breve{\nabla}_j K^j_i = 0. \tag{C.9}$$

Since $K = 0$, the trace of Eq. C.7 yields $\partial_t \mathfrak{h}^k_k = 0$. Similarly, applying Eq. C.7 into Eq. C.9 yields $\partial_t\left(\breve{\nabla}^k\mathfrak{h}_{ik}\right) = 0$. Thus, choosing the trace and transverse portions to vanish initially nails the perturbation to

be transverse-traceless.

We also note that, to first order in this spatial perturbation, the Ricci tensor is

$$\mathcal{R}_{ij} = \frac{1}{2}\left(-\breve{\nabla}_i\breve{\nabla}_j\mathfrak{h}^k_k + \breve{\nabla}^k\breve{\nabla}_j\mathfrak{h}_{ik} + \breve{\nabla}^k\breve{\nabla}_i\mathfrak{h}_{jk} - \breve{\nabla}^k\breve{\nabla}_k\mathfrak{h}_{ij}\right). \tag{C.10}$$

We now assume, additionally, that the background metric is flat so the covariant derivates commute. With this assumption and vanishing trace and transverse portions of the perturbation, the first three terms in the Ricci vanish, leaving

$$\mathcal{R}_{ij} = -\frac{1}{2}\breve{\nabla}^k\breve{\nabla}_k\mathfrak{h}_{ij}. \tag{C.11}$$

The evolution equation for the extrinsic curvature under these assumptions reduces to

$$\partial_t K_{ij} = -\frac{1}{2}\breve{\nabla}^k\breve{\nabla}_k\mathfrak{h}_{ij}. \tag{C.12}$$

Combining this with Eq. C.7,

$$\partial_t^2 K_{ij} = \breve{\nabla}^k\breve{\nabla}_k K_{ij}. \tag{C.13}$$

In constructing our initial data, we set the actual oscillating metric perturbation $\mathfrak{h}_{ij}$ to vanish on the initial hypersurface. This does not, as the above shows, mean that the extrinsic curvature vanishes. If we choose our K_{ij} such that its trace K vanishes and both Equations C.9 and C.13 are satisfied, we will find ourselves with a gravitational wave. To do this, we expand the extrinsic curvature in terms of the TSHs of Sec. B.3.3.

C.2 Expansion of K_{ij}

In the linear spatial perturbation described above, we consider the expansion of the extrinsic curvature in terms of the Zerilli pure-spin TSHs.

$$\boldsymbol{K} = \sum_{\ell,m}\left\{\mathcal{A}_{\ell,m}\boldsymbol{T}^{L\,0,\ell\,m} + \mathcal{B}_{\ell,m}\boldsymbol{T}^{E\,1,\ell\,m} - \imath\mathcal{Q}_{\ell,m}\boldsymbol{T}^{B\,1,\ell\,m} - \imath\mathcal{D}_{\ell,m}\boldsymbol{T}^{B\,2,\ell\,m} + \mathcal{F}_{\ell,m}\boldsymbol{T}^{E\,2,\ell\,m} + \mathcal{G}_{\ell,m}\boldsymbol{T}^{T\,0,\ell\,m}\right\}. \tag{C.14}$$

First let us consider the trace. Using the explicitly written out TSHs in the previous appendix,

$$K = \mathcal{A}_{\ell,m} + \frac{2}{r^2}\mathcal{G}_{\ell,m} = 0. \tag{C.15}$$

so we have one less coefficient to solve for.

Eq. C.9 yields three constraint equations, while Eq. C.13 yields five second-order coupled differential equations for the expansion coefficients. If we consider only even parity modes, both $\mathcal{Q}_{\ell,m}$ and $\mathcal{D}_{\ell,m}$ must both vanish as they are coefficients to the magnetic-type parity TSHs. We can now decouple a differential

equation for $\mathcal{A}$ whose general solution is given by

$$\mathcal{A}_{\ell,m} = r^{\ell-2}\left(\frac{1}{r}\partial_r\right)^{\ell}\frac{\mathcal{P}^i_{\ell,m}(t-r)+\mathcal{P}^o_{\ell,m}(t+r)}{r} \tag{C.16}$$

where $\mathcal{P}^i_{\ell,m}(t-r)$ and $\mathcal{P}^o_{\ell,m}(t+r)$ are arbitrary functions which describe the radial dependence of ingoing and outgoing waves respectively. With this coefficient, the rest of the equations fall apart.

Absorbing the extra factors of r and ℓ into the TSH coefficients, we find the solution given in Chapter 4:

$$A_{ij} = \sum_{\ell,m}\begin{pmatrix} \mathcal{A}_{\ell,m}Y^{\ell,m} & \mathcal{B}_{\ell,m}Y^{\ell,m}_{\theta} & \mathcal{B}_{\ell,m}Y^{\ell,m}_{\varphi} \\ * & \mathcal{G}_{\ell,m}Y^{\ell,m}+\mathcal{F}_{\ell,m}W^{\ell,m} & \mathcal{F}_{\ell,m}X^{\ell,m} \\ * & * & (\mathcal{G}_{\ell,m}Y^{\ell,m}-\mathcal{F}_{\ell,m}W^{\ell,m})\sin^2\theta \end{pmatrix} \tag{C.17}$$

where the coefficients $\mathcal{A}_{\ell,m}$, $\mathcal{B}_{\ell,m}$, $\mathcal{F}_{\ell,m}$, and $\mathcal{G}_{\ell,m}$ are functions only of the coordinate radius and time r, t as follows

$$\mathcal{A}_{\ell,m} = r^{\ell-2}\left(\frac{1}{r}\partial_r\right)^{\ell}\frac{\mathcal{P}^i_{\ell,m}(t-r)+\mathcal{P}^o_{\ell,m}(t+r)}{r}, \tag{C.18a}$$

$$\mathcal{B}_{\ell,m} = \frac{1}{\ell(\ell+1)r}\partial_r(r^3\mathcal{A}_{\ell,m}), \tag{C.18b}$$

$$\mathcal{G}_{\ell,m} = -\frac{r^2}{2}\mathcal{A}_{\ell,m}, \tag{C.18c}$$

$$\mathcal{F}_{\ell,m} = \frac{1}{(\ell-2)(\ell+1)}\left[\mathcal{G}_{\ell,m}+\partial_r\left(\frac{r}{\ell(\ell+1)}\partial_r(r^3\mathcal{A}_{\ell,m})\right)\right] \tag{C.18d}$$

Appendix D

Tools for Coupled Hydrodynamic Simulations

In this appendix we will discuss the various parts of a hydrodynamic code in detail. For this Appendix we drop the subscript $_o$ from ρ_o to avoid clutter in the equations.

D.1 Reconstruction: Piecewise Parabolic Method (PPM)

The PPM reconstruction technique [62], as applied in our code, involves four steps:

- Interpolate each variable to the cell boundary using a quadratic polynomial, setting the variables on both sides of the boundary as equivalent at first.
- If desired, see if there is a contact discontinuity in the cell and sharpen it.
- If desired, add artificial viscosity.
- Preserve monotonicity by making replacements of one side's variable, if necessary.

We assume the variable q is a scalar function of x, the dimension we are reconstructing along, and interpolate a quadratic polynomial to the cell boundary.

$$q_{i+1/2} = \frac{1}{2}(q_{i+1} + q_i) + \frac{1}{6}(\delta_m q_i - \delta_m q_{i+1}) \tag{D.1}$$

where

$$\delta_m q_i = \begin{cases} \text{sign}(\delta q_i)\min(|\delta q_i|, 2|q_{i+1} - q_i|, 2|q_i - q_{i-1}|) & \text{if}(q_{i+1} - q_i)(q_i - q_{i-1}) > 0 \\ 0 & \text{otherwise} \end{cases} \tag{D.2}$$

$$\delta q_i = \frac{1}{2}(q_{i+1} - q_{i-1}) \tag{D.3}$$

Initially we set the variable value on both the left and right of the cell interface as equivalent

$$q_i^R = q_{i+1}^L = q_{i+1/2}. \tag{D.4}$$

Discontinuities which are primarily contact discontinuities can be treated differently. We can detect whether a contact discontinuity exists in the cell by checking whether the following condition is satisfied

$$K_0 \frac{|\rho_{i+1} - \rho_{i-1}|}{\min(\rho_{i+1}, \rho_{i-1})} \geq \frac{|P_{i+1} - P_{i-1}|}{\min(P_{i+1}, P_{i-1})} \tag{D.5}$$

where K_0 is a user-specified, problem-specific constant to control the sensitivity of the shock detection. If this condition is satisfied, we apply the steepening to the *density* variable only. We start by defining the quantity η as

$$\eta = \max(0, \min(1, \eta_1(\tilde{\eta} - \eta_2))) \tag{D.6}$$

where η_1 and η_2 are user-specified positive constants. Given

$$\delta^2 \rho_i = \frac{\rho_{i+1} - 2\rho_i + \rho_{i-1}}{6\Delta x^2}, \tag{D.7}$$

the quantity $\tilde{\eta}$ is

$$\tilde{\eta} = \begin{cases} \frac{\rho_{i-2} - \rho_{i+2} + 4\delta\rho_i}{12\delta\rho_i} & \text{if } \left\{ \delta^2\rho_{i+1}\delta^2\rho_{i-1} < 0\,, (\rho_{i+1} - \rho_{i-1}) - \epsilon_p \min(|\rho_{i+1}|, |\rho_{i-1}|) > 0 \right\} \\ 0 & \text{otherwise} \end{cases}. \tag{D.8}$$

With η determined, the density to the left and right of the boundaries is modified as

$$\rho_{i+1}^L \rightarrow \rho_{i+1}^L(1 - \eta) + \left(\rho_i + \frac{1}{2}\delta_m \rho_i\right)\eta, \tag{D.9a}$$

$$\rho_i^R \rightarrow \rho_i^R(1 - \eta) + \left(\rho_{i+1} - \frac{1}{2}\delta_m \rho_{i+1}\right)\eta \tag{D.9b}$$

Thus, shock detection and sharpening depends on four user-defined parameters: ϵ_p and K_0 define how a contact discontinuity is detected while η_1 and η_2 determine to what extent the shock is sharpened.

The PPM also includes the option to flatten the zone structure near shocks by adding simple dissipation. From two user-specified parameters ω_1 and ω_2, we define a flattening parameter

$$\nu_i = \begin{cases} \max\left(0, 1 - \omega_2 \max\left(0, \left(\frac{P_{i+1} - P_{i-1}}{P_{i+2} - P_{i-2}} - \omega_1\right)\right)\right) & \text{if } \epsilon_p \min(P_{i-1}, P_{i+1}) < |P_{i+1} - P_{i-1}|, v_{i-1}^x - v_{i+1}^x > 0 \\ 1 & \text{otherwise} \end{cases} \tag{D.10}$$

The flattening is then accomplished by the transformation

$$q_i^{L,R} \to \nu_i q_i^{L,R} + (1-\nu_i) q_i. \tag{D.11}$$

This differs from the flattening in Colella and Woodward [62] by its adaptation to stencils with three points and and ν_i is further modified

$$\nu_i \to \max\left(\nu_i, \nu_{i+\mathrm{sign}(P_{i-1}-P_{i+1})}\right). \tag{D.12}$$

In the final step, we avoid oscillatory behavior by making the following replacements to preserve monotonicity:

$$q_{i+1}^L \to q_i^R = q_i \qquad \text{if} \qquad (q_i^R - q_i)(q_i - q_{i+1}^L) \le 0 \tag{D.13a}$$

$$q_{i+1}^L \to 3q_i - 2q_i^R \qquad \text{if} \qquad (q_i^R - q_{i+1}^L)\left(q_i - \frac{1}{2}(q_{i+1}^L + q_i^R\right) > \frac{1}{6}(q_i^R - q_{i+1}^L)^2 \tag{D.13b}$$

$$q_i^R \to 3q_i - 2q_{i+1}^L \qquad \text{if} \qquad (q_i^R - q_{i+1}^L)\left(q_i - \frac{1}{2}(q_{i+1}^L + q_i^R\right) < \frac{1}{6}(q_i^R - q_{i+1}^L)^2 \tag{D.13c}$$

The PPM then gives us the set of conservative and primitive variables on both sides of a cell interface which we can use to set up a Riemann problem. For more detail, see Appendix D.

D.2 Riemann Solver: Modified Marquina

For our work we use an approximate Riemann solver, the Marquina solver, derived first by Donat and Marquina [70], modified by Aloy *et al.* [8] and extended to general relativity by Frieben, Ibáñez and Pons. We consider the linearized Riemann problem in one dimension

$$\partial_t C + \partial_{x^i} \mathcal{F}^{(i)} = 0 \tag{D.14}$$

across a discontinuity at $x^1 = 0$ so the solution are self-similar in terms of the variable $\xi := x^i/t$. The Marquina solver only finds the flux along the $\xi = 0$ characteristic ray.

We calculate the eigenvalues $\lambda_i(C)$ and left and right eigenvectors, $\mathfrak{l}_i(C)$ and $\mathfrak{r}_i(C)$ respectively, of the Jacobian matrix $\mathcal{B} := \alpha \frac{\partial \mathcal{F}}{\partial C}$. The eigenvalues of this Jacobian define the material and acoustic waves in this direction. The material waves are determined by the triple eigenvector

$$\lambda_o = \alpha v^x - \beta^x. \tag{D.15}$$

The remaining two eigenvectors $\lambda_\pm$ define the two acoustic waves given in terms of the local sound velocity c_s found through

$$h c_s^2 = \left.\frac{\partial P}{\partial \rho_o}\right|_\epsilon + \frac{P}{\rho_o^2}\left.\frac{\partial P}{\partial \epsilon}\right|_{\rho_o}. \tag{D.16}$$

These acoustic eigenvectors are

$$\lambda_{\pm} = \frac{\alpha}{1 - v^2 c_s^2} \left\{ v^x (1 - c_s^2) \pm c_s \sqrt{(1 - v^2)[\gamma^{xx}(1 - v^2 c_s^2) - (v^x)^2 (1 - c_s^2)]} \right\} - \beta^x. \tag{D.17}$$

Corresponding left and right eigenvectors can be analytically calculated as well and can be found, for example, in [70].

With this decomposition in hand, we define characteristic variables and fluxes which simplify the solution to the problem:

$$\mathfrak{w}_i^{L,R} := \mathfrak{l}_i(C^{L,R}) \cdot C^{L,R} \tag{D.18a}$$

$$\mathfrak{f}_i^{L,R} := \mathfrak{l}_i(C^{L,R}) \cdot \mathcal{F}^{L,R} \tag{D.18b}$$

Depending on the relative sign of the left and right eigenvalues, the characteristic fluxes $\mathfrak{f}_{\pm}^i$ are set. If $\lambda_i(C^{L,R})$ are of the same sign,

$$\{\mathfrak{f}_+^i, \mathfrak{f}_-^i\} = \begin{cases} \{\mathfrak{f}_L^i, 0\} & \text{if } \lambda_i(C^L) > 0 \\ \{0, \mathfrak{f}_R^i\} & \text{otherwise} \end{cases} . \tag{D.19}$$

If the sign of the eigenvalue λ_i changes across the cell boundary, we instead calculate a Lax-Friedrichs type flux given by

$$\mathfrak{f}_+^i = \frac{1}{2}\left(\mathfrak{f}_L^i + \Lambda^i \mathfrak{w}_L^i\right) \tag{D.20a}$$

$$\mathfrak{f}_-^i = \frac{1}{2}\left(\mathfrak{f}_R^i - \Lambda^i \mathfrak{w}_R^i\right) \tag{D.20b}$$

where $\Lambda^i = \max(|\lambda_i(C^L), \lambda_i(C^R)|)$. The characteristic fluxes denote the part of the approximate Riemann solution we use for the matter evolution.

Before we can compute the Marquina flux across the cell boundary, consider the form of the conservation equation in terms of the characteristic variables $\mathfrak{w}$ defined in Eq. D.18b. Eq. D.14 can then be rewritten as

$$\partial_t \mathfrak{w} + \Lambda \partial_x \mathfrak{w} = 0 \tag{D.21}$$

where Λ is the diagonal matrix of eigenvalues. Each characteristic variable then obeys the linear advection equation with velocity λ_i, easing our efforts in solving the Riemann problem. We can write the solution in terms of the characteristic variables and the discontinuity of the characteristic variables across the discontinuity,

$$\Delta\mathfrak{w} := \mathfrak{w}_L - \mathfrak{w}_R = \mathfrak{l} \cdot (C_L - C_R). \tag{D.22}$$

We reorder the variables such that the corresponding eigenvalues are sorted by magnitude $\lambda_1 \leq ... \leq \lambda_N$.

Defining $\left(e^j\right)_i \coloneqq \delta_i^j$, we can solve the Riemann problem in terms of the characteristic variable on the left

$$\mathfrak{w} = (\mathfrak{w})_L + \sum_{j=1}^{M} \Delta\mathfrak{w}_j e^j \tag{D.23}$$

where the similarity variable ξ lies between the λ_M and λ_{M+1}, or in terms of the characteristic variable on the right

$$\mathfrak{w} = (\mathfrak{w})_R - \sum_{j=M+1}^{N} \Delta\mathfrak{w}_j e^j. \tag{D.24}$$

Desiring the best of both worlds, we average these two solutions

$$\mathfrak{w} = \frac{1}{2}\left(\mathfrak{w}_L + \mathfrak{w}_R + \sum_{j=1}^{M} \Delta\mathfrak{w}_j e^j - \sum_{j=M+1}^{N} \Delta\mathfrak{w}_j e^j\right) \tag{D.25}$$

which can be rewritten in terms of the actual conserved variables by operating the solution on the right eigenvector $\mathfrak{r}^i$ to obtain the solution

$$\boldsymbol{C} = \frac{1}{2}\left(\boldsymbol{C}_L + \boldsymbol{C}_R + \sum_{j=1}^{M} \Delta\mathfrak{w}_j \mathfrak{r}^j - \sum_{j=M+1}^{N} \Delta\mathfrak{w}_j \mathfrak{r}^j\right). \tag{D.26}$$

Given the conserved variables which approximately solve the Riemann problem, we note that our goal in solving the Riemann problem is to calculate the *flux* across the cell boundary. From Eq. 6.9 we have the analytic expression of the fluxes in terms of the conservative and primitive variables. By converting the above derived conservative variables to primitives we have all the information necessary to calculate the flux. Here we simplify in that we consider only the flux along the characteristic $\xi = 0$, yielding a simple flux calculation

$$\mathcal{F}(\boldsymbol{C}) = \frac{1}{2}\left(\mathcal{F}(\boldsymbol{C}_L) + \mathcal{F}(\boldsymbol{C}_L) - \sum_{i=1}^{N} |\lambda_i| \Delta\mathfrak{w}_i \mathfrak{r}^i\right)\,. \tag{D.27}$$

The actual flux used in Eq. 6.14 is

$$\hat{\mathcal{F}} = \frac{1}{2}(\mathfrak{f}_- \cdot \mathfrak{r}_- + \mathfrak{f}_+ \cdot \mathfrak{r}_+ + \mathfrak{Q}). \tag{D.28}$$

where $\mathfrak{Q}$ is the correction due to the characteristic conservative jumps

$$\mathfrak{Q} \coloneqq \sum_{i=1}^{N} |\lambda_i| \left(\Delta\mathfrak{w}_L \mathfrak{r}_L - \Delta\mathfrak{w}_R \mathfrak{r}_R\right)) \tag{D.29}$$

D.3 Recovery of Primitives

While we evolve the conserved variables $C = \{D, S_i, \tau\}$, they are not convenient for analyzing the system. Instead, we cover the set of primitive variables $\{\rho_o, v^i, \epsilon\}$ together with the derived quantities of pressure $P = P(\rho_o, \epsilon)$ and the Lorentz factor $W = (1 - v^i v_i)^{-1/2}$. There are two types of recovery methods depending on the type of equation of state. For both methods we work with the "undensitized" conserved variables $\check{C}$ defined by dividing by the square-root of the spatial metric, $\sqrt{\gamma}$. We choose a constraint, $f = 0$, and use a Newton-Raphson type iteration until this is satisfied.

D.3.1 Polytropic Equation of State

The polytropic equation of state $P(\rho_o) = \kappa\rho_o^\Gamma$ is a special form of the ideal gas equation of state $P(\rho_o, \epsilon) = (\Gamma - 1)\rho_o\epsilon$ where the internal energy can be directly related to the pressure and rest-mass density as

$$\epsilon = \frac{\kappa\rho_o^{\Gamma-1}}{\Gamma - 1}. \tag{D.30}$$

In this case, the constraint we iterate towards satisfying is derived from the definition of the undensitized conserved energy:

$$f = \tilde{\rho}_o\tilde{W} - \check{D} \tag{D.31}$$

where we start from a reasonable guess for the rest-mass density $\tilde{\rho_o}$. With the equation of state known, the specific enthalpy for this guess simplifies to

$$\tilde{h} = 1 + \frac{\Gamma\kappa\tilde{\rho}_o}{\Gamma - 1} \tag{D.32}$$

From the requirement that $u_\mu u^\mu = -1$ we can find the Lorentz factor in terms of the updated conserved variables and the guess for the rest-mass density to be

$$\tilde{W} = \sqrt{1 + \frac{S^2}{(\check{D}\tilde{h})^2}}. \tag{D.33}$$

As $\tilde{W}$ is directly related to $\tilde{h}$, it is easiest to write the derivative of the constraint f in terms of the derivative of $\tilde{h}$ as our guess for the ρ_o changes

$$f' = \tilde{W} - \frac{\tilde{\rho}_o S^2}{\tilde{W}\check{D}^2\tilde{h}^3}\tilde{h}' \tag{D.34}$$

where

$$\tilde{h}' = \frac{1}{\tilde{\rho}_o}\frac{\partial P}{\partial \rho} \tag{D.35}$$

D.3.2 General Equation of State

For a general equation of state $P = P(\rho_o, \epsilon)$, we choose this the equation of state itself as the constraint to satisfy:

$$f = \tilde{P} - P(\tilde{\rho}_o, \tilde{\epsilon}). \tag{D.36}$$

Given an initial guess for the pressure $\tilde{P}$, we find the resulting guesses for the rest-mass density, Lorentz factor, and internal energy from the new conserved variables

$$\tilde{\rho}_o = \frac{\check{D}}{\aleph}\sqrt{\aleph^2 - S^2} \tag{D.37a}$$

$$\tilde{W} = \frac{\aleph}{\sqrt{\aleph^2 - S^2}} \tag{D.37b}$$

$$\tilde{\epsilon} = \frac{\sqrt{\aleph^2 - S^2} - \tilde{P}\tilde{W} - \tilde{D}}{\check{D}} \tag{D.37c}$$

where $\aleph := \check{\tau} + \check{D} + \tilde{P}$ and $S^2 := \gamma^{ij}\check{S}_i\check{S}_j$.

For the Newton-Raphson iteration, the derivative of the constraint f is given in terms of the guessed parameters of the equation of state

$$f' = 1 - \frac{\partial P}{\partial \rho_o}\frac{\partial \rho_o}{\partial P} - \frac{\partial P}{\partial \epsilon}\frac{\partial \epsilon}{\partial P} \tag{D.38}$$

where $\frac{\partial P}{\partial \rho_o}$ and $\frac{\partial P}{\partial \epsilon}$ are derived from the equation of state. The other derivatives are found in terms of conserved variables as

$$\frac{\partial \rho_o}{\partial P} = \frac{\check{D}S^2}{\aleph^2\sqrt{\aleph^2 - S^2}} \tag{D.39a}$$

$$\frac{\partial \epsilon}{\partial P} = \frac{\tilde{P}S^2}{\tilde{\rho}_o\aleph\left(\aleph^2 - S^2\right)}. \tag{D.39b}$$

Bibliography

[1] Cactus computational toolkit home page. Http://www.cactuscode.org/, URL http://www.cactuscode.org/.

[2] Mesh refinement with carpet. Http://www.carpetcode.org/, URL http://www.carpetcode.org/.

[3] *Vector and Parallel Processing –VECPAR'2002, 5th International Conference*. Springer, Berlin (2003). URL http://www.cactuscode.org/Publications/.

[4] O. Agertz, B. Moore, J. Stadel, D. Potter, F. Miniati, J. Read, L. Mayer, A. Gawryszczak, A. Kravtsov, J. Monaghan, A. Nordlund, F. Pearce, V. Quilis, D. Rudd, V. Springel, J. Stone, E. Tasker, R. Teyssier, J. Wadsley, and R. Walder. Fundamental differences between sph and grid methods. *Mon. Not. Roy. Astron. Soc.*, 380:963 (2007). astro-ph/0610051.

[5] P. Ajith and S. Bose. Estimating the parameters of non-spinning binary black holes using ground-based gravitational-wave detectors: Statistical errors (2009). 0901.4936.

[6] M. Alcubierre, G. Allen, B. Brügmann, E. Seidel, and W.-M. Suen. Towards an understanding of the stability properties of the 3+1 evolution equations in general relativity. *Phys. Rev. D*, 62:124011 (2000). gr-qc/9908079.

[7] M. Alcubierre, B. Brügmann, P. Diener, M. Koppitz, D. Pollney, E. Seidel, and R. Takahashi. Gauge conditions for long-term numerical black hole evolutions without excision. *Phys. Rev. D*, 67:084023 (2003). gr-qc/0206072.

[8] M. A. Aloy, J. M. Ibáñez, J. M. Martí, and E. Müller. Genesis: A high-resolution code for 3d relativistic hydrodynamics. *ApJ*, 122:S151 (1999). astro-ph/9903352.

[9] K. Alvi. Approximate binary-black-hole metric. *Phys. Rev. D*, 61:124013 (2000).

[10] P. Amaro-Seoane, C. Miller, and M. Freitag. Gravitational waves from eccentric intermediate-mass black hole binaries. *ApJ*, 692:L50 (2009). arXiv:0901.0604.

[11] A. Anile. *Relativistic fluids and magneto-fluids: with applications in astrophysics and plasma physics*. Cambridge University Press, New York, NY (1989).

[12] P. Anninos and P. C. Fragile. Non-oscillatory central difference and artificial viscosity schemes for relativistic hydrodynamics. *ApJ*, 144:S243 (2003). astro-ph/0206265.

[13] M. Ansorg, B. Brügmann, and W. Tichy. A single-domain spectral method for black hole puncture data. *Phys. Rev. D*, 70:064011 (2004). gr-qc/0404056.

[14] P. J. Armitage and P. Natarajan. Accretion during the merger of supermassive black holes. *ApJ*, 567(1):L9 (2002). URL http://stacks.iop.org/1538-4357/567/L9.

[15] P. J. Armitage and P. Natarajan. Eccentricity of supermassive black hole binaries coalescing from gas rich mergers. *ApJ*, 634:921 (2005). astro-ph/0508493.

[16] R. Arnowitt, S. Deser, and C. W. Misner. *Gravitation: An Introduction to Current Research*. Wiley (1962).

[17] A. Ashtekar, C. Beetle, and S. Fairhurst. Isolated horizons: A generalization of black hole mechanics. *Class. Quant. Grav.*, 16:L1 (1999). gr-qc/9812065.

[18] A. Ashtekar and B. Krishnan. Dynamical horizons: Energy, angular momentum, fluxes and balance laws. *Phys. Rev. Lett.*, 89:261101 (2002). gr-qc/0207080.

[19] A. Ashtekar and B. Krishnan. Dynamical horizons and their properties. *Phys. Rev. D*, 68:104030 (2003). gr-qc/0308033.

[20] A. Ashtekar and B. Krishnan. Isolated and dynamical horizons and their applications. *Living Rev. Rel.*, 7:10 (2004).

[21] B. Aylott et al. Testing gravitational-wave searches with numerical relativity waveforms: Results from the first numerical injection analysis (ninja) project (2009). arXiv:0901.4399.

[22] L. Baiotti, I. Hawke, P. J. Montero, and L. Rezzolla. A new three-dimensional general-relativistic hydrodynamics code. *Mem. del. Soc. Ast. It. Sup.*, 1:210 (2003).

[23] J. Baker, J. Centrella, D. Choi, M. Koppitz, J. van Meter, and M. Miller. Getting a kick out of numerical relativity. *ApJ*, 653:L93 (2006). astro-ph/0603204.

[24] J. G. Baker, M. Campanelli, and C. O. Lousto. The lazarus project: A pragmatic approach to binary black hole evolutions. *Phys. Rev. D*, 65:044001 (2002). gr-qc/0104063.

[25] J. G. Baker, M. Campanelli, F. Pretorius, and Y. Zlochower. Comparisons of binary black hole merger waveforms. *Class. Quant. Grav.*, 24:S25 (2007). gr-qc/0701016.

[26] J. G. Baker, J. Centrella, D.-I. Choi, M. Koppitz, and J. van Meter. Binary black hole merger dynamics and waveforms. *Phys. Rev. D*, 73:104002 (2006). gr-qc/0602026.

[27] J. G. Baker, J. Centrella, D.-I. Choi, M. Koppitz, and J. van Meter. Gravitational wave extraction from an inspiraling configuration of merging black holes. *Phys. Rev. Lett.*, 96:111102 (2006). gr-qc/0511103.

[28] J. G. Baker, J. R. van Meter, S. T. McWilliams, J. Centrella, and B. J. Kelly. Consistency of post-newtonian waveforms with numerical relativity. *Phys. Rev. Lett.*, 99:181101 (2007). gr-qc/0612024.

[29] F. Banyuls, J. Font, J. Ibáñez, J. Martí, and J. Miralles. Numerical {3+1} general relativistic hydrodynamics: A local characteristic approach. *ApJ*, 476:221 (1997).

[30] T. W. Baumgarte and S. L. Shapiro. On the numerical integration of einstein's field equations. *Phys. Rev. D*, 59:024007 (1999). gr-qc/9810065.

[31] T. W. Baumgarte and S. L. Shapiro. Numerical relativity and compact binaries. *Phys. Rept.*, 376(2):41 (2003). gr-qc/0211028.

[32] M. Begelman, R. Blandford, and M. Rees. Massive black hole binaries in active galactic nuclei. *Nature*, 287:307 (1980).

[33] K. Belczynski, M. Benacquista, and T. Bulik. Double compact objects as low-frequency gravitational wave sources (2008). arXiv:0811.1602.

[34] K. Belczynski, R. E. Taam, V. Kalogera, F. A. Rasio, and T. Bulik. On the rarity of double black hole binaries: consequences for gravitational-wave detection. *ApJ*, 662:504 (2007). astro-ph/0612032.

[35] P. Berczik, D. Merritt, and R. Spurzem. Long-term evolution of massive black hole binaries. ii. binary evolution in low-density galaxies. *ApJ*, 633:680 (2005). astro-ph/0507260.

[36] E. Berti, V. Cardoso, and M. Casals. Eigenvalues and eigenfunctions of spin-weighted spheroidal harmonics in four and higher dimensions. *Phys. Rev. D*, 73:024013 (2006). Erratum-ibid.D73(2006)109902, gr-qc/0511111.

[37] E. Berti, V. Cardoso, and C. M. Will. On gravitational-wave spectroscopy of massive black holes with the space interferometer lisa. *Phys. Rev. D*, 73:064030 (2006). gr-qc/0512160.

[38] H. Beyer and O. Sarbach. On the well posedness of the baumgarte-shapiro-shibata- nakamura formulation of einstein's field equations. *Phys. Rev. D*, 70:104004 (2004). gr-qc/0406003.

[39] T. Bogdanović, C. S. Reynolds, and M. C. Miller. Alignment of the spins of supermassive black holes prior to coalescence. *ApJ*, 661:L147 (2007). astro-ph/0703054.

[40] C. Bona, J. Massó, E. Seidel, and J. Stela. New formalism for numerical relativity. *Phys. Rev. Lett.*, 75(4):600 (1995).

[41] J. M. Bowen. General solution for flat-space longitudinal momentum. *Gen. Rel. Grav.*, 14:1183 (1982).

[42] J. M. Bowen and J. W. York. Time asymmetric initial data for black holes and black hole collisions. *Phys. Rev. D*, 21:2047 (1980).

[43] S. Brandt and B. Brügmann. Black hole punctures as initial data for general relativity. *Phys. Rev. Lett.*, 78:3606 (1997). gr-qc/9703066.

[44] S. Brandt and B. Brügmann. A simple construction of initial data for multiple black holes. *Phys. Rev. Lett.*, 78(19):3606 (1997). gr-qc/9703066.

[45] S. Brandt, R. Correll, R. Gómez, M. F. Huq, P. Laguna, L. Lehner, P. Marronetti, R. A. Matzner, D. Neilsen, J. Pullin, E. Schnetter, D. Shoemaker, and J. Winicour. Grazing collisions of black holes via the excision of singularities. *Phys. Rev. Lett.*, 85:5496 (2000).

[46] D. Brill and R. Lindquist. Interaction energy in geometrostatics. *Phys. Rev.*, 131:471 (1963).

[47] D. R. Brill. On the positive definite mass of the bondi-weber-wheeler time-symmetric gravitational waves. *Annals Phys.*, 7:466 (1959).

[48] D. Brown, P. Diener, O. Sarbach, E. Schnetter, and M. Tiglio. Turduckening black holes: An analytical and computational study. *Phys. Rev. D*, 79(4):044023 (2009). arXiv:0809.3533.

[49] L. e. a. Burderi, (Ed.). *Compact Binaries as Sources of Gravitational Radiation*, Proceedings of the Multicoloured Landscape of Compact Objects and their Explosive Origins. AIP, Cefalu, Italy (2006). astro-ph/0612055.

[50] M. Campanelli, B. Kelly, and C. O. Lousto. The lazarus project. ii. spacelike extraction with the quasi-kinnersley tetrad. *Phys. Rev. D*, 73(6):064005 (pages 17) (2006). gr-qc/0510122, URL http://link.aps.org/abstract/PRD/v73/e064005.

[51] M. Campanelli, W. Krivan, and C. O. Lousto. The imposition of cauchy data to the teukolsky equation ii: Numerical comparison with the zerilli-moncrief approach to black hole perturbations. *Phys. Rev. D*, 58:024016 (1998). gr-qc/9801067.

[52] M. Campanelli and C. O. Lousto. The imposition of cauchy data to the teukolsky equation i: The nonrotating case. *Phys. Rev. D*, 58:024015 (1998). gr-qc/9711008.

[53] M. Campanelli and C. O. Lousto. Second order gauge invariant gravitational perturbations of a kerr black hole. *Phys. Rev. D*, 59:124022 (1999). gr-qc/9811019.

[54] M. Campanelli, C. O. Lousto, J. Baker, G. Khanna, and J. Pullin. The imposition of cauchy data to the teukolsky equation iii: The rotating case. *Phys. Rev. D*, 58:084019 (1998). Erratum-ibid.D62(2000)069901, gr-qc/9803058.

[55] M. Campanelli, C. O. Lousto, P. Marronetti, and Y. Zlochower. Accurate evolutions of orbiting black-hole binaries without excision. *Phys. Rev. Lett.*, 96:111101 (2006). gr-qc/0511048.

[56] M. Campanelli, C. O. Lousto, and Y. Zlochower. The last orbit of binary black holes. *Phys. Rev. D*, 73:061501 (2006). gr-qc/0601091.

[57] M. Campanelli, C. O. Lousto, and Y. Zlochower. Close encounters of three black holes. *Phys. Rev. D*, 77:101501 (2008). arXiv:0710.0879.

[58] M. Campanelli, C. O. Lousto, Y. Zlochower, B. Krishnan, and D. Merritt. Spin flips and precession in black-hole-binary mergers. *Phys. Rev. D*, 75:064030 (2007). gr-qc/0612076.

[59] S. Chandrasekhar. *The Mathematical Theory of Black Holes*. Oxford University Press (1983).

[60] D.-I. Choi, B. J. Kelly, W. D. Boggs, J. G. Baker, J. Centrella, and J. van Meter. Recoiling from a kick in the head-on collision of spinning black holes. *Phys. Rev. D*, 76:104026 (2007). gr-qc/0702016.

[61] Y. Choquet-Bruhat, J. Isenberg, and J. W. York. Einstein constraints on asymptotically euclidean manifolds. *Phys. Rev. D*, 61(8):084034 (2000).

[62] P. Colella and P. Woodward. The piecewise parabolic method (ppm) for gas-dynamical simulations. *J. Comput. Phys.*, 54:174 (1984).

[63] G. B. Cook. Initial data for numerical relativity. *Living Rev. Rel.*, 3:5 (2000). gr-qc/0007085, URL http://www.livingreviews.org/lrr-2000-5.

[64] J. Cuadra, P. J. Armitage, R. D. Alexander, and M. C. Begelman. Massive black hole binary mergers within sub-pc scale gas discs. *Mon. Not. Roy. Astron. Soc.*, 393:1423 (2009). arXiv:0809.0311.

[65] S. Dain, C. O. Lousto, and Y. Zlochower. Extra-large remnant recoil velocities and spins from near-extremal-bowen-york-spin black-hole binaries. *Phys. Rev. D*, 78:024039 (2008). arXiv:0803.0351, URL doi:10.1103/PhysRevD.78.024039.

[66] T. Damour, B. R. Iyer, and B. S. Sathyaprakash. Improved filters for gravitational waves from inspiralling compact binaries. *Phys. Rev. D*, 57:885 (1998).

[67] K. A. Dennison, T. W. Baumgarte, and H. P. Pfeiffer. Approximate initial data for binary black holes. *Phys. Rev. D*, 74:064016 (2006). gr-qc/0606037.

[68] P. Diener. A new general purpose event horizon finder for 3d numerical spacetimes. *Class. Quant. Grav.*, 20:4901 (2003). gr-qc/0305039.

[69] H. Dimmelmeier, J. Novak, J. A. Font, J. M. Ibanez, and E. Mueller. "mariage des maillages": A new numerical approach for 3d relativistic core collapse simulations. *Phys.Rev. D*, 71:064023 (2005). astro-ph/0407174.

[70] R. Donat and A. Marquina. Capturing shock reflections: An improved flux formula. *J. Comput. Phys.*, 125(1):42 (1996).

[71] O. Dreyer, B. Krishnan, D. Shoemaker, and E. Schnetter. Introduction to isolated horizons in numerical relativity. *Phys. Rev. D*, 67:024018 (2003). gr-qc/0206008.

[72] M. D. Duez, P. Marronetti, S. L. Shapiro, and T. W. Baumgarte. Hydrodynamic simulations in 3+1 general relativity. *Phys. Rev. D*, 67:024004 (2003). gr-qc/0209102.

[73] K. Eppley. Ph.D. thesis, Princeton University (1977).

[74] K. Eppley. Pure gravitational waves. In *Sources of Gravitational Radiation*, edited by L. L. Smarr, pp. 275–291. Cambridge University Press, Cambridge, Cambridge, UK (1979).

[75] A. Escala, R. B. Larson, P. S. Coppi, , and D. Mardones. The role of gas in the merging of massive black holes in galactic nuclei. i. black hole merging in a spherical gas cloud. *ApJ*, 607(2):765 (2004). URL http://stacks.iop.org/0004-637X/607/765.

[76] A. Escala, R. B. Larson, P. S. Coppi, , and D. Mardones. The role of gas in the merging of massive black holes in galactic nuclei. ii. black hole merging in a nuclear gas disk. *ApJ*, 630(1):152 (2005). URL http://stacks.iop.org/0004-637X/630/152.

[77] J. A. Faber, T. W. Baumgarte, Z. B. Etienne, S. L. Shapiro, and K. Taniguchi. Relativistic hydrodynamics in the presence of puncture black holes. *Phys. Rev. D*, 76:104021 (2007). arXiv:0708.2436.

[78] G. Faye, P. Jaranowski, and G. Schafer. A skeleton approximate solution of the einstein field equations for multiple black-hole systems. *Phys. Rev. D*, 69:124029 (2004). gr-qc/0311018.

[79] L. S. Finn. Detection, measurement and gravitationfinal radiation. *Phys. Rev. D*, 46:5236 (1992).

[80] D. R. Fiske, J. G. Baker, J. R. van Meter, D.-I. Choi, and J. M. Centrella. Wave zone extraction of gravitational radiation in three-dimensional numerical relativity. *Phys. Rev. D*, 71:104036 (2005). gr-qc/0503100.

[81] J. Font, J. Ibáñez, A. Marquina, and J. Martí. Multidimensional relativistic hydrodynamics: Characteristic fields and modern high-resolution shock-capturing schemes. *Astron. Astrophys.*, 282:304 (1994).

[82] J. A. Font. Numerical hydrodynamics and magnetohydrodynamics in general relativity. *Living Rev. Rel.*, 3:2 (2000). Cited on December 2008, gr-qc/0003101.

[83] R. Foster and D. Backer. Constructing a pulsar timing array. *ApJ*, 361:300 (1990).

[84] J. Frauendiener. On discretizations of axisymmetric systems. *Phys. Rev. D*, 66:104027 (2002). gr-qc/0207092.

[85] H. Friedrich. Conformal einstein evolution. *Lect. Notes Phys.*, 604:1 (2002). gr-qc/0209018.

[86] A. Garat and R. H. Price. Nonexistence of conformally flat slices of the kerr spacetime. *Phys. Rev. D*, 61:124011 (2000). gr-qc/0002013.

[87] A. P. Gentle. The bssn formulation is a partially constrained evolution system (2007). arXiv:0707.0339.

[88] A. Ghez, M. Morris, E. E. Becklin, T. Kremenek, and A. Tanner. The accelerations of stars orbiting the milky way's central black hole. *Nature*, 407:349 (2000). astro-ph/0009339.

[89] B. Giacomazzo and L. Rezzolla. Whiskymhd: a new numerical code for general relativistic magnetohydrodynamics. *Class. Quant. Grav.*, 24(12):S235 (2007). URL http://stacks.iop.org/0264-9381/24/S235.

[90] S. Gillessen, F. Eisenhauer, S. Trippe, T. Alexander, R. Genzel, F. Martins, and T. Ott. Monitoring stellar orbits around the massive black hole in the galactic center. *ApJ*, 692:902 (2009). arXiv:0810.4674.

[91] J. Goldberg, A. Macfarlane, E. Newman, F. Rohrlich, and E. Sudarshan. Spin-s spherical harmonics and ð. *J. Math. Phys.*, 8:2155 (1967).

[92] J. A. Gonzalez, U. Sperhake, B. Brügmann, M. Hannam, and S. Husa. Total recoil: the maximum kick from nonspinning black-hole binary inspiral. *Phys. Rev. Lett.*, 98:091101 (2007). gr-qc/0610154.

[93] A. Gould and H.-W. Rix. Binary black hole mergers from planet-like migrations. *ApJ*, 532(1):L29 (2000). astro-ph/9912111, URL http://stacks.iop.org/1538-4357/532/L29.

[94] E. Gourgoulhon. Construction of initial data for 3+1 numerical relativity. *J. Phys. Conf. Ser.*, 91:012001 (2007). arXiv:0704.0149.

[95] C. Gundlach (2009). Email conversation.

[96] C. Gundlach and J. M. Martin-Garcia. Hyperbolicity of second-order in space systems of evolution equations. *Class. Quant. Grav.*, 23:S387 (2006). gr-qc/0506037.

[97] C. Gundlach and J. M. Martin-Garcia. Well-posedness of formulations of the einstein equations with dynamical lapse and shift conditions. *Phys. Rev. D*, 74:024016 (2006). gr-qc/0604035.

[98] S. G. Hahn and R. W. Lindquist. The two-body problem in geometrodynamics. *Annals Phys.*, 29:304 (1964).

[99] M. Hannam, S. Husa, B. Brügmann, J. A. Gonzalez, and U. Sperhake. Beyond the bowen-york extrinsic curvature for spinning black holes. *Class. Quant. Grav.*, 24:S15 (2007). gr-qc/0612001.

[100] M. Hannam, S. Husa, U. Sperhake, B. Brügmann, and J. A. Gonzalez. Where post-newtonian and numerical-relativity waveforms meet. *Phys. Rev. D*, 77:044020 (2008). arXiv:0706.1305.

[101] M. Hannam et al. The samurai project: verifying the consistency of black- hole-binary waveforms for gravitational-wave detection. *Phys. Rev. D*, 79:084025 (2009). arXiv:0901.2437.

[102] S. Hayward. General laws of black hole dynamics. *Phys. Rev. D*, 49:6467 (1994). gr-qc/9306006.

[103] F. Herrmann, I. Hinder, D. Shoemaker, and P. Laguna. Unequal mass binary black hole plunges and gravitational recoil. *Class. Quant. Grav.*, 24:S33 (2007).

[104] F. Herrmann, I. Hinder, D. Shoemaker, P. Laguna, and R. A. Matzner. Gravitational recoil from spinning binary black hole mergers. *ApJ*, 661(1):430 (2007). gr-qc/0701143, URL http://www.journals.uchicago.edu/doi/abs/10.1086/513603.

[105] F. Herrmann, I. Hinder, D. M. Shoemaker, P. Laguna, and R. A. Matzner. Binary black holes: Spin dynamics and gravitational recoil. *Phys. Rev. D*, 76:084032 (2007). arXiv:0706.2541.

[106] I. Hinder, B. Vaishnav, F. Herrmann, D. M. Shoemaker, and P. Laguna. Circularization and final spin in eccentric binary-black-hole inspirals. *Phys. Rev. D*, 77(8):081502 (pages 5) (2008). URL http://link.aps.org/abstract/PRD/v77/e081502.

[107] R. A. Hulse and J. Taylor. Discovery of a pulsar in a binary system. *ApJ*, 195:L51 (1975).

[108] S. Husa, I. Hinder, and C. Lechner. Kranc: a mathematica application to generate numerical codes for tensorial evolution equations. *Computer Physics Communications*, 174:983 (2006).

[109] J. M. Ibáñez, M. A. Aloy, J. A. Font, J. M. Martí, J. A. Miralles, and J. A. Pons. Riemann solvers in general relativistic hydrodynamics. In *Godunov Methods: Theory and Applications*, edited by E. F. Toro, p. 485. Kluwer Academic (2001). astro-ph/9911034.

[110] J. Ibáñez. Numerical relativistic hydrodynamics. In *Rotating Objects and Relativistic Physics*, edited by F. Chinea and L. González-Romero, vol. 423 of *Lecture Notes in Physics, Berlin Springer Verlag*, pp. 147–183 (1993).

[111] J. Ibáñez. Numerical general-relativistic hydrodynamics: Riemann solvers. In *Eighteenth Texas Symposium on Relativistic Astrophysics*, edited by A. Olinto, J. Frieman, and D. Schramm, p. 598 (1998).

[112] R. Isaacson. Gravitational radiation in the limit of high frequency. ii. nonlinear terms and the effective stress tensor. *Phys. Rev.*, 166:1272 (1968).

[113] P. Jaranowski and G. Schafer. On bare masses in time-symmetric initial-value solutions for two black holes. *Phys. Rev. D*, 61:064008 (2000). gr-qc/9907025.

[114] E. M. Jos Maria Mart. Numerical hydrodynamics in special relativity. *Living Rev. Rel.*, 6(7) (2003). URL http://www.livingreviews.org/lrr-2003-7.

[115] B. J. Kelly, W. Tichy, M. Campanelli, and B. F. Whiting. Black hole puncture initial data with realistic gravitational wave content. *Phys. Rev. D*, 76:024008 (2007). arXiv:0704.0628.

[116] W. Kinnersley. Type d vacuum metrics. *J. Math. Phys.*, 10:1195 (1969).

[117] B. Kocsis, M. Gáspár, and S. Márka. Detection Rate Estimates of Gravity Waves Emitted during Parabolic Encounters of Stellar Black Holes in Globular Clusters. *ApJ*, 648:411 (2006). astro-ph/0603441.

[118] K. D. Kokkotas and B. G. Schmidt. Quasi-normal modes of stars and black holes. *Living Rev. Rel.*, 2(2) (1999). gr-qc/9909058.

[119] M. Koppitz, D. Pollney, C. Reisswig, L. Rezzolla, J. Thornburg, P. Diener, and E. Schnetter. Getting a kick from equal-mass binary black hole mergers. *Phys. Rev. Lett.*, 99:041102 (2007). gr-qc/0701163.

[120] A. Lazzarini and R. Weiss. Ligo science requirements document. Tech. Rep. E950018-02-E (1996).

[121] L. Lehner and O. M. Moreschi. Dealing with delicate issues in waveforms calculations. *Phys. Rev. D*, 76:124040 (2007). arXiv:0706.1319.

[122] J. Levine and R. Stebbins. Upper limit on the gravitational flux reaching the earth from the crab pulsar. *Phys. Rev. D*, 6:1465 (1972).

[123] A. Lichnerowicz. L'intégration des équations de la gravitation relativiste et la problème des n corps. *J. Math Pures et Appl.*, 23:37 (1944).

[124] L. Lindblom, B. J. Owen, and D. A. Brown. Model waveform accuracy standards for gravitational wave data analysis. *Phys. Rev. D*, 78:124020 (2008). arXiv:0809.3844.

[125] R. Lindquist. Initial-value problem on einstein-rosen manifolds. *J. Math. Phys.*, 4:938 (1963).

[126] F. Löffler, L. Rezzolla, and M. Ansorg. Numerical evolutions of a black hole-neutron star system in full general relativity: I. head-on collision. *Phys. Rev. D*, 74:104018 (2006). gr-qc/0606104.

[127] C. O. Lousto and Y. Zlochower. Foundations of multiple black hole evolutions. *Phys. Rev. D*, 77:024034 (2008). arXiv:0711.1165.

[128] G. Lovelace. Reducing spurious gravitational radiation in binary-black- hole simulations by using conformally curved initial data. *Class. Quant. Grav.*, 26:114002 (2009). arXiv:0812.3132.

[129] R. N. Manchester. The parkes pulsar timing array. In *40 Years of Pulsars: Millisecond Pulsars, Magnetars and More*, vol. 983, pp. 584–592. AIP Conf. Proc., Montreal (2008). arXiv:0710.5026.

[130] P. Marronetti, M. F. Huq, P. Laguna, L. Lehner, R. A. Matzner, and D. Shoemaker. Approximate analytical solutions to the initial data problem of black hole binary systems. *Phys. Rev. D*, 62:024017 (2000). Gr-qc/0001077.

[131] P. Marronetti, W. Tichy, B. Brügmann, J. Gonzalez, and U. Sperhake. High-spin binary black hole mergers. *Phys. Rev. D*, 77:064010 (2008). arXiv:0709.2160.

[132] J. M. Martí, J. M. Ibáñez, and J. A. Miralles. Numerical relativistic hydrodynamics: Local characteristic approach. *Phys. Rev. D*, 43(12):3794 (1991).

[133] J. M. Martí and E. Müeller. The analytical solution of the riemann problem in relativistic hydrodynamics. *J. Fluid. Mech.*, 258:317 (1994).

[134] J. Mathews. Gravitational multipole radiation. *J. Soc. Indust. Appl. Math.*, 10:768 (1962).

[135] R. A. Matzner, M. F. Huq, and D. Shoemaker. Initial data and coordinates for multiple black hole systems. *Phys. Rev. D*, 59:024015 (1999).

[136] M. Milosavljevic and D. Merritt. Formation of galactic nuclei. *ApJ*, 563:34 (2001). astro-ph/0103350.

[137] C. W. Misner, K. Thorne, and J. Wheeler. *Gravitation*. W. H. Freeman and Co., New York, NY (1973).

[138] M. Morris and E. Serabyn. The galactic center environment. *Ann. Rev. Astron. Astrophys.*, 34:645 (1996).

[139] N. Murchadha and J. York. Gravitational potentials: A constructive approach to general relativity. *Gen. Rel. Grav.*, 7:257 (1976).

[140] T. Nakamura, K. Oohara, and Y. Kojima. General relativistic collapse to black holes and gravitational waves from black holes. *Prog. Theor. Phys. Suppl.*, 90:1 (1987).

[141] E. Newman and R. Penrose. An approach to gravitational radiation by a method of spin coefficients. *J. Math. Phys.*, 3:566 (1962).

[142] E. Newman and R. Penrose. Note on the bondi-metzner-sachs group. *J. Math. Phys.*, 7:863 (1966).

[143] S. Nissanke. Post-newtonian freely specifiable initial data for binary black holes in numerical relativity. *Phys. Rev. D*, 73:124002 (2006). gr-qc/0509128.

[144] E. Noyola, K. Gebhardt, and M. Bergmann. Gemini and hubble space telescope evidence for an intermediate mass black hole in omega centauri. *ApJ*, 676:1008 (2008). arXiv:0801.2782.

[145] R. Oechslin, H. T. Janka, and A. Marek. Relativistic neutron star merger simulations with non-zero temperature equations of state i. variation of binary parameters and equation of state. *Astron. Astrophys.*, 467:395 (2007). astro-ph/0611047.

[146] B. Owen. Search templates for gravitational waves from inspiraling binaries: Choice of template spacing. *Phys. Rev. D*, 53:6749 (1996).

[147] E. Pazos, E. N. Dorband, A. Nagar, C. Palenzuela, E. Schnetter, and M. Tiglio. How far away is far enough for extracting numerical waveforms, and how much do they depend on the extraction method? *Class. Quant. Grav.*, 24:S341 (2007). gr-qc/0612149.

[148] P. Peters. Gravitational radiation and the motion of two point masses. *Phys. Rev.*, 136:1224 (1964).

[149] H. P. Pfeiffer. The initial value problem in numerical relativity (2004). gr-qc/0412002.

[150] H. P. Pfeiffer, D. A. Brown, L. E. Kidder, L. Lindblom, G. Lovelace, and M. A. Scheel. Reducing orbital eccentricity in binary black hole simulations. *Class. Quant. Grav.*, 24:S59 (2007). gr-qc/0702106.

[151] H. P. Pfeiffer, G. B. Cook, and S. A. Teukolsky. Comparing initial-data sets for binary black holes. *Phys. Rev. D*, 66:024047 (2002). gr-qc/0203085.

[152] H. P. Pfeiffer, L. E. Kidder, M. A. Scheel, and S. A. Teukolsky. A multidomain spectral method for solving elliptic equations. *Comput. Phys. Commun.*, 152:253 (2003). gr-qc/0202096.

[153] J. N. Philippe Grandclment. Spectral methods for numerical relativity. *Living Rev. Rel.*, 12(1) (2009). Cited in February 2009, URL http://www.livingreviews.org/lrr-2009-1.

[154] M. Preto, I. Berentzen, P. Berczik, D. Merritt, and R. Spurzem. Merger of massive black holes using n-body simulations with post-newtonian corrections (2008). arXiv:0811.3501.

[155] F. Pretorius. Evolution of binary black hole spacetimes. *Phys. Rev. Lett.*, 95:121101 (2005). gr-qc/0507014.

[156] F. Pretorius. *Binary Black Hole Coalescence*, vol. 359 of *Astrophysics and Space Sciences Library*. Springer Verlag, Canpus Publishing Ltd (2009). arXiv:0710.1338.

[157] J. Quirk. A contribution to the great riemann solver debate. *Int. J. Num. Methods Fluids*, 18:555 (1994).

[158] T. Regge and J. Wheeler. Stability of a schwarzschild singularity. *Phys. Rev.*, 108:1063 (1957).

[159] O. Reula. Strongly hyperbolic systems in general relativity (2004). gr-qc/0403007.

[160] M. Ruiz, M. Alcubierre, D. Nunez, and R. Takahashi. Multipole expansions for energy and momenta carried by gravitational waves. *Gen. Rel. Grav.*, 40:2467 (2008). arXiv:0707.4654.

[161] O. Sarbach, G. Calabrese, J. Pullin, and M. Tiglio. Hyperbolicity of the bssn system of einstein evolution equations. *Phys. Rev. D*, 66:064002 (2002). gr-qc/0205064.

[162] B. S. Sathyaprakash and B. F. Schutz. Physics, astrophysics and cosmology with gravitational waves. *Living Rev. Rel.*, 12:2 (2009). arXiv:0903.0338.

[163] E. Schnetter, S. H. Hawley, and I. Hawke. Evolutions in 3d numerical relativity using fixed mesh refinement. *Class. Quant. Grav.*, 21:1465 (2004). gr-qc/0310042.

[164] E. Schnetter, B. Krishnan, and F. Beyer. Introduction to dynamical horizons in numerical relativity. *Phys. Rev. D*, 74(2):024028 (pages 20) (2006). URL http://link.aps.org/abstract/PRD/v74/e024028.

[165] A. Sesana, A. Vecchio, and M. Volonteri. Gravitational waves from resolvable massive black hole binary systems and observations with pulsar timing arrays. *Mon. Not. Roy. Astron. Soc.*, 394:2255 (2009). arXiv:0809.3412.

[166] M. Shibata and T. Nakamura. Evolution of three-dimensional gravitational waves: Harmonic slicing case. *Phys. Rev. D*, 52:5428 (1995).

[167] H.-a. Shinkai and G. Yoneda. Constraint propagation in (n+1)-dimensional space-time. *Gen. Rel. Grav.*, 36:1931 (2004). gr-qc/0402101.

[168] L. L. Smarr. *The Structure of General Relativity with a Numerical Illustration: The Collision of Two Black Holes*. Ph.D. thesis, University of Texas at Austin (1975).

[169] U. Sperhake. Binary black-hole evolutions of excision and puncture data. *Phys. Rev. D*, 76:104015 (2007). gr-qc/0606079.

[170] U. Sperhake, E. Berti, V. Cardoso, J. A. Gonzalez, B. Brügmann, and M. Ansorg. Eccentric binary black-hole mergers: The transition from inspiral to plunge in general relativity. *Phys. Rev. D*, 78:064069 (2008). arXiv:0710.3823.

[171] U. Sperhake, B. Kelly, P. Laguna, K. Smith, and E. Schnetter. Black hole head-on collisions and gravitational waves with fixed mesh-refinement and dynamic singularity excision. *Phys. Rev. D*, 71(12):124042 (2005).

[172] J. Taylor and J. Weisberg. A new test of general relativity - Gravitational radiation and the binary pulsar PSR 1913+16. *ApJ*, 253:908 (1982).

[173] S. Teukolsky. Perturbations of a rotating black hole. i. fundamental equations for gravitational, electromagnetic, and neutrino-field perturbations. *ApJ*, 185:635 (1973).

[174] S. A. Teukolsky. Linearized quadrupole waves in general relativity and the motion of test particles. *Phys. Rev. D*, 26:745 (1982).

[175] J. Thornburg. A multiple-grid-patch evolution scheme for 3-D black hole excision. In *The Ninth Marcel Grossman Meeting: On Recent Developments in Theoretical and Experimental General Relavtivity, Gravitation, and Relativistic Field Theories*, edited by V. G. Gurzadyan, R. T. Jantzen, and R. Ruffini, pp. 1743–1744. World Scientific, Singapore (2003). gr-qc/0012012.

[176] J. Thornburg. A fast apparent-horizon finder for 3-dimensional cartesian grids in numerical relativity. *Class. Quant. Grav.*, 21:743 (2004). gr-qc/0306056.

[177] J. Thornburg. Event and apparent horizon finders for 3+1 numerical relativity. *Living Rev. Rel.*, 10(3) (2007). gr-qc/0512169.

[178] K. S. Thorne. Multipole expansions of gravitational radiation. *Rev. Mod. Phys.*, 52:299 (1980).

[179] W. Tichy and B. Brügmann. Quasi-equilibrium binary black hole sequences for puncture data derived from helical killing vector conditions. *Phys. Rev. D*, 69:024006 (2004). gr-qc/0307027.

[180] W. Tichy, B. Brügmann, M. Campanelli, and P. Diener. Binary black hole initial data for numerical general relativity based on post-newtonian data. *Phys. Rev. D*, 67:064008 (2003). gr-qc/0207011.

[181] W. Tichy and P. Marronetti. Binary black hole mergers: Large kicks for generic spin orientations. *Phys. Rev. D*, 76:061502 (2007). gr-qc/0703075.

[182] E. F. Toro, (Ed.). *Godunov Methods: Theory and Applications*, Proceedings of an International Conference on Godunov Methods: Theory and Applications. Kluwer Academic, New York (2001).

[183] B. Vaishnav, I. Hinder, F. Herrmann, and D. Shoemaker. Matched filtering of numerical relativity templates of spinning binary black holes. *Phys. Rev. D*, 76:084020 (2007). arXiv:0705.3829.

[184] R. Wald. *General Relativity*. University of Chicago Press, Chicago, U.S.A. (1984).

[185] J. Weber. Detection and generation of gravitational waves. *Phys. Rev.*, 117(1):306 (1960).

[186] J. Wilson. Numerical study of fluid flow in a kerr space. *ApJ*, 173:431 (1972).

[187] J. Winicour. Characteristic evolution and matching. *Living Rev. Rel.*, 8(10) (2005). gr-qc/0508097.

[188] T. Yamamoto, M. Shibata, and K. Taniguchi. Simulating coalescing compact binaries by a new code sacra. *Phys. Rev. D*, 78:064054 (2008). arXiv:0806.4007.

[189] G. Yoneda and H.-a. Shinkai. Advantages of modified adm formulation: constraint propagation analysis of baumgarte-shapiro-shibata-nakamura system. *Phys. Rev. D*, 66:124003 (2002). gr-qc/0204002.

[190] J. York, James W. Gravitational degrees of freedom and the initial-value problem. *Phys. Rev. Lett.*, 26:1656 (1971).

[191] J. York, Jr. Initial data for collisions of black holes and other gravitational miscellany. pp. 89–109 (1989).

[192] J. W. York. Kinematics and dynamics of general relativity. In *Sources of Gravitational Radiation*, edited by L. L. Smarr, pp. 83–126. Cambridge University Press, Cambridge, UK (1979).

[193] J. W. York. In *Essays in General Relativity*, edited by F. J. Tipler, chap. 4, pp. 39–57. Academic (1980).

[194] Q. Yu. Evolution of massive binary black holes. *Mon. Not. Roy. Astron. Soc.*, 331:935 (2002). astro-ph/0109530.

[195] N. Yunes and W. Tichy. Improved initial data for black hole binaries by asymptotic matching of post-newtonian and perturbed black hole solutions. *Phys. Rev. D*, 74:064013 (2006). gr-qc/0601046.

[196] N. Yunes, W. Tichy, B. J. Owen, and B. Brügmann. Binary black hole initial data from matched asymptotic expansions. *Phys. Rev. D*, 74:104011 (2006). gr-qc/0503011.

[197] F. J. Zerilli. Tensor harmonics in canonical form for gravitational radiation and other applications. *J. Math. Phys.*, 11:2203 (1970).

Vita

Tanja Bode

Tanja Bode was born in New Haven, CT on February 25, 1982. She is the youngest of the two daughters of Ute and Udo Bode. She attended Cornell University, doing research in the area of observational submillimeter astronomy with a summer internship in radio astronomy at the MIT Haystack Observatory. In May 2004 she received her B.A. in Physics with a concentration in Astronomy. From there she moved directly to State College, PA to begin her graduate studies in the physics department of the Pennsylvania State University. She was a Teaching Assistant for her first two years, but already began work with the Numerical Relativity group under Deirdre Shoemaker in the summer of 2005. Tanja Bode has been a student member of the American Physical Society since 2007.

1. T. Bode, D. Shoemaker, F. Herrmann, and I. Hinder, "Robustness of binary black hole mergers in the presence of spurious radiation," *Phys. Rev. D* 77, 044027 (2008).

2. T. Bode, P. Laguna, D. Shoemaker, I. Hinder, F. Herrmann, and B. Vaishnav, "Binary black hole evolutions of approximate puncture initial data," arXiv:0902.1127 (2009).